PRESSURE DEPENDENCE OF THE LUMINESCENCE AND RAMAN MODES IN POLYFLUORENE

A Dissertation presented to
the Faculty of the Graduate School
University of Missouri-Columbia

In Partial Fulfillment
Of the Requirements for the Degree
Doctor of Philosophy

by

CHRISTOPHER M. MARTIN

Dr. H. R. Chandrasekhar, Dissertation Supervisor
MAY 2005

Department of Physics and Astronomy

University of Missouri-Columbia

The undersigned, appointed by the Dean of the Graduate School, have examined the dissertation entitled

Pressure Dependence of the Luminescence and Raman Modes in Polyfluorene

Presented by Christopher M. Martin,
a candidate for the degree DOCTOR OF PHILOSOPHY,
and hereby certify that in their opinion it is worthy of acceptance

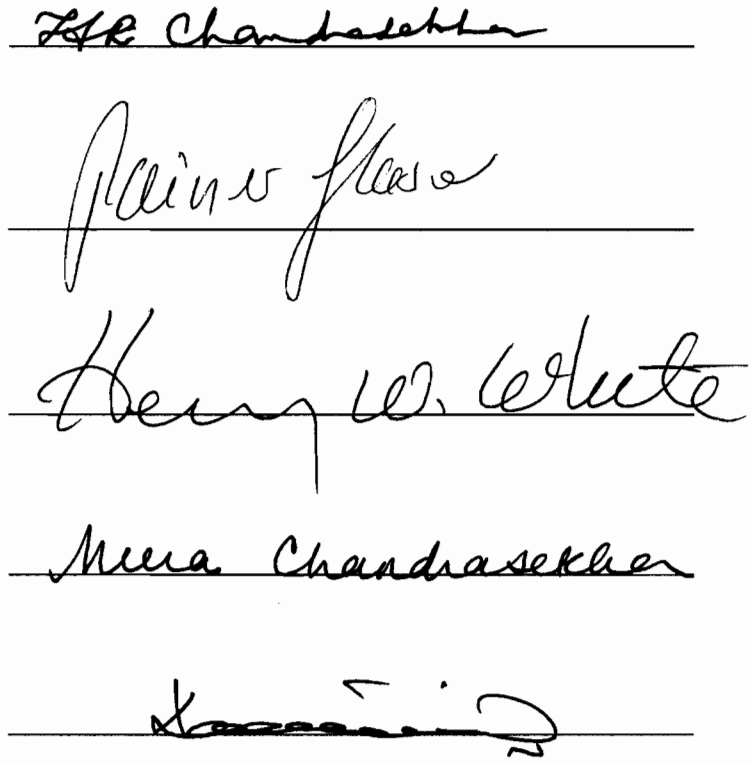

ACKNOWLEDGMENTS

I would like to thank Dr. Meera Chandrasekhar and Dr. H.R. (Chandra) Chandrasekhar for their continued guidance and support through the years. Their enduring patience and scientific insight helped to create a large number of publications and opportunities for collaborations within the scientific community. I would like to thank explicitly some of the very long list of collaborators that have helped me in the process of completing my research; S. Guha, G. Heimel, W. Graupner, U. Scherf, M.J. Winokur, and Q. Cai. I would like to thank Dr. Peter Pfeifer and Dr. Brian DeFacio for providing outstanding courses that challenged and rewarded the students.

I would like to thank my family and friends especially those who were there to help offer support in my times of madness. I can not say enough to thank Rainee Kaczorowski for making each day the best that it could be.

I have enjoyed my time working and studying in the MU Physics department and the opportunities afforded to me.

Thank You

Christopher Martin

PUBLICATION LISTING FOR C.M. MARTIN

1. Influence of the Molecular Geometry on the Photoexcitations of Highly Emissive Organic Semiconductors
   S. Yang, W. Graupner, S. Guha, P. Puschnig, C. Martin, H. R. Chandrasekhar, M. Chandrasekhar, G. Leising, C. Ambrosch-Draxl, SPIE Proceedings 3797, 26-37 (1999)

2. Geometry Dependent Electronic Properties of Highly Fluorescent Conjugated Molecules
   S. Yang, W. Graupner, S. Guha, P. Puschnig, C. Martin, H. R. Chandrasekhar, M. Chandrasekhar, G. Leising, C. Ambrosch-Draxl, Phys. Rev. Lett., 85, 2388 (2000).

3. High Pressure Raman Studies on the Structural Conformation of Oligophenyls
   G. Heimel, P. Puschnig, Q. Cai, C. Martin, E. Zojer, W. Graupner, M. Chandrasekhar, H. R. Chandrasekhar, C. Ambrosch-Draxl, G. Leising, Synthetic Metals, 116, 163-166 (2001)

4. High-Pressure Effect on the Photoluminescence Intensity of Sexithiophene Single Crystals
   M. A. Loi, G. Bongiovanni, A. Mura, Q. Cai, C. Martin, H. R. Chandrasekhar, M. Chandrasekhar, W. Graupner, F. Garnier, Synthetic Metals, 116, 311-315 (2001)

5. Pressure-Induced Quenching of the Photoluminescence in Sexithiophene Single Crystals Observed by Femtosecond Spectroscopy
   M. A. Loi, A. Mura, G. Bongiovanni , Q. Cai, C. Martin, H. R. Chandrasekhar, M. Chandrasekhar, W. Graupner, F. Garnier, Synthetic Metals, 119, 645-646 (2001)

6. Optical Transitions in *para*-phenylenes under Hydrostatic Pressure
   M. Chandrasekhar, S.C. Yang, S. Guha, Q. Cai, C.M. Martin, H.R. Chandrasekhar, W. Graupner and G. Leising, Synthetic Metals, 119, 657-658 (2001)

7. On the Structure of Oligophenyls
   G. Heimel, Q. Cai, C. Martin, P. Puschnig, S. Guha,. W. Graupner, C. Ambrosch-Draxl, M. Chandrasekhar and G. Leising, Synthetic Metals, 119, 371-372 (2001)

8. Ultrafast Formation of Nonemissive Species versus Intermolecular Interaction in Single Crystals of Conjugated Molecules

M. A. Loi, A. Mura, G. Bongiovanni, Q. Cai, C. Martin, H. R. Chandrasekhar, M. Chandrasekhar W. Graupner, and F. Garnier, Phys. Rev. Lett., 86, 732 (2001)

9. Ultrafast Formation of Nonemissive States in Organic Semiconductors
   M. A. Loi, A. Mura, G. Bongiovanni, Q. Cai, C. Martin, H. R. Chandrasekhar, M. Chandrasekhar W. Graupner, and F. Garnier, Istito Nazionale per la Fisica della Materia (INFM), Highlights 2000/2001, 81-83

10. Incorporation of AsSe Centers in ZnSe Far-From-Equilibrium
    J.W. Farmer, Jack L. Boone, Nickolas L. Brakensiek, E.D. Wheeler, H.R. Chandrasekhar, and C.M. Martin, J. Phys Chem. Solids 63, 1921 (2002)

11. A study of Far-From-Equilibrium Doping in ZnSe
    E.D. Wheeler, Jack L. Boone, Nickolas L. Brakensiek, J.W. Farmer, H.R. Chandrasekhar, and C.M. Martin, 2002 Workshop on the Physics and Chemistry of II-IV Materials, extended abstracts, San Diego CA.

12. Primary Optical Excitations and Excited-State Interaction Energies in Sexithiophene
    M. A. Loi, C. Martin, H. R. Chandrasekhar, M. Chandrasekhar, W. Graupner, F. Garnier, A. Mura , G. Bongiovanni, Physical Review B 66, 113102 (2002)

13. Optical Spectroscopic Studies of a Soluble Fluorene-Based Conjugated Polymer: A Hydrostatic Pressure and Temperature Study
    S. Guha, J.D. Rice, C. M. Martin. M. Chandrasekhar, W. Graupner, and U. Scherf, Mat. Res. Soc. Symp. Proc. Vol. 708 , BB10.7.1 (2002)

14. Temperature Dependent Photoluminescence of Organic Semiconductors with Varying Backbone Conformation
    S. Guha, J. D. Rice, Y. T. Yau, C. M. Martin, M. Chandrasekhar, H.R. Chandrasekhar, R. Guentner, P. Scandiucci de Freitas, U. Scherf, Physical Review B 67, 125204 (2003) (cond-mat/0206357)

15. Effect of Temperature and Pressure on the Optical Properties of Polyfluorene
    C.M. Martin, S. Guha, M. Chandrasekhar, H.R. Chandrasekhar, R. Guentner, P. Scandiucci de Freitas, U. Scherf, Synthetic Metals 135-136, 261 (2003).

16. Hydrostatic Pressure Dependence of the Luminescence and Raman Frequencies in Polyfluorene

C.M. Martin, S. Guha, M. Chandrasekhar, H.R. Chandrasekhar, R. Guentner, P. Scanduicci de Freitas, U. Scherf, Physical Review B 68 , 115203 (2003).

17. Raman modes in oligophenyls under hydrostatic pressure
    C.M. Martin, Q. Cai , S. Guha, W. Graupner, M. Chandrasekhar, and H.R. Chandrasekhar, Physica Status Solidi (b) 241, 3339 (2004).

18. Structural and spectroscopic investigations of bulk poly (bis(2-ethyl)hexylfluorene)
    B. Tanto, S. Guha, C.M. Martin, U. Scherf, and M.J. Winokur, Macromolecules 37, 9438 (2004).

TABLE OF CONTENTS

LIST OF FIGURES AND TABLES

ABSTRACT

I present a study of the optical properties of poly-para-phenylene and three different side-chain substituted polyfluorene polymers. Each of the different side-chain substitutions directly affects morphology of the polymer, the defect concentration, and the bulk optical and physical properties inherent to the material.

I present an analysis of the Raman spectra under hydrostatic pressures for three *oligo*(*para*-phenylene) materials (*p*-terphenyl, 3P; *p*-quaterphenyl, 4P; and *p*-hexaphenyl, 6P) under hydrostatic pressure up to 80 kbar, with a focus on the 15-25 kbar region where the molecules are known to be forced into a more planar state. Spectroscopic indicators of the degree of non-planarity are found in the intensity ratios and frequency separations of the 1280 cm^{-1} to the 1220 cm^{-1} modes and the 1610 cm^{-1} to the 1600 cm^{-1} modes. The most remarkable feature is the clearly defined change in the slope of the 1220 cm^{-1} in-plane bending mode upon planarization. In contrast, modes in the 1600 cm^{-1} region do not have as clear a two-slope behavior; however, a more sensitive measure of planarization is the frequency difference between the 1610 cm^{-1} and the 1600 cm^{-1} modes, which exhibits a distinct drop before planarization, and a gradual increase thereafter. The resonance conditions that are responsible for the 1610 cm^{-1} mode make the two-slope behavior less pronounced as compared to the 1280-1220 pair of modes. The intensity of the Raman modes from all three oligophenyls also indicate planarization: the intensity of the 1280 cm^{-1} mode

decreases sharply relative to the 1220 cm^{-1} mode until the molecule planarizes, and increases slowly thereafter.

I present studies of the photoluminescence (PL) and Raman modes of polyfluorene (PF2/6) under hydrostatic pressures of 0-120 kbar at room temperature. The distinct PL with associated vibronics observed at atmospheric pressure blue shifts and changes dramatically around 20 kbar, above this pressure a broad peak at about 2.3 eV, associated with the keto defect, begins to dominate the PL. Raman modes observed are the 1417 cm^{-1} mode from the C-C stretch within the monomer, the 1342 cm^{-1} and 1290 cm^{-1} modes from phenyl rings connecting the monomer units, and the 1600 cm^{-1} modes from the intra-ring C-C stretch. All Raman modes analyzed shift to higher energies with pressure. Some of the phonon lines exhibit an antiresonance effect at higher pressures that is indicative of a high electron phonon interaction between the Raman phonons and the (real) PL transitions.

1 Introduction

1.1 Introduction to organic semi-conductors

For several years now conjugated organic molecules have been very promising active materials for low cost, large area optoelectronic and photonic devices such as light emitting diodes.[1] The high charge carrier mobility due to the π-orbital overlap of neighboring molecules dictates the conductive properties of these materials, thus allowing the creation of conducting or semi-conducting polymers. The wide band gap organics have been of particular interest for organic displays requiring blue light emission, such as an excitation source for color conversion to red, green, or white light by color-changing media such as fluorescent dyes.[2] In recent years rapid development has occurred in the applications of organic materials in devices such as OLEDs, diode lasers, transistors, and photodiodes.[3]

Since the degree of π-orbital overlap dictates many of the electrical and optical properties of organic materials it is important to understand the conformation of the material. Optical studies under high pressure allow us to correlate how intermolecular interactions and structural changes impact photo-physical properties without altering the chemical composition of the sample. Oligomers of *para*-phenylene have proven to be a nice model system for emissive molecules and have been utilized as prototype materials for blue organic light emitting diodes.[4-7]

Recently polyfluorene (PF) has sparked particular interest due in part to the extraordinarily large photoluminescence quantum efficiency (55%) compared to

other conjugated polymers/molecules in solid state.[8] These materials are also known to retain a high hole mobility at room temperature.[9,10] Both of these traits increase the technological importance of polyfluorene (PF) and other related conjugated molecules. PFs have been efficiently utilized in organic light emitting diodes (OLEDs).[11]

Some side-group substituted PFs have been shown to exhibit complex morphological behaviors that have interesting implications due to their rich photophysics. The liquid crystallinity of PF derivatives with long alkyl substituents allows fabrication of electroluminescent devices with highly polarized emission[12] that is of potential use for applications requiring polarized emission.[13] Unfortunately devices fabricated from the PF family of materials are known to degrade under operation. The desired blue electroluminescence from the singlet excitons changes to an undesirable 2.1-2.6 eV greenish/reddish emission. Photo-oxidation produces a similar broad emission band in the photoluminescence (PL) spectrum. Initially this red shifted emission had been attributed to aggregation and/or excimer formation in the material.[14,15] Recently, List *et al*.[16] have conclusively shown that the 2.3 eV band is related to emission from keto defect sites (9-fluorenone) in the sample. The fluorenone sites act as guest emitters that can efficiently trap singlet excitons created on the conjugated polyfluorene backbone. Time-resolved PL measurements further show different temporal dynamics for the various peaks in the 2.1-2.6 eV region, indicating that the origin of some of the peaks is due to on-chain emissive defects while other peaks are from aggregates and excimers.[17,18]

In this work I discuss the optical properties of *para*-phenylene and polyfluorene in the context of PL, absorption, and Raman scattering as a function of temperature at ambient pressure and as a function of hydrostatic pressure at room temperature. Hydrostatic pressure enhances intermolecular interaction and changes the molecular geometry without producing chemical changes in the material. The combination of pressure and temperature studies allows investigation of phase transitions in the material. A full understanding of the influence of the intermolecular interactions is crucial since the photoluminescence quantum yield (PLQY) of polymers is known to decrease in the solid state. For example, in methylated ladder-type poly *para*-phenylene (m-LPPP), the PLQY of solution and film are (100%) and (30%), respectively.[19] In decyloxy PPP (DOPPP) PLQY values of 85% in solution and 35% in film are observed.[20] In the solid state the electronic properties of organic materials depend significantly on the three-dimensional interactions. Recent theoretical methods of quantum-chemistry and solid-state physics in conjunction with experimental measurements have provided valuable insight into the electronic and optical properties of both oligomers and polymers.[21,22,23,24] Hydrostatic pressure studies enable the study of the effects of enhanced interaction on aggregate and defect-related emissions in these systems.

An additional interesting feature of PFs is that the backbone conformation is intermediate to that of planar and non-planar conjugated solids. It thus provides an interesting contrast to the planar polymer m-LPPP and the non-planar oligophenyls such as *para*-hexaphenyl (PHP). Previous studies indicate that

enhanced intermolecular interactions under the impact of pressure in conjugated solids typically produce an increased degree of conjugation, destabilization of localized states as in m-LPPP,[25,26] and changes in the ring torsional motion as in PHP.[27] These changes in geometry can be deduced from their influence on electronic and vibronic spectra. PFs also show rich morphological behavior as a function of temperature: the glass-rubber transition and the liquid crystalline phase are induced at elevated temperatures. It therefore makes it an interesting system to study under high pressure since one can test whether any of the high-temperature phases can be induced by the application of pressure alone at room temperature.

1.2 Materials

1.2.1 oligo(*para*-phenylens)

Due to the wide band-gap of the *para*-phenylene PPP, this material has been utilized as the active emissive layer in blue light emitting organic diodes. The number of phenyl rings conjugated together determines the resulting band-gap of the material, as the length of the molecule is increased the band gap decreases.[28] The three oligomers discussed here are *p*-terphenyl (3P), *p*-quarterphenyl (4P) and *p*-sexiphenyl 6P, Figure 1.1. The simplest of this family of oligomers biphenyl, was not included in this study since the band-gap was much larger than the available UV lines from the argon ion laser.

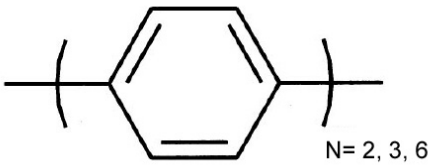

Figure 1.1 Molecular structure of oligo(*para*-phenylene)

The oligomers of PPP are linear fully conjugated molecules, resulting in a delocalization of the excited states and good charge carrier mobility along the molecule. The structure is on average planar, but due to the repulsion of the ortho-hydrogens along the molecule, each phenyl ring sits at a slight angle with respect to the adjacent rings. The angle between adjacent rings has been shown to decrease as the length of the molecule increases.[28] The conformation of the molecule has also been shown to be sensitive to the presence of impurities in the material resulting in a more planar molecule.[29]

1.2.2 polyfluorene (PF)

Several side group substitutions have been made upon the 9,9-dialkyl-PF backbones.[9,30] To keep the solubility high in typical organic solvents, alkyl groups longer than 6 carbon atoms are often used. It has been shown that the side group substitution does not affect the optical and electronic properties in dilute solution.[9] However, this is not the case in the solid state where the nature of the side chains will dictate the physical properties of the polymers such as the glass rubber transition temperature (T_g), the crystal melting temperature (T_m), the crystal formation temperature (T_c), and the liquid crystalline phase transition

temperature ($T_{Cr\text{-}LC}$).[9] If the alkyl side group is not branched, a special highly ordered glassy beta phase, which exhibits extended intrachain π-conjugation, can be achieved by properly thermo cycling the polymer.[9,31,32,33] The formation and stability of the ordered phases are important for long term device applications of the polymer. The extended molecular ordering in the beta phase changes the optical absorption of the material by inducing a bound polaron state on the low-energy side of the absorption spectra,[9] limiting applications in devices such as polymer electron injection lasers. Other consequences of the beta phase are a distinct red shift of absorption and emission peaks with a well-resolved vibronic progression both in absorption and emission due to enhanced molecular alignments. In contrast, the alpha phase shows a well-resolved vibronic progression only in the emission spectrum. If the substituted side chains are branched-alkyl groups then the formation of a beta phase is greatly inhibited; although it has been demonstrated with proper solvent vapor treatment in conjunction with thermo cycling.[9]

The polyfluorene polymers that have been studied here were synthesized by reductive aryl-aryl coupling according to Yamamoto as described by Emil J.W. List et.al.[9,30] This was the preferred synthesis method since it can produce very high molecular weight polymers with low defect concentrations.

The PF monomer unit is depicted in Figure 1.2 showing the connection of the alkyl side groups at the 9,9 position and the conjugation to the adjacent molecules at the 2,7 positions.

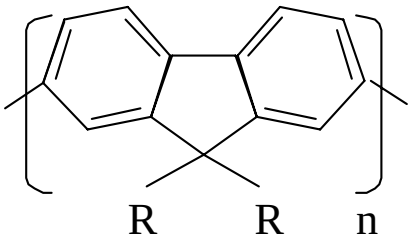

Figure 1.2 Diagram of the PF monomer building block

During synthesis it is possible that not all of the side groups are fully substituted along the polymer chain. These defects will affect the bulk optical properties of the material by acting as dopants changing the bulk electronic properties of the material.[9] The keto defect (2,7-fluorenone) (Figure 1.3) is the substitution of oxygen in place of the alkyl groups.[9] The role of this defect and the impact on the emissive properties has recently been under investigation and debated in the literature.[9,30,34]

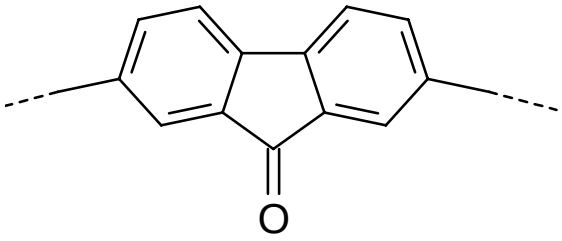

Figure 1.3 Diagram of the keto defect

Upon exposure to UV light in the presence of oxygen, it is possible for the polymer to photo-oxidize and the keto defect concentration to increase. This drastically affects the emissive properties of the polymer. The energy of the emission contributed to the keto defect is 2.3 eV, and the intensity of the peak increases with temperature suggesting a thermally activated charge migration process. From PL measurements on spin-cast films, the thickness of the film

also has an effect on the intensity of the defect emission. The lifetime of this transition has been determined to be about 300 ps.[35]

Since the keto defect is polar, when the PF is dissolved in a high polarity solvent the defect emission is quenched. This has been shown by U. Sherff et.al.[9] and verified by M. Bowerman and D. Derendinger (MU optics class 2002) by looking at the PL of dilute solutions in toluene and dichloromethane. The strong bonding of the solvent to the PF molecules will also affect the properties of drop cast film at room temperature. A film drop cast from toluene has a hard glassy nature whereas when cast from dichloromethane the film is soft and easily manipulated, indicative of an alteration of the T_g due to the solvent interacting with the polymer chains. Currently the defect emission, and therefore the sensitivity of PF to oxidation, is limiting its application in devices. The defect emission has been shown to increase rapidly in electro-luminescent devices operating in air; which once again changes the emission from the desired blue to a green color.[9] The role of solvent quenching and a detailed understanding of the impact the defect has on the emissive properties will be very important for device applications. If the effect of the defects could be quenched after synthesis, less time will be required to ensure the very high purity standards now required. Another important detail yet to be answered is the effect of the solvent quenching on the rate of photo-oxidization of the film and the creation of new defect sites.

PF 2/6 poly [9,9-bis(2-ethylhexyl)fluorene-2,7-diyl]

This is the variety of the PF family that has been most thoroughly investigated by our group.[34] The name PF 2/6 is a short hand notation assigned to make communication easier by noting the side chain substitution, in this case ethylhexyl. The sample details are listed in Figure 1.4.

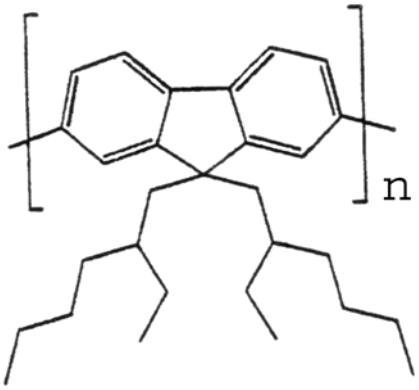

M_n =	83500 g/mol
M_w =	162500
M_w/M_n ratio	~2
T_g	80 °C
$T_{Cr\text{-}LC}$	167 °C
T_m	250 °C

Figure 1.4 The monomer unit for poly [9,9-bis(2-ethylhexyl)fluorene-2,7-diyl], the molecular weight, and thermal transitions for the sample that we have investigated.

PF2/6 forms planar monomer units but has a torsional degree of freedom between adjacent monomer units. The torsional freedom in PF2/6 makes the structure an intermediate case between non-planar oligophenyls and planar m-LPPP. PF 2/6 is semi-crystalline at room temperature with the T_g of the amorphous component at 80 °C, and a crystalline to nematic liquid crystalline phase transition at 167 °C (reverse transition at 132 °C upon cooling).[36] The molecules have been shown to form a C_5 helical conformation at room temperature.[36] Due to the branched alkyl side groups this material is not expected to easily form a beta phase, however it has been shown that with solvent treatment and thermo cycling a highly aligned state can be achieved.[9]

The surface morphology of the PF2/6 powder was investigated using a field emission scanning electron microscope (FESEM). An accelerating voltage of 5 keV with a current of 10 micro-amps was used to minimize electron damage to the sample. As a result of the synthesis and purification, the PF2/6 was provided to us in a meta-stable glassy state, which appears fibrous and is somewhat soft to the touch, Figure 1.5 top. Upon heating above the liquid crystal transition the surface morphology changes significantly. The fibers that were initially apparent are now gone and the surface of the polymer appears much smoother, Figure 1.5 lower panel. Three sets of samples were prepared to ensure no problems with coating materials. One sample was examined as prepared and the others were coated with a thin layer carbon and platinum. The coating is usually necessary when imaging semi-conducting or insulating materials to remove the surface charge on the sample to prevent anomalous images.

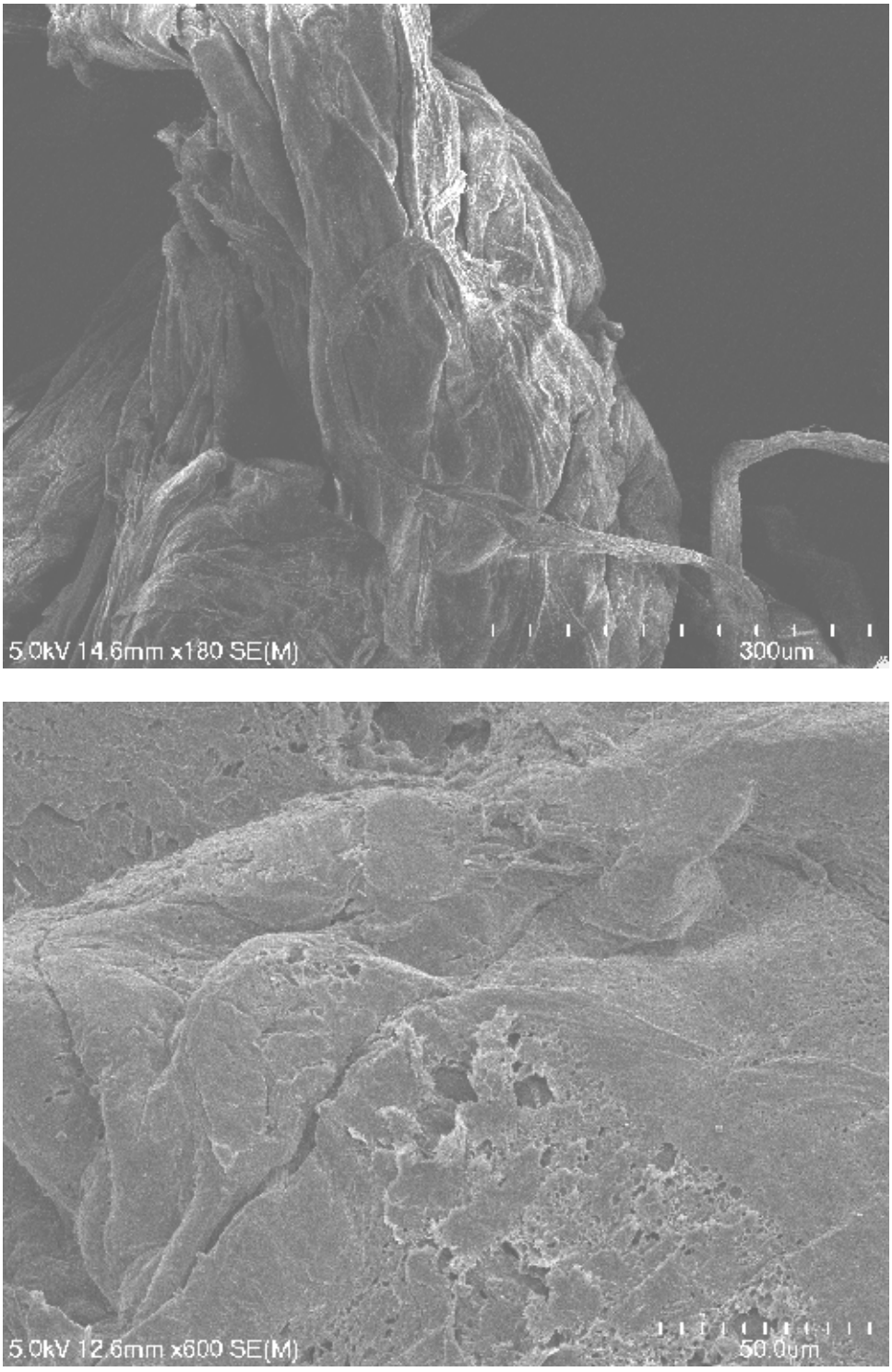

Figure 1.5 SEM image of as prepared PF2/6 in the glassy state (top panel) and after heating to 450 K (bottom panel).

PF 1112 poly [9,9-bis(3,7,11-trimethyldodecyl)fluorene-2,7-diyl]

We worked with two different versions of this polymer; the very low defect concentration dialkylated homopolymer and a copolymer where a 2% (2,7-fluorenone) concentration has been incorporated, figure 1.6. The copolymer serves as a model for photodegeneration-induced defect-rich PF. This model was necessary to prove that the origin of the 2.3 eV emission was due to the defect and not to an aggregate emission due to the close proximity of the adjacent molecules or side groups.

PF 1112 is a branched dialkylated PF similar to PF 2/6. Both exhibit a nematic liquid crystalline phase and have different crystalline nature at room temperature. This allows a very nice comparison between the materials.

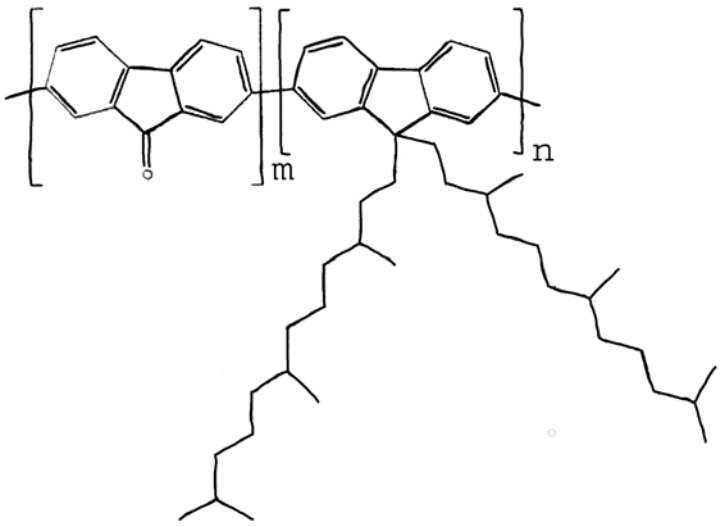

copolymer n= 98%, m=2%	
M_n =	56000 g/mol
M_w =	120000 g/mol
M_w/M_n ratio	~2.2
T_g	Not Yet Determined
T_{Cr-LC}	amorphous

homopolymer n=100%	
M_n =	90000 g/mol
M_w =	200000 g/mol
M_w/M_n ratio	~2.2
T_g	68 °C
T_{Cr-LC}	amorphous

Figure 1.6 poly [9,9-bis(3,7,11-trimethyldodecyl)fluorene-2,7-diyl] or poly [9,9-bis(hexahydrofarnesyl)fluorene-2,7-diyl]

A DSC measurement has not yet been recorded for the copolymer but it is expected that the glass rubber transition temperatures should be similar to (or slightly higher than) the homopolymer. This material is fully amorphous at room temperature, but also forms some extended ordered phases that are frozen at T_g. Due to the non-crystalline nature of the material, liquid crystalline phase transitions are not detectable using DSC.

PF Ethylhexoxy poly [9,9-bis(4-(2-ethylhexoxy)phenyl)fluorene-2,7-diyl]

This is the most recently synthesized of all of these samples. Due to the phenyl rings in the side group, some nice comparisons can be made to mLPPP and other hex side group polymers. As synthesized this sample inherently has a very low keto defect concentration; once again to confirm the role the defect sites and side groups play in the emissive properties. The DSC for this material has not yet been recorded therefore no information about the phase transitions is available.

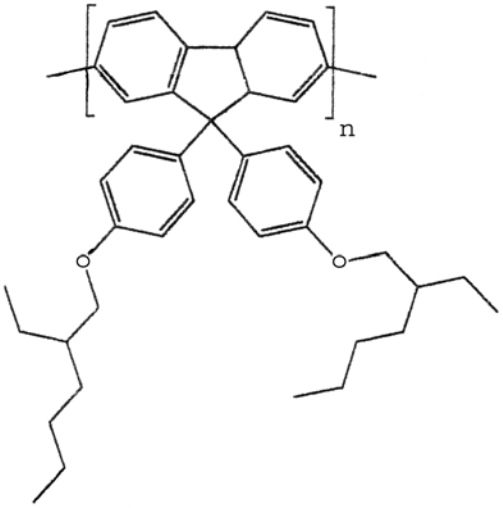

M_n =	209000 g/mol
M_w =	456000 g/mol
M_w/M_n ratio	~2.2
T_g	Not Yet Determined
T_{Cr-LC}	Not Yet Determined

Figure 1.7 poly [9,9-bis(4-(2-ethylhexoxy)phenyl)fluorene-2,7-diyl]

1.3 References

[1] Organic electronics: introduction, J.M. Shaw and P.F. Seidler, IBM J. Res. & Dev. **45**, 3 (2001).

[2] S. Tasch, E. J. W. List, C. Hochfilzer, G. Leising, P. Schlichting, U. Rohr, Y. Geerts, U. Scherf, and K. M¨ullen, Phys. Rev. B 56, 4479 (1997).

[3] For a review see "*Organic electronics: introduction*", J.M. Shaw and P.F. Seidler, IBM J. Res. & Dev. **45**, 3 (2001); Handbook of Conducting Polymers, edited by T.A. Skotheim, R.L. Elsenbaumer and J.R. Reynolds, Marcel Dekker, Inc. (1997).

[4] C. Hosokawa, H. Higashi, T. Kusumoto, Appl. Phys Lett. 62, 3238 (1993).

[5] W. Graupner, G. Grem, F. Meghdadi, Ch. Paar, G. Leising, U Scherf, K. Muellen, W. Fischer, F. Stelzer, Mol. Cryst. Liq. Cryst. 256, 549 (1994).

[6] Handbook of Conducting Polymers 2nd ed. edited by T.A. Skotheim, R.L. Elsenbaumer, and J.R. Reynolds, Marcel Dekker Inc., New York, (1997).

[7] S. Tasch, C. Brandstaetter, F. Meghdadi, G. Leising, L. Athouel, G. Froyer, Adv. Mater, 9, 33 (1997).

[8] A.W. Grice, D.D. C. Bradley, M.T. Bernius, M. Inbasekaran, W.W.Wu, and E.P. Woo, Appl. Phys. Lett. **73**, 629 (1998).

[9] U. Scherf, Emil J.W. List, Semiconducting Polyfluorenes – Towards Reliable Structure-Property-Relations, Adv. Matter, 14, No. 7, (2002)

[10] M. Redecker, D.D.C. Bradley, M. Inbasekaran, and E.P. Woo, Appl. Phys. Lett. **73**, 1565 (1998).

[11] M. T. Bernius, M. Inbasekaran, J. O'Brien, and W. Wu, Adv. Mater. 12, 1737 (2000).

[12] T. Miteva, A. Meisel, M. Grell, H.G. Nothofer, D. Lupo, A. Yasuda, W. Knoll, L. Kloppenburg, U.H.F. Bunz, U. Scherf, and D. Neher, Synth. Met. 111, 173 (2000).

[13] M. Grell, D.D.C. Bradley, G. Ungar, J. Hill, and K.S. Whitehead, Macromolecules 32, 5810 (1999).

[14] V.N. Bliznyuk, S. A. Carter, J.C. Scott, K. Klrner, R.D. Miller, and D.C. Miller Macromolecules32, 361 (1999).

[15] K.H. Weinfurtner, H. Fujikawa, S. Tokito, and Y. Taga, Appl. Phys. Lett. 76 2502, (2000).

[16] E.J.W. List, R. Guentner, P. S. de Freitas, and U. Scherf, Adv. Mater. 14, 374 (2002).

[17] J.M. Lupton, M.R. Craig, and E.W. Meijer, Appl. Phys. Lett. 80, 4489 (2002).

[18] L.M. Herz and R.T. Phillips, Phys. Rev. B 61, 13691 (2000).

[19] S. Tasch, A. Niko, G. Leising, and U. Scherf, Appl. Phys. Lett. 68, 1090 (1996).

[20] Y. Yang, Q. Pei, and A.J. Heeger, Appl. Phys. Lett 79, 934 (1996).

[21] D. Beljonne, Z. Shuai, R.H. Friend, and J.L. Bredas, J. Chem Phys. 102, 2022 (1995).

[22] J. Cornil, A.J. Heeger, and J.L. Bredas, Chem. Phys. Lett. 272, 463 (1997).

[23] F. C. Spano, J. Chem. Phys. 114, 5376 (2001).

[24] P. Puschnig and C. Ambrosch-Draxl, Phys. Rev. Lett. 89, 056405-1 (2002).

[25] S. Yang, W. Graupner, S. Guha, P. Puschnig, C. Martin, H. R. Chandrasekhar, M. Chandrasekhar, G. Leising, C. Ambrosch-Draxl, U. Scherf, Phys. Rev. Lett. 85, 2388 (2000).

[26] M. Chandrasekhar, S. Guha, and W. Graupner, Adv. Mater. 13, 613 (2001).

[27] S. Guha, W. Graupner, R. Resel, M. Chandrasekhar, H.R. Chandrasekhar, R. Glaser and G. Leising, Phy. Rev. Lett. 82, 3625 (1999); *ibid*, J. Phys. Chem. A 105, 6203 (2001).

[28] G. Heimel, D. Somitsch, P. Knoll, and E. Zojer, J. Chem Phys. Vol 116, 24, 2002.

[29] H.W. Furumoto and H.L. Ceccon, IEEE J. Quantum Electron. 6, 262, 1970.

[30] Emil J.W. List, R Guentner, P. Scanducci de Freitas, U. Sherf, On the Role of keto Defects for the Emission Properties of Polyfluorene-Type Materials, prepublication communication. 2002.

[31] A.J. Cadby, P.A. Lane, H. Mellor, S.J. Martin, M. Grell, C. Giebeler, D.D.C. Bradley, M. Wohlgenannt, C. An and Z.V. Vardeny, Phys. Rev. B. **62**, 15604 (2000).

[32] M. Ariu, D.G. Lidzey, and D.D.C. Bradley, Synth. Met. **111-112**, 607 (2000).

[33] M. Grell, D.D.C Bradley, M. Inbasekaran, G. Ungar, K.S. Whitehead, E.P. Woo, Synth. Met. 111-112, 579 (2000).

[34] S. Guha, J.D. Rice, C.M. Martin, w. Graupner, M. Chandrasekhar, H.R. Chandrasekhar, U. Scherf, Mat. Res. Soc. Symp. Proc. Vol 708 (2002).

[35] L. M. Herz, R. T. Phillips, Phys. Rev. B. 61, 13691 (2000).

[36] U. Scherf and E.J.W. List, Adv. Mater. 14, 477 (2002).

2 Experimental Methods

2.1 The Diamond Anvil Cell and High Pressure Physics

Experimental work in high pressure physics was initiated in the late 1940s and increased rapidly over the next two decades peaking during the early 1970's. Early in the development of the field the study of crystallography and phase transitions in metals fueled the development of tools needed for high pressure work. A key researcher that developed and patented many of the first high pressure experimental devices was H. Tracy Hall.[1] A detailed review of the history and landmarks of the field is presented by Tracy Hall in chapter 2 of High Pressure Techniques.[2] The Tracy Hall Foundation maintains an online database of high pressure research and the developments in the field.[3]

Many of the early designs of pressure devices required large pistons or multiple anvils to develop the hydrostatic pressures. In 1973 Leo Merrill and William Bassett published a review of a new "Miniature diamond anvil pressure cell for single crystal x-ray diffraction studies."[4] The newly developed pressure cell could be held in the palm of one hand and is highly permeable to x-rays due to the choice of construction materials beryllium. One of the limitations of the older designs for x-ray studies was the angle of accessibility through the cell. With the proper gasket material the newly designed pressure cell had an angle of accessibility of approximately 55^{o}.[4] This design enigma coupled to the advances on the application of fluids and gases as pressure mediums allowed the rapid development of numerous experimental techniques. After just a few years of development Tracy Hall commented, "…there are as many variations on the MB

design as there are high pressure researchers."[2] For a more thorough review of the history and application of the diamond anvil cell I recommend the works of A. Jayaraman,[5,6] W.C. Moss, and K.A. Goettel.[7] Several former students of both Dr. Meera Chandrasekhar and Dr. H.R. Chandrasekhar include overviews of the use of the diamond anvil cell in their thesis work: Dr. Uma Devi Venkateswaran, Dr. Mark Boley, Dr. Rockwell, and Dr. Q. Cai.

The basic construction of the Merrill-Basset diamond anvil cell (DAC) is two parallel triangular shaped beryllium copper plates, approximately 3.5 cm on each side, that contain the anvils with bolts located at the apexes to adjust the pressure, Figure 2.1.

Figure 2.1 Photograph of a Merrill-Basset type diamond anvil cell. The base of the diamond mounting plates can be seen in the center of the cell and the base of a diamond is visible at the center of the DAC.

Since pressure is force divided by area, a modest force exerted by the plates creates extreme pressures between the small faces of the two diamonds. Force applied by the bolts changes the pressure developed between the diamonds and therefore also in the center of the sample chamber, Figure 2.2. There are three spring loaded cams that are adjacent to the bolts to help stabilize the plates as the pressure is tuned. The flat plates and other components of the cell must be very stiff or they will distort excessively at high pressures. To minimize this each part of the DAC is machined from a solid beryllium copper and then heat tempered to harden the metal.

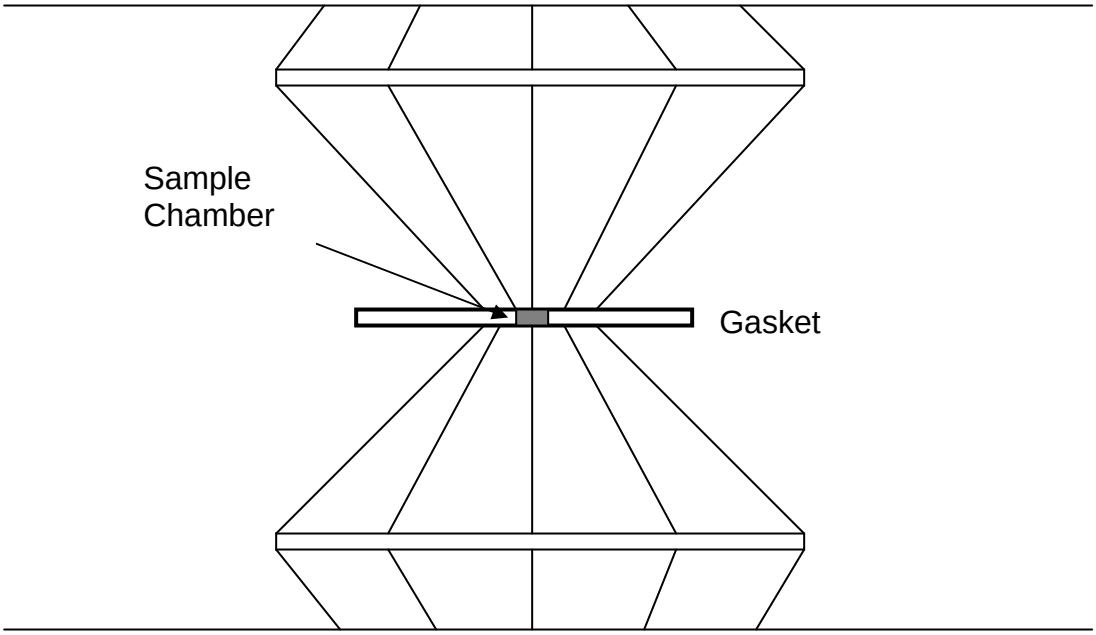

Figure 2.2 Detail of the pressure chamber of a Merrill-Bassett diamond anvil cell showing the pair of diamonds, the gasket, and the sample chamber.

Diamond is an ideal material for the construction of high pressure anvils due to its hardness and optical clarity even under high uni-axial stress. Since the upper pressure limit of the cell is governed by the structural failure of the

diamonds, anvils are created using top quality gem stones with the culet cut short and polished. In the diamond trade associated with this class of stone there are two designations; type I and type II referring to differences in the high energy absorption spectrum of the stones governed by the impurity content of the carbon lattice. For optical applications such as absorption measurements the much more rare and expensive type II diamonds are preferred due to their smooth absorption spectrum that does not change as drastically as type I with applied uni-axial stress. This is complicated by yet another sub-classification of the diamonds into; type Ia (larger aggregates of nitrogen impurities), type Ib (single nitrogen dopants), type IIa (considered pure), and type IIb (including boron impurities).

The before cutting, the diamonds must be selected to minimize the luminescence of the anvil. If the diamonds have an inherent fluorescence it will interfere with photo-luminescence measurements taken inside the cell under pressure. Very pure high grade diamonds are transparent to visible radiation and do not typically have any or very little fluorescence, but due to impurities some stones will fluoresce under UV light. Since the 333 nm line from the argon ion laser is the highest energy excitation typically used in the lab it is convenient for checking the diamonds for photo-luminescent emission. A second criterion used to judge the quality of the diamonds is to look at the intensity and symmetry of the second order Raman signal in comparison to the intensity of the fluorescence. A better anvil will have florescence that is lower than the intensity

of the Raman peak. A stone with lower internal stress will have a more narrow Raman line shape and lower birefringence.

The cut of the diamond and the alignment of the crystal axis will impact the structural integrity of the resulting anvil. As a rule of thumb the more facets the better, but as the number of facets increases so does the cost. Anvils are available with as few as 8 facets and as many as 32, which is highly suggested by diamond merchants such as George Kaplan of Lazare Kaplan Diamonds (LKI). The culet of the diamond can either be cut flat to within ¼ λ or beveled by cutting a 1.5^{o} relief around the edge of the stone reducing the effective diameter of the culet to 1/3 the original size. Beveled diamonds have the benefits of less susceptibility to chipping or scratching on the culet during alignment and allowing the cells to operate at much higher pressures without destroying the diamonds. The beveling of the culet improves the distribution of the stress along the faces of the anvil but greatly reduces the ease of alignment.

Any flaw in the diamond will result in premature failure of the anvil. This includes surface defects and inclusions (carbon dislocations in the lattice) in the stone. To increase the long term survival of the anvil, the diamond lattice should have very low internal stress. Great care must be taken while loading and working with the DAC to prevent damage to the anvils. With proper care, the alignment of the cell, the gasket material, and the pressure medium will dictate the maximum obtainable pressure and not the failure of the anvils.

The seats of the DAC are fabricated out of a disk of the same tempered 2% beryllium copper as the flat plates to prevent the anvils from being depressed

deeply into the seat, figure 2.3. As the diamond sinks too far into the seat, the alignment of the cell will fail at high pressures. Since each stone will impress on the bottom of the seat, each seat is a one time use item. Each mount must be custom machined to accept the specific diamond. The mounting chamber is drilled a few microns larger than the diameter of diamond to allow for thermal expansion of the diamond, but snug enough to prevent the mounting epoxy from seeping to the bottom of the mount. The mounting chamber is cut to the depth of the girdle of the diamond. To allow optical access through the anvil a 30^{o} cone is drilled from the back side.

Figure 2.3 Photographs of the anvil seats in various stages of preparation; on the left is the seat blanks, the center panel has the chamber machined to accept the diamond, and the panel to the right shows the diamond ready for epoxy to hold it in place.

The diamonds are held in the seat using a two part epoxy manufactured by Cummings called Stycast that has a high thermal conductivity. This epoxy base is mixed with about 7% catalyst by weight, but the required catalyst changes as the base ages. Care should be taken not to let any of the epoxy seep under the girdle of the diamond, greatly hampering any attempt to remove the set diamond at a later date, and to keep the top portion of the diamond clear, Figure 2.4. The

seats are mounted into the flats of a cell and a small metal tube is used to press and hold the table of the diamonds firmly against the seats while the epoxy sets. Stycast is soluble in ethanol but extended time and elevated temperatures can be required to remove the diamonds.

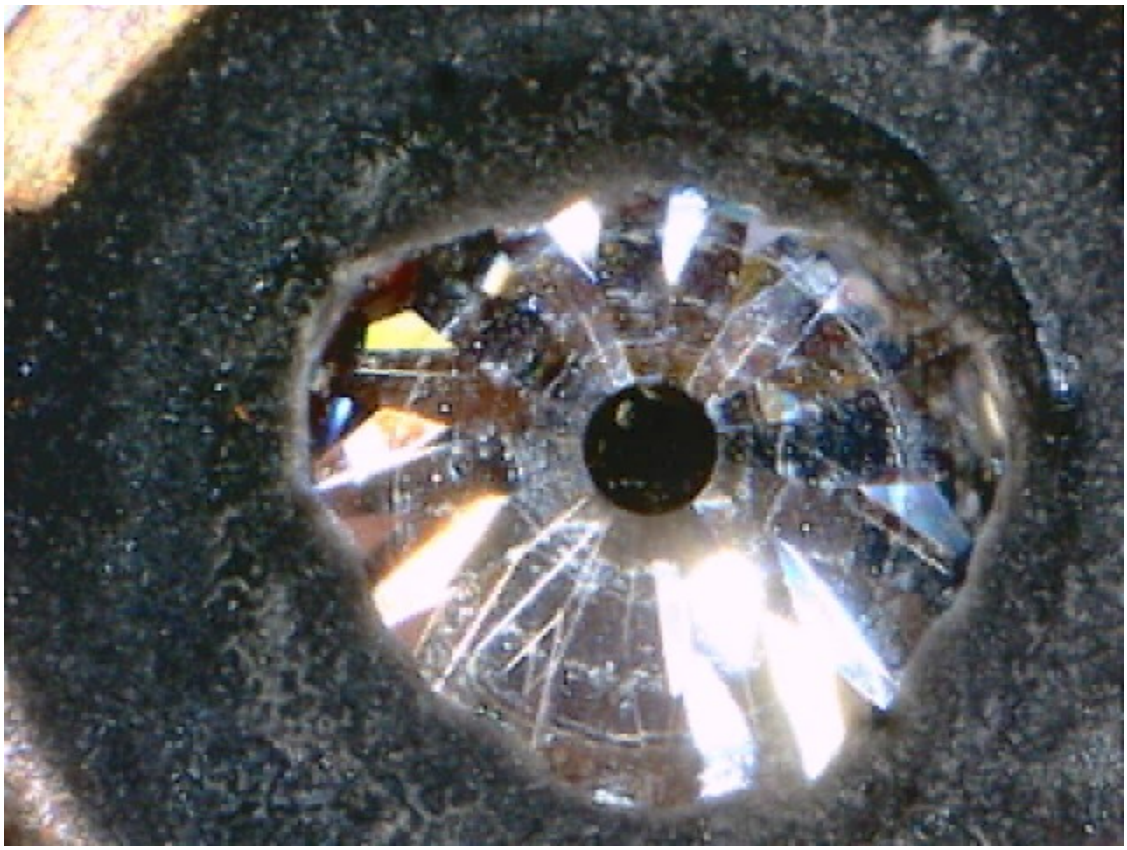

Figure 2.4 Photograph of the diamond epoxied into a seat

Once mounted, the anvils must be aligned relative to one another for the preservation of the structural integrity of the diamonds under high uni-axial stress. The perfect alignment of the cell is less important at lower pressures than at pressures above about 40 kbar where the anvils are more prone to crushing. The alignment of the diamonds is affected in two ways; parallelism and two-

dimensional translation of one of the diamonds. The parallelism of the diamonds is controlled by the three apex pressure application bolts on the cell. The translation is controlled by three small set screws in base of the cell. The alignment of the cell should be verified each time the cell is closed bringing the diamonds in contact and applying pressure.

Before initiating the alignment procedure make sure that both of the diamond seats are fully seated in the plates. A small stainless steel tube, the same diameter of the seat that allows clearance of the diamond in the center, is used between the seats to press them firmly into the mounts. The small set screws that hold the seats in place should be very snug. The preliminary alignment of the top seat should center the diamond in the plate, there is a tool specifically designed for this task. Any time the set screws are loosened, the seats should be reseated in the plate using the stainless tube.

The initial step in any procedure involving bringing the diamonds into contact is to clean and inspect the culet of both anvils. The surface of the diamond should be kept very clean through every step of the procedure of loading and aligning the cell. Lens paper and ethanol or acetone typically works very well for cleaning organic and other debris from the surface. If there is metal or other gasket material adhered to the diamond it can be cleaned off using polishing grit and a jewelers polishing pad or very carefully scraped off using a scalpel under a microscope. If there is question about a defect on the surface of the stone get a second opinion before continuing or applying pressure in the cell. When assembling the DAC bring both plates close together by slowly turning the three

bolts the same amount by hand. When the gap between the diamonds appears to be very small and uniform from the side, place the cell under the microscope to view through the cell and continue uniformly tightening the bolts by hand, Figure 2.5. Fringes formed between the cutlets should be visible. The width of the fringes indicate the degree of parallelism: wide uniform fringes indicate the culets are almost parallel and narrow sharp fringes indicate a larger angle between the faces. If you can't see any fringes apply pressure at each apex bolt one at a time to see if the fringes created in each case are similar; if so then slowly tighten each bolt a bit further until fringes are observed. The goal here is to adjust the apex bolts to remove all of the fringes from view; as the parallelism of the diamonds is perfected the fringes will get wider and then eventually disappear. If beveled diamonds are used in the cell there will be circular fringes surrounding the parallel flat faces.

Once the diamonds are parallel the spatial alignment of the pair must be checked by viewing from the side, Figure 2.5. View the lateral positions of the two diamonds from each of the three sides to check alignment. To fine tune the position of the adjustable diamond the three sets screws can be adjusted. Most of the adjustments will be tightening in small increments with loosing of the bolts being avoided. The required changes are usually very small and with practice the cell can be fully aligned in one hour.

When aligning the diamonds extreme care must be utilized to prevent one diamond from diving into the face of the other creating a defect that could end the life of the anvil. Each time the cell is opened and reassembled you need to clean

and inspect the diamonds again very carefully. When the diamonds are in contact even a modest shock can damage one of the anvils, therefore great care must be utilized when handling the cell.

Figure 2.5 View from the side of the cell under the microscope to verify alignment of the diamonds.

There are some typical problems encountered when aligning the cells especially if the anvils are not perfectly matched. If one of the anvils have been repaired it is likely that that culet is larger or even cut into a slight oval shape and then the center of the diamonds should be aligned. When working with mismatched anvils the maximum pressure of the cell is reduced and the gasket should be watched more carefully for failure since the diamonds will indent the gasket at different rates on each side. Beveled diamonds present a special challenge during alignment since the actual culet is greatly reduced in size and there is a small gap at the edges of the diamonds.

Once the final alignment has been achieved the thickness of the cell needs to be measured at the three apex bolts of the cell. Noting these distances ensures the surfaces of the culets can be kept parallel during use. When determining these apex distances it is convenient to make a mark at the spot on the apex to denote the exact position of the micrometer to allow reproducibility. Each corner is numbered on the top plate of the cell. Care should also be taken not to apply any force to the plates with the micrometer skewing the results.

The gasket material that I used was stainless steel shim stock .01 inches (~250 microns) thick but many different types of metal have been used in the past including heat treated inconel steel. The roll of shim stock is first sheered off the roll into ~1 cm strips that then are punched into discs that are about .9 cm in diameter forming the rough gaskets, Figure 2.6. For the punch to work efficiently and to extend the life of the tool, the steel needs to be coated with a thin layer of machine oil. Once stamped the two alignment holes are drilled

through the gasket using cobalt twist drill bits and a micro drill press. The gasket is held in place by a custom jig that has guide holes that match the positioning of the guide pins on the lower DAC seat. After the alignment holes are drilled the gaskets are cleaned first with acetone and then with methanol in an ultrasonic bath to completely remove all traces of the oil.

Figure 2.6 Photograph of the required tooling for producing the DAC gaskets.

To harden the steel in the area between the diamonds the gaskets are pre-compressed to work harden the steel. When pressing the gaskets it is very important to keep the diamonds clean and parallel as the force is exerted. The apex bolts are tightened until the distances are about 0.1 mm below the parallel distance determined during previous alignment procedure. There is a slight flex to the plates as the tension is increased on the bolts so care must be taken not to over tighten the bolts. After releasing the pressure and removing the pressed gasket the thickness inside the depression is measured using specially made

caps that fit the micrometer. The thickness of the gasket will affect the maximum pressure the cell can experience without gasket failure. A thinner gasket will raise the maximum pressure obtainable with the cell by reducing the risk of deformation of the sample chamber, where as a thicker gaskets is much easier to load and there is greater volume within the sample chamber. At higher pressures the thicker gaskets tend to deform more readily into an oval shape as one side of the pressure chamber translates relative to the other. As the gaskets are pressed the top of each gasket should be labeled and the thickness recorded.

Figure 2.7 Pressing the gasket to work harden the material forming the pressure chamber.

The sample camber may be formed in the center of the gasket by drilling by hand or by electro spark vaporization. The Physics Department machine shop has the tooling to blast a hole in the approximately in the center that is about 60-70 micrometers in diameter. This hole can then be enlarged to the desired

diameter, about 125 microns in diameter or at most about 1/3 the diameter of the culet of the anvil. About 30% of the holes that the machine shop blasts in the gaskets are located close enough to the center of the gasket to be of use, the rest are too close to the edge of the gasket to be of use. The edge of the pressure chamber can be beveled and rounded to increase the life of the gasket and extend the maximum pressure obtainable. There is an aluminum jig for holding the gasket in place while working on the gasket/sample chamber under the microscope, Figure 2.8. The gasket is ready for use when the sample chamber is centered, circular in shape, of the proper diameter, there are no metal burrs, and all of the machine oil has been removed by ultrasonic cleaning.

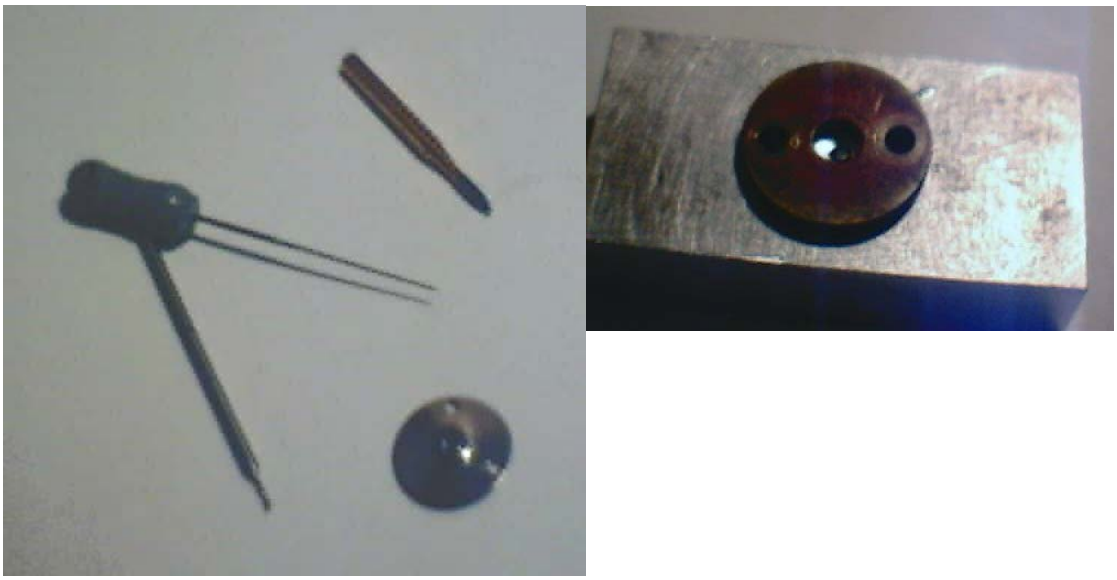

Figure 2.8 Tooling necessary for the preparation of the sample chamber in the gasket. On the left is an assortment of micro-drills and on the right is a block for mounting the gasket while working on the chamber.

When using a cryogenic liquid pressure medium, indium gaskets are necessary to act as a seal to form the vacuum chamber around the diamonds.

This is the chamber that is flushed with argon at liquid nitrogen temperatures to fill the cell with liquid argon. The gaskets are extruded using a ring press by the physics machine shop using pure indium. The material is not altered during use and can be endlessly recycled. The very soft gasket is pressed by hand into channels in the plates of the pressure cell and a new gasket is required each time the cell is loaded.

The vacuum chamber around the diamonds is formed by a stainless steel cylinder with a small capillary tube allowing attachment to a vacuum pump/filling system, figure 2.9. The cylinder is held securely in place by an aluminum plate adhered to the DAC with tacky lab wax, which serves to hold the components in place as the cell is loaded. The height of the cylinder is determined by the sum of the height of diamonds above the seats plus 100 microns. Due to the height requirements/constraints these parts might not be interchangeable between different pressure cells. The seal between the cylinder and the pressure cell is maintained by the indium dam and the epoxy around the anvils.

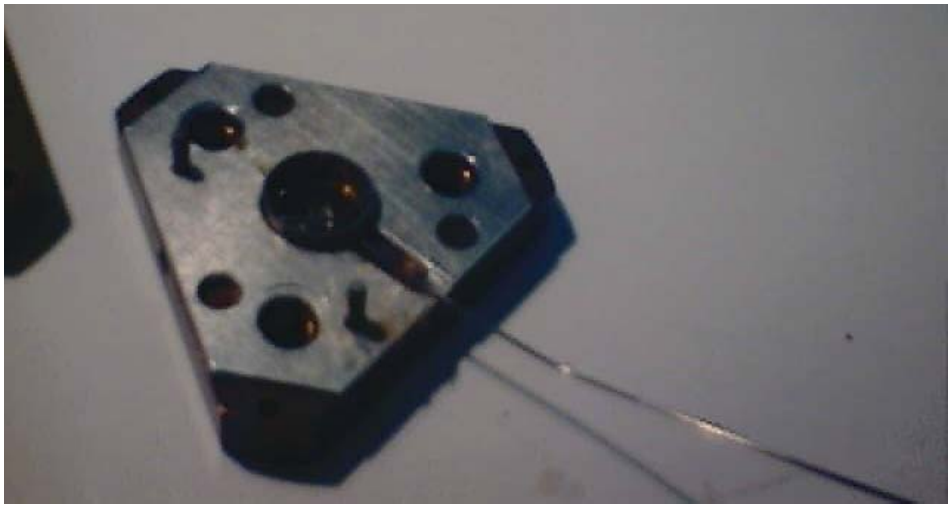

Figure 2.9 Photograph of the bottom plate of the DAC including the aluminum plate, the vacuum chamber, and the capillary filling tube.

While loading the liquid argon, the temperature of the cell and the argon is monitored by using a thermocouple and a volt meter. The Thermocouple junction (copper and constantan wires) is attached to the side of the vacuum chamber and the aluminum plate using tacky wax.

The sample is now ready to be added to the pressure chamber. The sample needs to be sufficiently thin so that it does not contact the diamonds at high pressure, 20-45 microns in each direction is a good starting point. The sample can be either a single crystal, bulk powder or a thin film. Loading thin films has proven to be very difficult in the past. The films can be deposited on the surface of the diamond by drop-casting or by thermal evaporation onto the anvil. After forming the film the outer edge of the sample is removed from the anvil so that the gasket can seal properly. One problem with loading films is that due to differing thermal expansion coefficients of the material and the diamond the film breaks free of the diamond allowing the sample to escape from the pressure chamber. It is often difficult to verify the presence of the film under a visible light microscope as the cell is loaded. Once loaded it is desirable that the film be free floating in the sample chamber, if the film did not break free of the surface after loading the sample might not experience truly hydrostatic pressure.

A small chip of ruby is also placed into the sample chamber allowing the determination of the pressure inside the cell. The ruby and the sample are very small and the electrostatic attraction/repulsion can make placing both of them into the small sample chamber very challenging. The pressure inside the cell is

determined by comparing the energy of the luminescence of the ruby inside to a small chip mounted on the base of the seat.

With the sample and ruby in place the top plate of the cell is slid carefully onto the alignment pins. The bolts with lock washers are carefully turned by hand to bring the diamonds close to the parallel distance. The thickness of the cell must be monitored at the three apex bolts as the faces of the anvils are brought to parallel. The pressure chamber needs to remain open enough to allow the liquid argon to enter the cell. If there is too much clearance the sample or the ruby can escape from the pressure chamber as the argon floods into the cell. The proper distance is determined by summing the parallel distance + the thickness of the gasket + ~ 150 microns. This should compress the indium and seal the vacuum chamber yet allow the flow of gas into the pressure chamber. The presence of the sample and ruby should be confirmed after each manipulation of the cell.

The cell is now clamped into the filling tray to allow cooling by a puddle of liquid nitrogen. Good thermal contact between the cell and the aluminum tray makes the loading process move much more quickly. The capillary tube is attached to the vacuum system and the cell is evacuated. To remove any contaminates in the sample chamber, especially water, it is often necessary to flush the cell with dry nitrogen several times between long periods of pumping on the vacuum. The pressure of the filling system should be brought to above atmospheric pressure with pre-purified nitrogen and held for five to ten minutes to thoroughly flush the system.

The temperature of the cell should be continuously monitored as the cell cools and approaches the freezing point of the argon of 84 K. After the initial cooling of the cell the argon is added to the pressure chamber. When adding the argon to the cell the pressure of the system should be kept above one atmosphere in pressure. As the cell is cooled and the argon condenses into liquid more gas must be added to keep the pressure constant. One problem with this filling technique is if the temperature of the capillary tube is too low the argon will solidify in the tube obstructing the flow. This is mediated by continuously warming the gas and capillary with a soldering iron as the gas fills the vacuum chamber.

As the liquid argon fills the pressure chamber a meniscus should be briefly visible. The position of the sample and the ruby should be monitored in the sample chamber as the cell is filled with the argon. The ruby or samples, especially film samples, are often lost at this step in the loading procedure. Usually by the time the liquid argon fills the sample chamber the view through the cell is obscured by ice formation on the top of the cell.

Once the cell is filled with liquid argon the bolts can be uniformly tightened while the cell is cold to trap the liquid inside. The cell can now be removed from the liquid nitrogen bath and allowed to return slowly to room temperature. Once the cell is warm the gasket and samples should be examined under the microscope. The gasket should have a round hole in it and will appear to be between 15-25% smaller that the initial sample chamber. If the gasket and samples survived the loading process the parallelism is corrected on the cell by

measuring the thickness at the three apex bolts. By tightening any of the bolts the pressure inside of the cell is increased, if this causes the gasket to collapse closed then there was no argon in the cell and the loading process will have to be repeated. The amount of pressure and the hydrostatic nature of the cell should also be determined using the florescence from the ruby in the sample chamber.

The role of the pressure medium inside of the sample chamber is to transform the uni-axial compression of the diamonds into a hydrostatic pressure environment for the samples. Some researchers prefer the use of a cocktail of ethanol and methanol as the pressure medium. The main advantage to this pressure medium is the ease of loading the cell and some of the major disadvantages are sample solvent interaction. For organic polymers samples the inert nature and the useable pressure range of the argon medium is preferred. Argon, which condenses into a liquid at 87 K and freezes at 84 K at 1 atmosphere, freezes at 12 kbar but retains hydrostatic pressures inside the sample chamber up to about 90 kbar.

In practice the upper pressure limits of a specific cell is determined by the size/shape of the diamonds, the condition of the gasket and the solidification point of the pressure medium. The smaller the cutlet of the diamonds the higher the developed pressure will be for a given uni-axial compression of the diamonds. The thickness and the diameter of the sample chamber will affect the response of the gasket to the applied pressure.

Once the cell is loaded it is fairly stable and can be handled carefully. At moderate pressures it can sit for more than a year and not have any problems

with the gasket that result in the loss of pressure. At low and very high pressures there is a risk of the gasket failing resulting in a loss of pressure. When the cell is under pressure the diamonds experience a large uni-axial stress. Even though diamond is very hard, a shock to a diamond under strain can result in a crushed diamond. Care should be taken not to drop or shock the cell during handling.

Typically a pressure cell can be cycled from low to high pressure several times before the gasket begins to fail. As the gasket fails the cylindrical sample chamber slowly crushes shut. Looking through the cell, the sample chamber will look oval in shape as it slowly closes. It is normal for the sample chamber to reduce in volume as the pressure is increased. This occurs as the gasket is extruded out from between the culets reducing the thickness of the gasket and the diameter of the sample chamber. To help prevent deformation of the gasket the tension on each of the three bolts should be increased uniformly. If the sample is too thick or after being at higher pressures the gasket is too thin the sample can experience uni-axial stress as it is crushed between the diamonds. This condition can be detected by an asymmetry in the fluorescence signal from the ruby.

During the loading of the pressure cell a small chip of ruby is included in the sample chamber. The pressure inside the cell is determined by comparing the energy of the luminescence of the ruby inside to a small chip mounted on the base of the seat. Forman et al.[8] determined that the very strong R line fluorescence from ruby, at 694.2 nm and 6928 nm, shifted linearly up to 300 kbar with increasing pressure and could be used for pressure calibration. The rate of

the shift used for pressure calibration is -0.753 cm^{-1}/kbar. The relative intensity of the two R lines are sensitive to the temperature and the line width is sensitive to the hydrostatic environment, since the R lines shift with pressure the line widths are connected to the uniformity of the pressure environment. Measurement of the outside ruby before each Raman measurement also ensures that the calibration of the spectrometer is consistent from one day to the next.

As the temperature of the cell changes the pressure developed within the sample chamber is not constant. This is due to differences in the rate of thermal contraction of the components of the cell as it is cooled. This behavior is much more pronounced at pressures less than 10 kbar, where upon cooling form room temperature to 11 K the pressure change can be as great as seven to ten kbar. If the cell has already experienced high pressure or if the gasket was initially very thin, the pressure change upon cooling is larger. At higher pressures there is a larger static pressure on the components of the cell and the thermal contraction has less of an impact on the pressure. At 40 kbar the change in pressure as the cell is cooled to 11K is less than 2 kbar.

With the extensive help of the Physics department machine shop, the high-pressure optics group led by Meera and H.R. Chandrasekhar has made numerous modifications and refinements to the DAC design that we use. Alignment pins and the precision fit of the mechanical parts results in a superior research tool. Many of the specialized tools necessary for the alignment and use of the cell were developed in house by the specialist in the machine shop.

These specialized tools include tools for; centering and seating the diamond seats aiding alignment, hardware for the fabrication of gaskets, and the necessary vacuum connections for filling the cells.

2.2 Raman Spectroscopy

Raman spectroscopy is a measurement of the vibrational modes of a material using the change of frequency of scattered light.[9,10] Most photons incident onto a surface are scattered elastically or Rayleigh scattered. A small fraction of the incident photons can be inelastically scattered or Raman scattered with a shifted frequency that is shifted by an integer multiple of a normal mode of oscillation of the material or phonon. The frequency of the Raman shift is very sensitive to structural phase transitions and configuration changes of molecules and crystals. If the emerging photon is lowered in energy then it is called Stokes scattering and if the resulting photon is of higher energy it is anti-Stokes scattering. The anti-Stokes scattered is much weaker than the Stokes component due to thermal population of the vibrational states. During Raman measurements the Rayleigh scattered component must be eliminated to allow the much weaker Raman signal to be detected.

The incident laser excitation should be close to, but not above, the band gap of the material being studied to avoid luminescence background. If the energy of the incident laser approaches the band gap of the material being studied there is a large resonant enhancement of the Raman scattering.

The Raman spectra were collected using a modified Spex Triplemate spectrometer. The two stage notch filter assembly was bypassed using two lenses and two mirrors effectively utilizing the final stage of the spectrometer. The benefit to bypassing the filter stage was increased throughput; the down side was an increased sensitivity to the alignment of the optical system. This model of spectrometer has toroidal shaped mirrors in the last stage that help to minimize edge of the grating losses and direct more of the light along the optic axis. A holographic super notch filter was utilized just before the entrance slit of the spectrometer to block the elastically scattered light.

The laser beam path between the laser and the sample consists of some beam steering mirrors, alignment apertures, a laser plasma line filter and focusing lenses. The laser with incident intensity of about 10-20 mW is focused onto the sample directly in front of the entrance slit of the spectrometer.

The pressure cell is attached to a custom made tailpiece at the end of the cryostat. The cryostat has optical access through all 4 sides and the end and is mounted on a 3-axis rotating table to allow alignment of the sample. The temperature of the sample is determined by either a thermal resistor or a thermocouple embedded in the tailpiece a couple of centimeters away from the sample. This distance is not usually a problem due to the high thermal conductivity of all of the components of the cryostat DAC system. The temperature of the system is controlled by Lakeshore thermal control unit driving a thin foil heater attached to the tailpiece.

2.3 Absorption

As photons travel through a material it can be either transmitted, scattered, or absorbed. Absorption occurs when a photon has more than the required energy to promote an electron from the valence band to the conduction band, i.e. when the energy is greater than the band gap. The quantity of the photons transmitted by materials follows the Beer-Lambert law;

$$I=I_0e^{-\alpha t},$$

where I is the transmitted intensity, I_o is the incident photon flux, t is the thickness of the material and α is the absorption coefficient. The quantity optical density is often cited if the thickness of the sample is not known. The absorption coefficient molecules in solution can easily be accomplished using a UV/VIS spectrometer and a standard cuvette at a known concentration.

Absorption spectra were recorded as a function of applied pressure using an Ocean Optics PC2000 Spectrometer with 25-micron slits and a deuterium/halogen light source. A custom mount was fabricated to reproducibly position the pressure cell between the light source and the Ocean Optics Spectrometer.

2.4 Photoluminescence

Photo-excitation of an electron from the valence to the conduction band occurs when a photon of energy greater than the band gap is absorbed by a material. Once an electron is promoted from the valence to the conduction band, creating an electron hole pair, within a given period of time it will recombine with

the hole and return to the lower energy state. The process of this transition can result in the emission of a photon to conserve total energy or through other non-radiative paths such as multi-phonon processes. The radiative emission is photoluminescence (PL) and the emitted photon has the energy remaining from the band to band transition.

The PL from many materials exhibit a progression of emissions called vibronic replicas. The main band to band transition is from the bottom of the conduction band to the top of the valence band but other transitions involving phonons or other vibrational modes are possible. The vibronic replicas are visible due to a coupling of the backbone vibrations to the electronic transitions. The vibronic peaks result from a non-zero overlap of the different vibronic wave-functions of the electronic ground and excited states. The transition highest in energy is the 0-0 transition between the zeroth vibronic levels of the excited state and the zeroth vibronic in the ground state. The 0-1 and 0-2 are transitions between the zeroth vibronic levels of the excited state and the first and second vibronic levels of the ground state, resulting in the creation of phonons. The intensity of the progression of vibronic replicas is determined by the population of the higher levels which is dictated by a Boltzmann distribution

For PL measurements the magnitude of the band-gap determines the energy required for excitation. Some of the narrow band semiconductors like GaAs can be excited using the 514.5nm line from a visible Ar^+ laser. Wide band-gap semiconductors require a ultraviolet light such as the 333nm or 351.1nm lines

from an ultraviolet Ar^+ ion laser. The incident laser intensity must be kept to a minimum to reduce the risk of damaging the samples.

The PL emission is analyzed by energy using a spectrometer. The spectra were recorded with an Ocean Optics PC2000 Spectrometer with 25-micron slits in a backscattering configuration. The Ocean Optics spectrometer system is a modular multi-channel CCD system that is capable of recording across the whole visible spectrum in one shot. The resolution of the instrument is set at the factory and there are no user adjustable parts. The resolution of the system is limited and determined by the pixel density of the CCD, the grating spacing, the slit width and numerical aperture of the fiber used to couple into the device.

The older high resolution Spex Model 1401 spectrometer was also used to analyze the emission. The PL was focused onto the entrance slit of the spectrometer and a thermoelectrically cooled high-voltage photomultiplier tube was used to record the intensity at each wavelength. A computer drive unit coordinates the collection of the data using a photon counter to convert the photo-current to a voltage as the spectrometer scans across the emission. The spectrometer creates data files that are the intensity of the emission at each specific wavelength. The main advantage of this spectrometer is the very high resolution, but the time required for large broadband scans is a major disadvantage.

For optical alignment and low temperature studies the DAC is mounted in a cryostat very similar to the Raman setup.

2.5 These Studies

For ambient pressure measurements the samples were loaded in a cryostat that was evacuated to below 100 mTorr to prevent any photo-oxidative damage. The low temperature measurements were conducted in a closed cycle helium cryostat to allow precise control of the sample temperature. The pressure studies were conducted in a Merrill-Bassett DAC with cryogenically loaded argon as the pressure medium.

The PL and Raman spectra were measured from a powder sample of PF, which has both amorphous and crystalline components, while the absorption and PL were measured from a film. The film was prepared by drop-casting PF2/6 dissolved in spectroscopic grade dichloromethane directly onto a quartz slide or onto the surface of the bottom diamond of the DAC. While the film is loosely attached to the diamond surface, it is not bonded onto it, and therefore experiences hydrostatic pressure in the DAC. All the Raman measurements were carried out with a bulk (powder) sample. This was necessary because the Raman signal from a film is very weak due to the drastically reduced scattering volume.

The spectral data was analyzed using PeakFit and Origin to determine the position, area, and full width at half max of all of the peaks. The results of the numerical fits were then plotted for presentation using Origin.

2.6 Scanning Electron Microscopy

Scanning electron images were collected at the University of Missouri Electron Microscopy Center with the help of Dr. L. Ross using a field emission scanning electron microscope (FESEM) under high vacuum operating at 5KeV. The operating voltage was kept low to minimize the damage induced by the electron beam. To minimize surface charging anomalies, samples were prepared with carbon and platinum coatings which allow the electron current to quickly drain to ground. The carbon coating was deposited using an arc deposition 10 cm from the sample for 1 second creating a uniform coating over the surface. Plasma deposition was utilized to coat the samples with 20 nm of platinum. Comparison of the images collected shows that there are some minor differences between the coated and uncoated samples. The platinum coating seems to have melted some of the delicate structures while increasing the image contrast of the bulk material. Due to the lower deposition temperature the carbon coating seems to have affected the surface morphology less than the platinum. I have shown that the conductivity of the bulk PF2/6 is high enough that coating is not necessary to obtain high quality images.

2.7 References

[1] H. Tracy Hall Foundation. H. Tracy Hall Patent list, http://www.htracyhall.org/hthpatnt.html

[2] Chapter 2, High Pressure techniques, H Tracy Hall, Ibid, pp9-72.

[3] High Pressure/High Temperature Data Center, The H. Tracy Hall Foundation, http://www.htracyhall.org/

[4] L. Merrill and W.A. Bassett, High pressure cell…, Rev. Sci. Instrum., Vol. 45, No. 2, February (1974).

[5] A. Jayaraman: "The diamond anvil high pressure cell", Scientific American, pp. 42-50, April (1984).

[6] A. Jayaraman: "Ultrahigh pressures", Rev. of Scientific Instruments vol. 57, pp. 1013-1031, (1986).

[7] W.C. Moss and K.A. Goettel: "Finite Element Design of Diamond Anvils", Applied Physics Letters vol. 50, pp. 25-27, (1987).

[8] R.A. Forman, G.J. Piermarini, J.D. Barnett, and S. Block, Science, 176, 284 (1972).

[9] Optical Characterization of Semiconductors, Sidney Perkowitz, Academic Press, (1993).

[10] Introductory Raman Scattering, John R. Ferraro, Kazuo Nakamoto, Academic Press, (1994).

3 Experimental Results

3.1 Oligophenyls

In the oligophenyls, the hydrogen in the ortho-positions on adjacent rings repel, causing the adjacent phenyl rings to twist.[1] Since a twist in both directions in equally probable, torsional oscillations can take place between the two possible configurations, described by a *W*–shaped potential.[2] The nature of the torsional motion is determined by at least two influences: the intramolecular repulsion between the ortho-hydrogen and the tendency towards planarization of a π-electron system due to resonance interactions.[3,4] Thus, due to the interacting π-electron system the inter-ring angle decreases with increasing oligomer length.[4] The inter-ring angle of a given oligophenyl can be tuned by the application of pressure or by the addition of dopants to the sample.[5] Presented here is a comparative low temperature study of the Raman modes in three *oligo*(*para*-phenylene) materials (*p*-terphenyl, 3P; *p*-quaterphenyl, 4P; and *p*-hexaphenyl, 6P) under hydrostatic pressure of up to 80 kbar. The motivation of this study is to investigate how the application of pressure and the planarization process of oligophenyls of differing lengths impact the Raman spectra.

The Raman spectrum of oligophenyls has been described by several authors[6-13] and has been mainly characterized by four intense modes of A_g symmetry for infinite chain molecules. The four modes investigated here are: the C-H in-plane bend near 1220 cm^{-1}, the inter-ring stretch near 1280 cm^{-1}, and the doublet arising from the aromatic ring stretch near 1600 cm^{-1}, and a combination mode of the 610 cm^{-1} and the 990 cm^{-1} modes near 1610 cm^{-1}.[5,11,13]

Spectroscopic indicators of the degree of non-planarity are found in the intensity ratios and frequency separations of the 1280 cm^{-1} to the 1220 cm^{-1} modes[14] and the 1610 cm^{-1} to the 1600 cm^{-1} modes.[11,13,15] The logarithm of the 1280 cm^{-1} to the 1220 cm^{-1} intensity ratio has been found to be inversely proportional to the number of π-conjugated phenyl rings in the polymer chain.[16-18] In 300K pressure studies of 6P the decrease in the intensity ratio of the 1280 cm^{-1} to the 1220 cm^{-1} mode provided evidence for planarization at ~ 15 kbar.[14] These modes provide a clear indication of the planarity due to the change of frequency of the ortho-hydrogen flex mode as the molecule is forced to a more planar configuration. In addition to the intensity changes in the ratio of the 1220 to the 1280 cm^{-1} peak, there are also changes in the frequencies and in the relative intensities of the 1600/1610 cm^{-1} modes as the oligophenyls become more planar.[15]

The Raman spectra from the samples at 1 bar and high pressure are shown in Figure 3.1. All modes shift to higher frequencies as the pressure increases. In all samples the intensity of the 1280 cm^{-1} mode relative to the 1220 cm^{-1} mode decreases rapidly as pressure is increased until it reaches a minimum in the vicinity of 10 kbar, after which it increases again slowly. It is also evident that the intensity of the 1610 cm^{-1} decreases relative to the 1600 cm^{-1}. Both initial decreases in intensity are similar to the change seen as temperature is increased from 10 to 300K in 6P as the molecule becomes on average more plainer.[14] The average inter-ring angle decreases with increasing temperature, from which the activation energy within the W potential was found to be ~45 meV.[14]

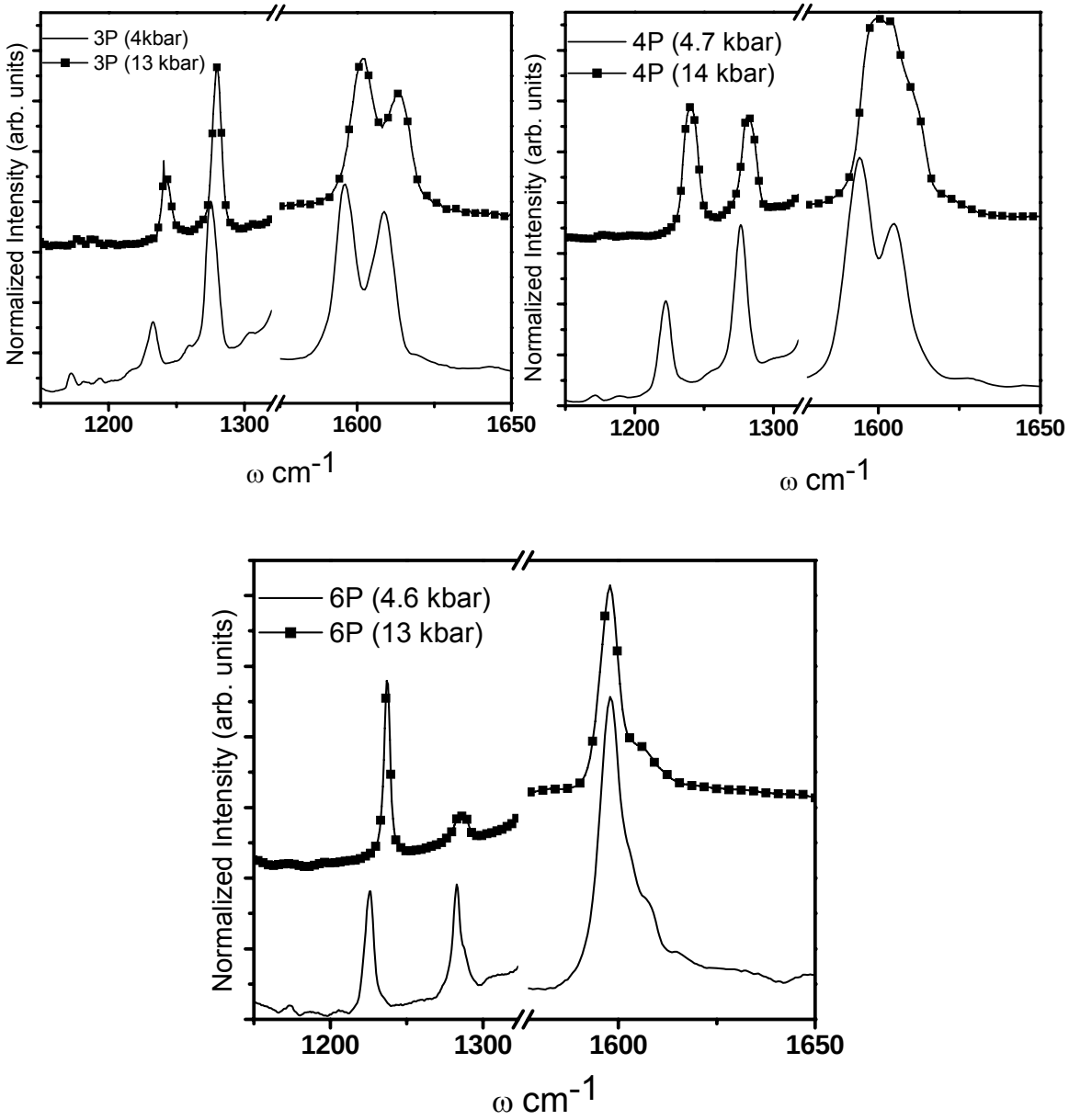

Figure 3.1 The three panels above show the 10K Raman spectra from 3P, 4P, and 6P at approximately 4 and 55 kbar. The individual spectra have been shifted vertically. The diamond peak at 1330 cm^{-1} has been removed for clarity.

The frequencies of the Raman modes as a function of pressure for all three samples are shown in Figure 3.2. The most remarkable feature is the steep increase in the frequency of the 1220 cm^{-1} mode at low pressures, at a rate

approximately five times that of the other three modes. This sharp increase ceases abruptly around 10 kbar for all three samples, and the mode then hardens at a rate somewhat slower than the other three modes (Table 3.1).

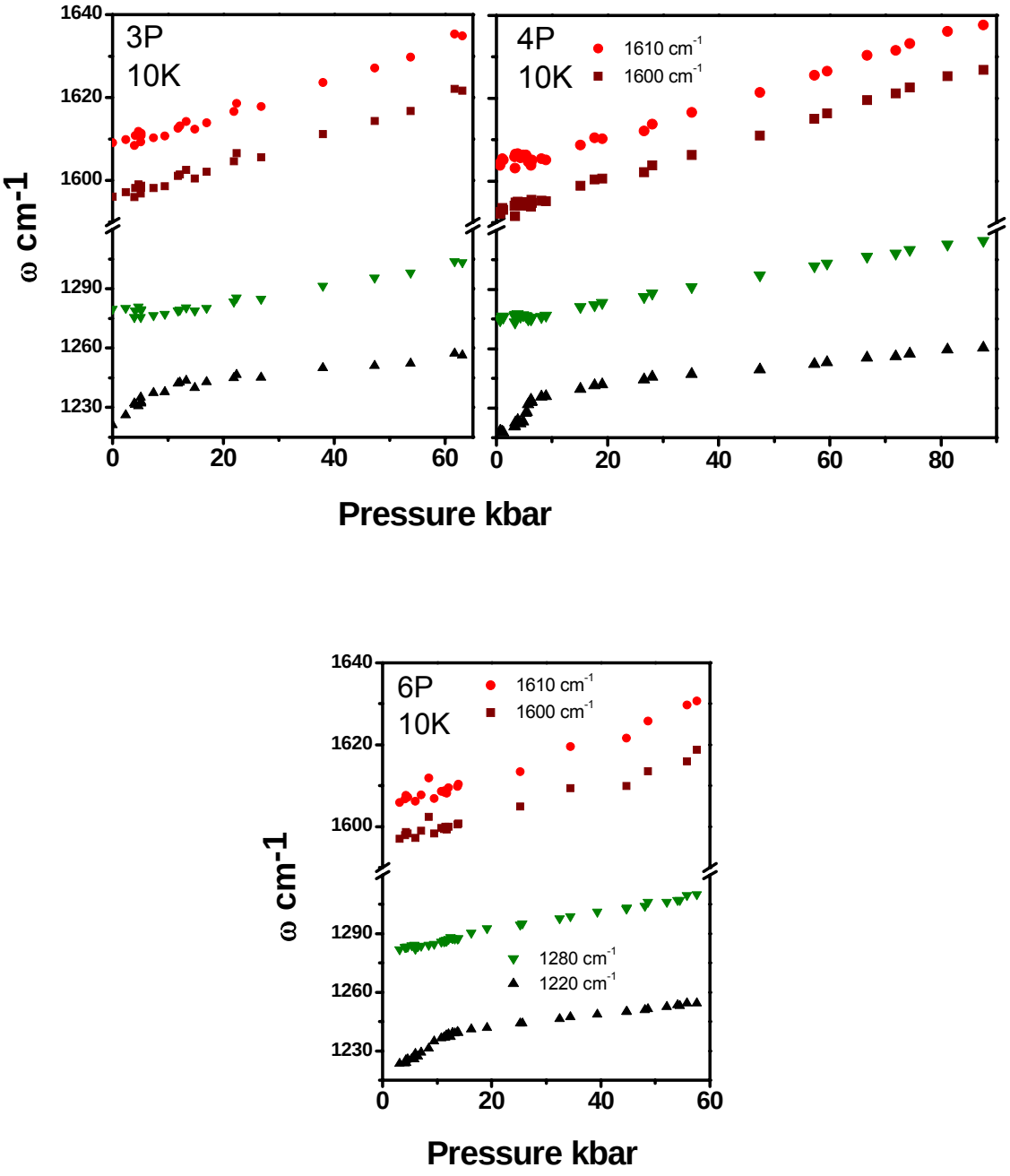

Figure 3.2 The mode frequencies as a function of applied hydrostatic pressure for 3P, 4P, and 6P

	3P	
	ω_0 cm^{-1}	$d\omega/dP$
	1608 ± 1.5	0.42 ± 0.02
	1596 ± 1	0.41 ± 0.02
	1275 ± 2	0.42 ± 0.03
Pre-	1223 ± 3	1.9 ± 0.2
Post-	1239 ± 2	0.27 ± 0.02
P_p	10 ± 1.5 kbar	

	4P	
	ω_0 cm^{-1}	$d\omega/dP$
	1603 ± 1	0.40 ± 0.01
	1592 ± 1	0.40 ± 0.01
	1274 ± 1	0.48 ± 0.01
Pre-	1214 ± 1	2.6 ± 0.2
Post-	1237 ± 1	0.27 ± 0.02
P_p	9 ± 2 kbar	

	6P	
	ω_0 cm^{-1}	$d\omega/dP$
	1604 ± 1.5	0.44 ± 0.02
	1596 ± 1	0.36 ± 0.02
	1281 ± 1	0.50 ± 0.01
Pre-	1217 ± 1.5	1.8 ± 0.1
Post-	1236 ± 1	0.32 ± 0.01
P_p	13 ± 1 kbar	

Table 3.1 The pressure dependence of frequencies of the Raman modes for each sample. Pre- refers to the data points below the planarization pressure and post- refers to the data above the planarization pressure, P_p.

In the low pressure range the rapid decrease in the inter-ring tilt angle affects the frequency of this in-plane bend mode of the ortho-hydrogen more than the other modes making it very sensitive to the degree of planarization. As the angle becomes between adjacent phenyl rings becomes closer to zero (i.e. the molecule becomes more planar) the frequency of the mode changes more slowly. The planarization pressure, P_p, was determined by fitting separately the low and high pressure data of the 1220 cm^{-1} mode to straight lines and determining the pressure at which these fits intersect (Table 3.1).

Upon changing the conformation of PPP from a non-planar benzenoid form to a fully planar quinoid conformation by doping, Marucci et. al.[12] report an upward shift in mode frequencies to 1240 cm^{-1} and 1330 cm^{-1} while the 1600 cm^{-1} mode is not affected.[12] By extrapolating the mode frequencies above P_p back to 1 bar we can determine the inherent frequency of the 1220 cm^{-1} mode to be between 1236 cm^{-1} and 1239 cm^{-1} in the more planar state for the three oligophenyls, in good agreement with the 1240 cm^{-1} predicted for the fully planar quinoid conformation. The impact of molecular planarization on the 1280 cm^{-1} mode is more difficult to determine since the diamond Raman line obscures any peaks that might appear around 1330 cm^{-1}. In any case, the 1280 cm^{-1} mode does not harden toward the 1330 cm^{-1} in a manner similar to the 1220 cm^{-1} mode. Upon changing from the benzenoid to quinoid conformation the inter ring C-C bond changes from a single to a double bond and therefore the bond length shortens slightly, resulting in the hardening of the 1280 cm^{-1} mode to 1330 cm^{-1}. The change in conformation between benzenoid to quinoid requires a

redistribution of the orbital electrons resulting in a polar molecule; therefore it is unlikely that we are achieving this fully planar quinoid conformation by the application of pressure alone.

While the 1600 cm^{-1} and 1610 cm^{-1} modes appear at first glance to shift linearly through the entire pressure range, when we plot the frequency differences as a function of pressure in Figure 3.3, we observe that that the frequencies of these modes are affected by planarization as well. The torsional freedom of the adjacent rings does not affect these modes as directly as it does the C-H flex mode, nor is the effect of the same magnitude. While the 1280-1220 cm^{-1} difference changes by about 20 cm^{-1} for 3P and 4P and about 10 cm^{-1} for 6P in the pressure range below P_p, the difference between the 1610-1600 cm^{-1} modes changes by only about 1.5 to 2 cm^{-1} in 3P and 4P, and is unobservable in 6P due to poor signal to noise ratios in the original spectra. The 1610-1600 cm^{-1} doublet in all three oligophenyls is attributed to a Fermi dyad.[11,13,19] A combination band that arises from two B_1 modes at ~610 cm^{-1} and ~990 cm^{-1} results in a mode of A symmetry that overlaps the fundamental aromatic C-C on-ring stretch modes of A symmetry, resulting in mixed modes of frequency ω+ and $\tilde{\omega}$- at ~1600 cm^{-1} and 1610 cm^{-1}.

Heimel et. al.'s calculations can help shed light on these pressure results.[11,13] From a calculation of the mixing coefficients, they find that the mixing between the fundamental and combination bands decreases with increasing oligomer length. This is caused by the increase in the energy separation between the fundamental and combination modes, and the decrease of the

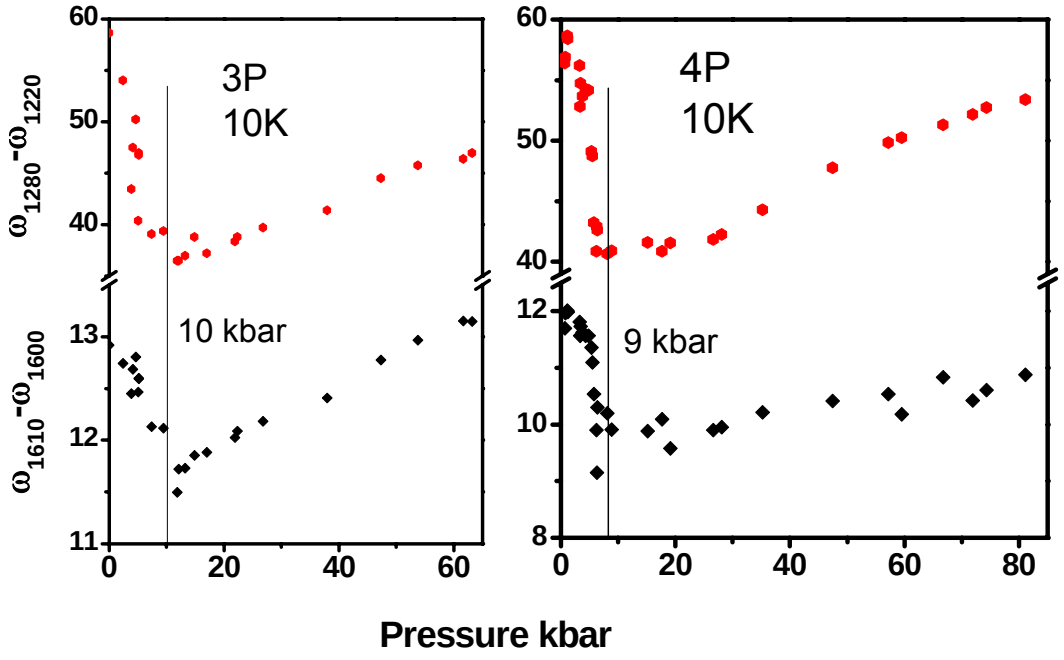

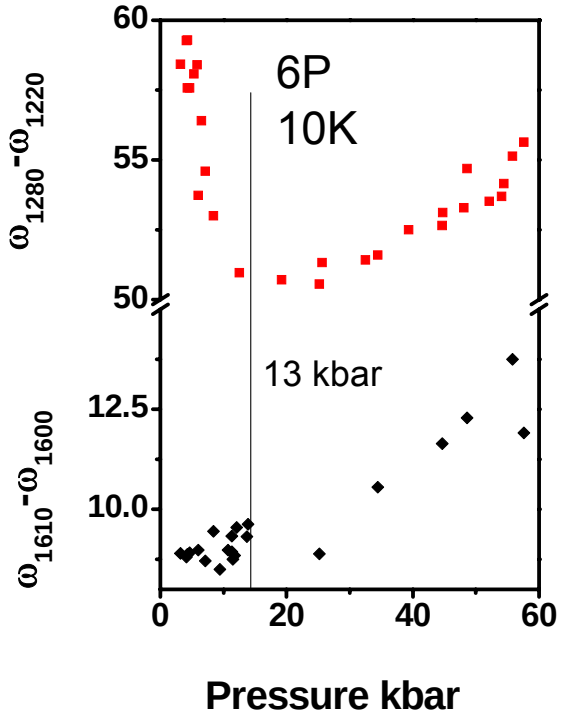

Figure 3.3 The difference in the energy between the 1280/1220 cm^{-1} and the 1610/1600 cm^{-1} Raman modes plotted as a function of applied hydrostatic pressure for 3P, 4P, and 6P.

interaction energy between the modes. Second, while both the fundamental and combination modes contribute to the Raman intensities of ω^+ and ω^-, the fundamental contributes the larger intensity to both peaks. Thus the peak with the smaller intensity, ω^+ (1610 mode), has a stronger component from the combination band, and the ratio of intensities of ω^+ and ω^- is a direct measure of the mixing of the modes. Third, in addition to the oligomer length, an additional parameter that determines mode mixing and consequent intensity redistribution is the inter-ring tilt angle. When one compares Raman spectra from a solution to that of a solid, the intensity of ω^+ decreases going from a solution to a solid, i.e., as the inter-ring angle decreases. The calculations also show that as the inter-ring angle decreases the intensity ratio of ω^+ to ω^- decreases. Thus the mixing is larger at a larger inter-ring angle, where the two resonating levels are close to one another. This decrease occurs for all oligomer lengths, although the intensity ratio is higher at any given angle for 3P than it is for 6P. Fourth, the separation between ω^+ and ω^- is dependent on the mixing and the interring tilt. When the inter-ring tilt decreases, the mixing is reduced, and the separation between ω^+ and ω^- decreases.

This set of pressure data probe both the effect of oligomer length and inter-ring angle. At 1 bar, we observe that the ω^+ - ω^- (1610-1600 cm^{-1}) separation and their intensity ratio, I_{1610}/I_{1600} decreases, as observed in previous studies[7] with increasing oligomer length. As pressure is applied, the inter-ring angle decreases, leading to a decrease in the separation between ω^+ and ω^- as shown in Figure 3.3, and a simultaneous decrease in the intensity ratio of the two

modes, I_{1610}/I_{1600}, Figure 3.4. The minimum in $\omega^+ - \tilde{\omega}^-$ occurs at the same pressures as it does for the 1280-1220 cm^{-1} pair, namely the planarization pressure, P_p. When we compare the three oligomers, we find that $\omega^+ - \omega^-$ decreases from 13 to 11.5 cm^{-1} for 3P and from 12 to 9.7 cm^{-1} for 4P as we increase pressure from 1 bar to P_p. In 6P, where the inter-ring angle is the smallest at 1 bar, the decrease in $\omega^+ - \omega^-$ is expected to be least, and due to signal to noise problems in our spectra is difficult to observe experimentally. In 6P, the intensity of the 1610 cm^{-1} mode is only about 30% that of the 1600 appearing as a shoulder to that peak, making the error bars in the measurement and the fits larger.

The planarization of the molecule is also accompanied by a decrease in intermolecular separation. The volume compressibility of the material is not constant with pressure, nor is it isotropic.[11] As the molecule becomes more planar, the inter-chain separation decreases at a slower pace, which in turn slows down the rate of increase of the C-H bend mode frequency. It is important to note that abrupt changes in $d\omega/dP$ commonly signal a structural phase change in a material. In this case, the changes are completely reversible. The frequencies and intensities of the modes recover their values with no hysteresis as we repeatedly cycle through the planarization pressure.

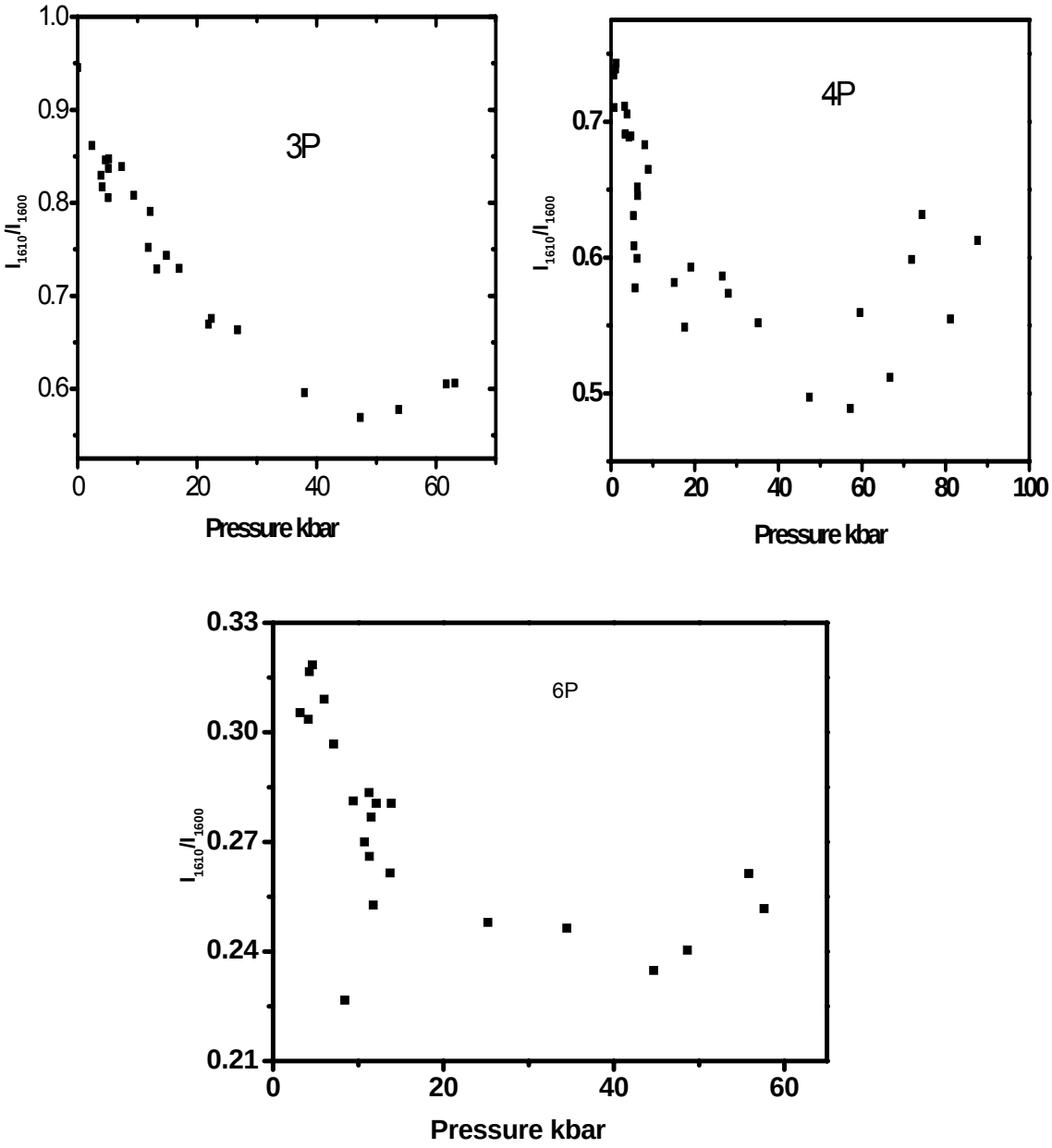

Figure 3.4 The ratio of the intensities of the 1610/1600 cm^{-1} Raman modes as a function of applied hydrostatic pressure for 3P, 4P, and 6P at 10K.

Using high pressure infrared spectroscopy, McCluskey et. al. have shown in studies of 3P and 4P that several IR absorption peaks associated with the out-of-plane C-H bend mode disappear when the molecule planarizes.[20,21] The disappearance of the IR modes has been attributed to a change from a low symmetry non-planar C_{2h} configuration to a higher symmetry D_{2h} of the molecule when planarized. The changes in the symmetries were determined by group theoretical analysis. McCluskey et.al. found 3P to planarize at slightly lower pressures than our data indicates, between two and six kbar versus 10±1.5 kbar, while 4P planarizes at 9±2 kbar.[20,21] These differences may be attributed to the sensitivity of various vibrational modes to the inter-ring tilt angle.

An examination of the ratio of the intensities of the 1280/1220 cm^{-1} modes in all three materials shows an initial drop in intensity up to the planarization pressure and a gradual increase thereafter, Figure 3.5. Above the planarization pressure this intensity ratio remains fairly constant at a given pressure as we scan the temperature from 15K to 300K, indicating that the relatively planarized molecules remain mostly planar. This is a definite indication that the W-type potential of the non-planar oligomer at 1 bar has collapsed to become a more U-shaped potential of a more planar configuration at higher pressures.

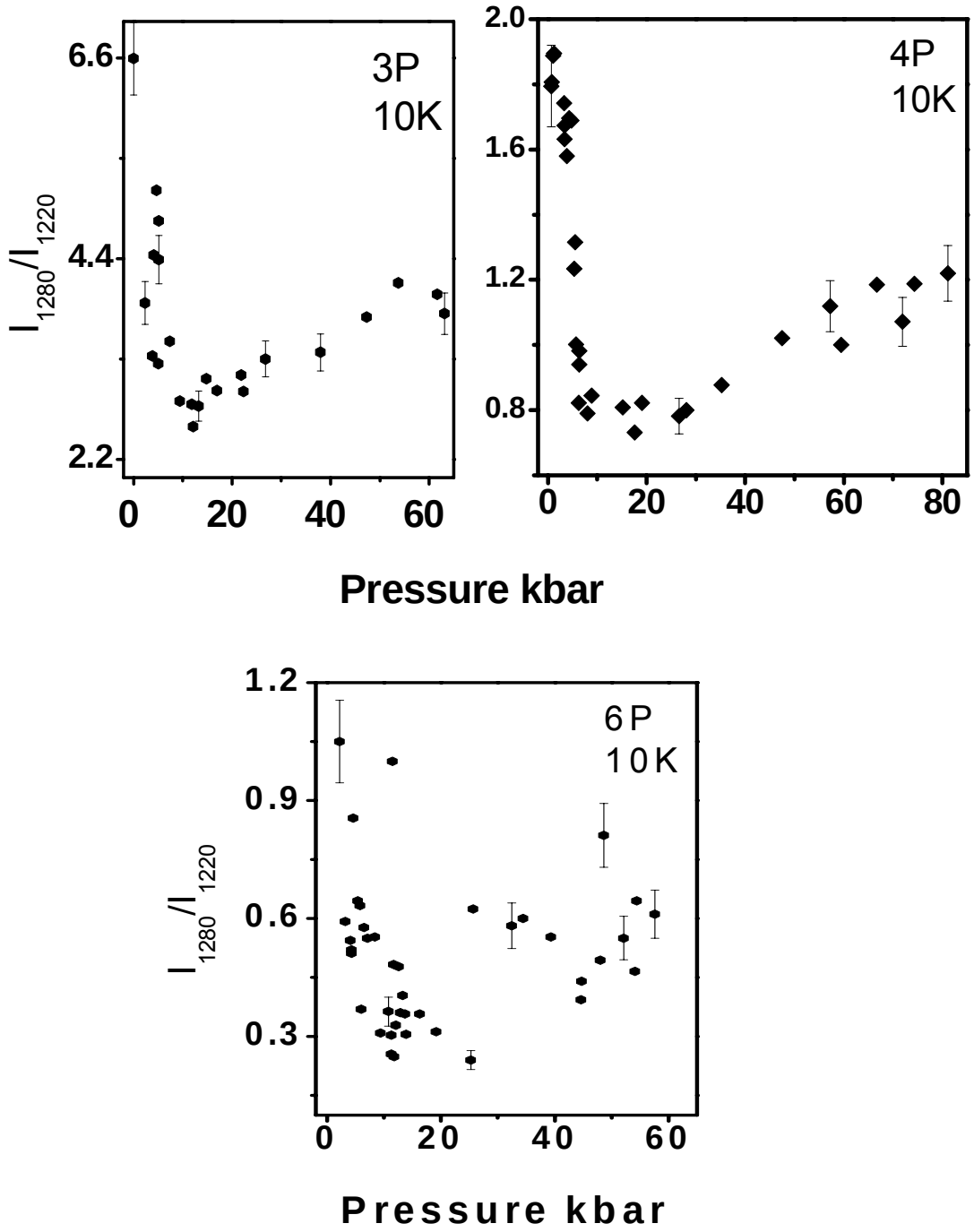

Figure 3.5 The ratio of the intensities of 1280/1220 cm^{-1} Raman modes as a function of applied hydrostatic pressure for 3P, 4P, and 6P at 10K. The typical error-bars are shown in each panel.

3.2 Polyfluorene

3.2.1 Photoluminescence of Polyfluorene

The PL emission from PF 2/6 changes drastically as a function of pressure. At ambient pressure, the π-(* (0-0) transition at about 2.9 eV dominates the emission, creating a strong blue light. Figure 3.6 shows the PL spectra from two PF2/6 films (panel (a) thick film, ~3000 nm; panel (b) thin film, ~100 nm) for a few selected values of temperature. , The vibronic replicas are visible in the PL spectra due to a coupling of the backbone carbon-carbon stretch vibrations to the electronic transitions. The vibronic peaks result from a non-zero overlap of the different vibronic wave-functions of the electronic ground and excited states. The transition highest in energy is the 0-0 transition between the zeroth vibronic levels of the excited state and the zeroth vibronic in the ground state. The 0-1 and 0-2 are transitions between the zeroth vibronic levels of the excited state and the first and second vibronic levels of the ground state, resulting in the creation of phonons. The relative intensity of the 0-0 peak to the 0-1 peak in the thick film (Figure 3.6(a)) is lower than that in the thin film (Figure 3.6(b)) indicating a higher self-absorption in the thick film.

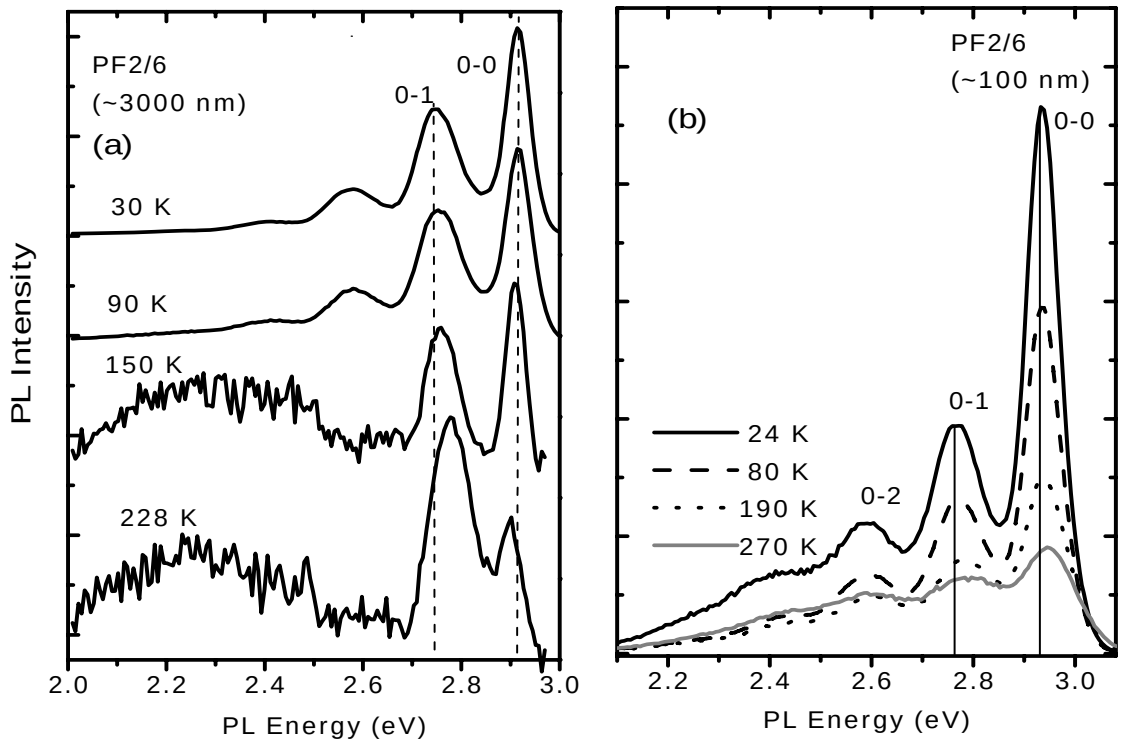

Figure 3.6 PL spectrum of PF2/6 at selected values of temperature for (a) a thick and (b) a thin film. The vertical lines indicate the shift in the transition energies as temperature is increased.

The peak positions were determined by fitting the spectra to Gaussian lineshapes. In the thin film, the main vibronic peaks that are observed at 30 K are the 0-0 peak at 2.93 eV, the 0-1 at 2.77 eV and the 0-2 transition at 2.59 eV. An additional vibronic replica is observed at 2.86 eV between the 0-1 and 0-2 peaks. These values are very close to the energies observed in the thick film and the bulk sample. With increasing temperatures a broad peak is seen to emerge at 2.3 eV around 150 K for the thick film. Recent work suggests that this peak is related to emission from keto defect sites,[24,25] which are due to the inclusion of fluorenone units along the PF backbone. Keto defects can be accidentally incorporated into the π-conjugated PF backbone either during

synthesis, by direct inclusion of a fluorenone unit, due to oxidization of non-alkylated or mono-substituted fluorene sites, or as a result of a photo-oxidative degradation process.[24] The concentration of these defect sites is quite low in our PF2/6 sample since the 2.3 eV emission is absent in the thinner film. The temperature dependence of the 2.3 eV emission suggests that it is a thermally activated process since a weak defect-related emission is only observed for temperatures above 150 K for the thick film.

Figure 3.7 shows the 300 K PL spectrum of a bulk powder sample of PF2/6 at selected values of pressure. The 0-0 transition (2.9 eV) at ambient pressure is barely visible due to self-absorption effects. However, the other vibronics at ambient pressure correlate with the PL data from the film. The most remarkable feature is the emergence of a strong orange emission above ~20 kbar at 2.4 eV, which dominates the spectrum and completely overwhelms the PL from the backbone. This peak has been attributed to a combination of emissions from aggregates and keto defect sites.[24] The broad orange emission comprised of several peaks clearly red shifts with increasing pressures.

The pressure dependence of the backbone PL transitions is difficult to quantify. The apparent position of the 0-0 transition is affected by changes in the absorption spectrum, and the relative intensities of the backbone and aggregate/defect emissions change dramatically as pressure is increased. The vibronic peaks are clearly observable up to 20 kbar above which pressure they appear to remain relatively constant in energy with increasing pressure. This behavior is contrary to the observations in other π-conjugated molecules and

polymers where the backbone emission clearly red shifts under increasing pressures as, for example, in polyacetylene,[26] polythiophene,[27] m-LPPP,[28] PHP,[29] poly (p-phenylene vinylene) (PPV)[30] and MEH-PPV.[31]

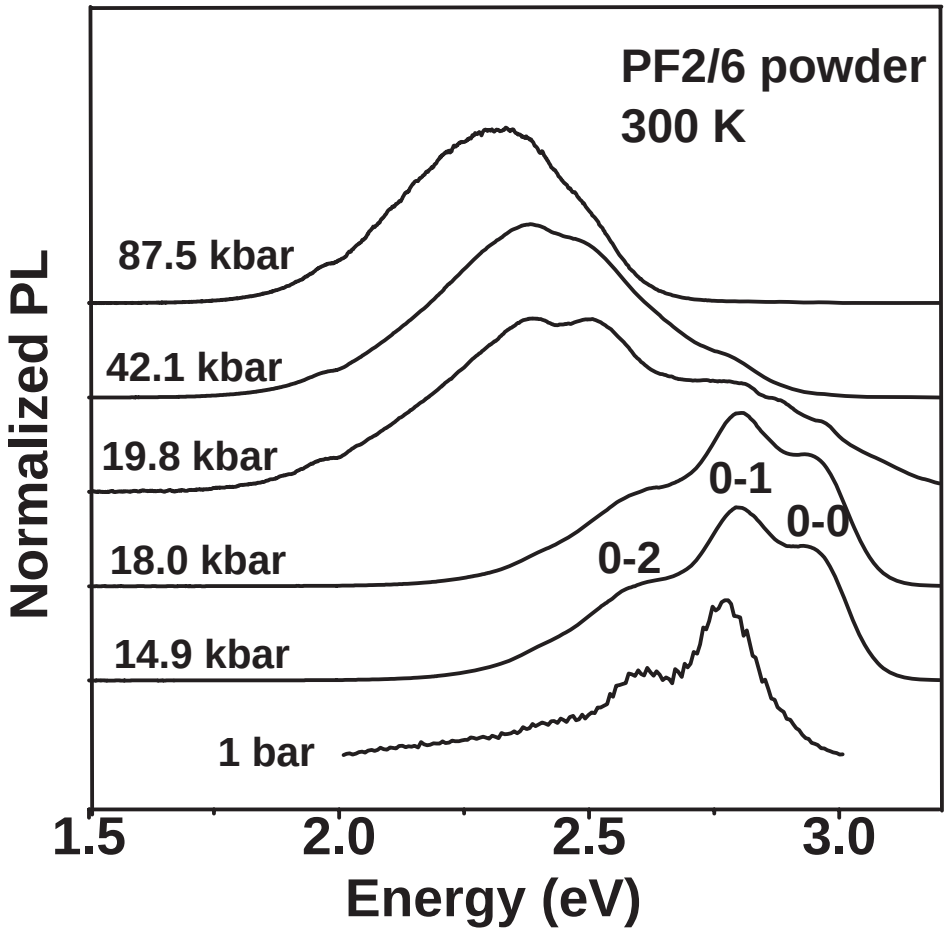

Figure 3.7 PL spectrum of bulk PF2/6 at selected values of hydrostatic pressure. The 1 bar spectrum was measured from a sample evacuated to below 100 mTorr to prevent photo-oxidative damage.

At about 42 kbar there is another change in the PL emission as the relative intensity of the keto emission increases greatly compared to the backbone

emission. At this pressure, there is a large increase in the overall intensity of the PL. These changes in the PL are most likely due to phase transitions in the polymer powder. It has been shown by transport measurements that polymers in a liquid crystalline state exhibit greatly enhanced inter-chain charge carrier mobility.[32],[33] Since this material does exhibit a crystalline to nematic liquid crystalline phase transition,[34] this is a possible explanation for the sudden change in the relative intensities of the emissions. The lifetime of the PL transitions were reported by L.M. Herz et.al. in a recent PRB,[13] where they find that the emission associated with the keto defect has a lifetime of 321±8 ps in comparison to the 3 ps lifetime of the 0-0 transition. Due to the difference in lifetimes the defect site will act as a charge carrier trap localizing the carriers in the long-lived state. This trapping effect in conjunction with enhanced inter-chain charge carrier mobility could account for the significant changes in the PL.[35,36,37]

From the spectra in figure 3.7 it is clear that the 2.3 eV emission is not just one broadband peak but actually several peaks superimposed that shift at different rates. In most of the low-pressure studies published, the PL of the 2.3 eV emission is much weaker in relative intensity than the backbone transitions obscuring the composition of the peak. It is only at high pressure that the more complex composition of the peak is detectable in these measurements.

As can be seen in figures 3.6 and 3.7, some of the PL features shift to higher energies with pressure while some shift to lower energies. The transitions associated with the polymer backbone seem to remain relatively stationary above 20 kbar while the defect emission tends to red shift as the pressure is increased.

This is in direct contrast to the expected red shift of the backbone emission with pressure due to the enhanced conjugation arising from a stronger overlap of π-electron wave functions found in linear oligophenyls.[38] In those studies/models all of the molecules were linear or on average planar in nature; whereas PF 2/6 is a non-planar helical in conformation. Figure 3.8 is a plot of the energies of the PL transitions as a function of pressure.

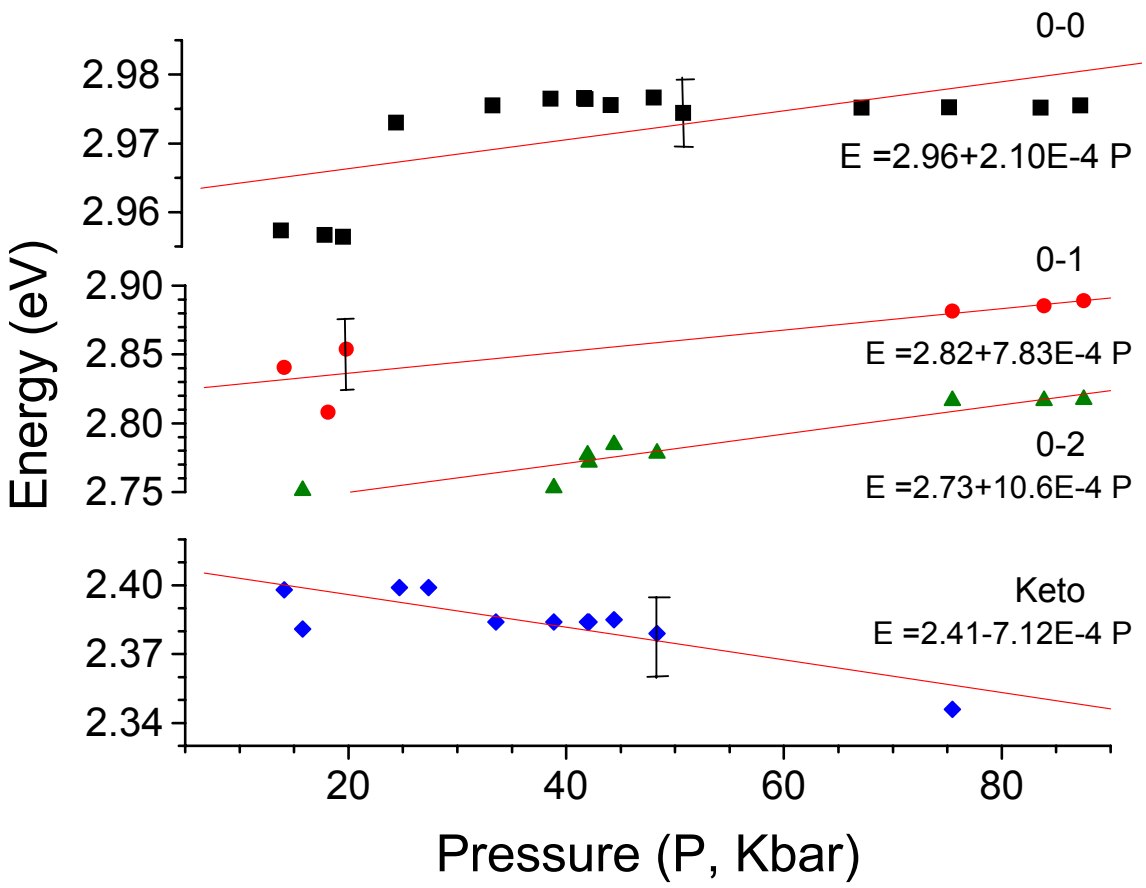

Figure 3.8 Peak Energy versus Pressure for the 0-0, 0-1, 0-2 transitions and the Emission due to the keto Defect from bulk powder PF 2/6.

There seems to be a change in the energy of the 0-0 transition at about 20 kbar, but these spectra are extremely difficult to fit to lineshapes and analyze. In order to clarify the behavior of the backbone emission, which is less affected by

the keto defect and self absorption effects in thin films, we studied the pressure dependence of the PL from a film of PF2/6 that was drop-cast onto the surface of one of the diamonds of the DAC. We systematically measured the PL both for increasing and decreasing pressures. The backbone emission is clearly defined up to 30 kbar, as shown in Figure 3.9. Above 30 kbar the 0-1 and 0-2 can no longer be clearly distinguished; instead a broad peak appears at 2.5 eV with a shoulder at 2.4 eV. The 0-0 vibronic peak is clearly observed up to 42 kbar as shown in Figure 3.9a. As the pressure increases further the 2.5 eV peak dominates the spectrum up to the highest pressures (~100 kbar). Figure 3.5b shows the PL spectra taken while lowering the pressure. Some hysteresis is observed in recovering the low-pressure spectra. In the mid-range (30-45 kbar) the emission in the 2.2-2.5 eV is still dominant and the backbone emission recovers very slowly. Full recovery is not observed until below about 10 kbar.

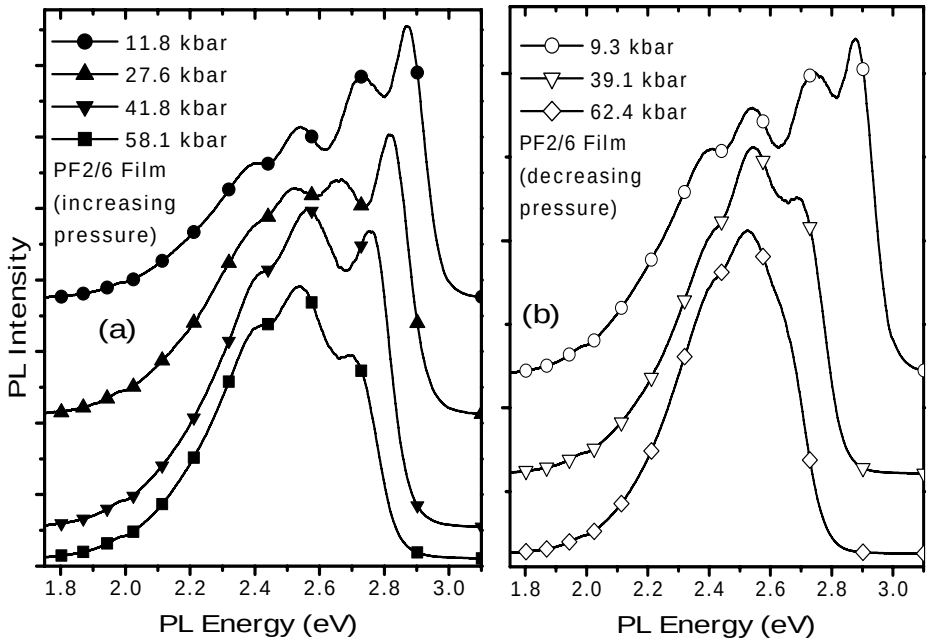

Figure 3.9 Room temperature PL spectrum of a PF2/6 film at selected values of pressure (a) while increasing the pressure and (b) on lowering the pressure.

The PL spectrum of the film was fit using six Gaussian peaks. In Figure 3.10 we show a spectrum at 14.8 kbar, where the vibronics, keto, and aggregate emissions are all clearly observed. The highest two are the 0-0 and 0-1 vibronics. The 2.53 eV peak is close to the 0-2 position. The 2.39 eV peak arises from an aggregate, as does the 2.07 eV peak. The 2.24 eV peak arises from the keto defect. The peak positions of the keto and the aggregate emissions versus pressure for the film sample are plotted in Figure 3.11, and they red shift by 0.6 and 0.3 meV/kbar, respectively, with increasing pressure. The 0-0 and the 0-1 backbone vibronics are clearly visible up to 40 kbar and shift by about an order of magnitude faster (Figure 13a). Similar systematic fitting of the backbone vibronic peaks is difficult for the powder sample, due to the increasing absorbance and the broad keto emission at higher pressures.

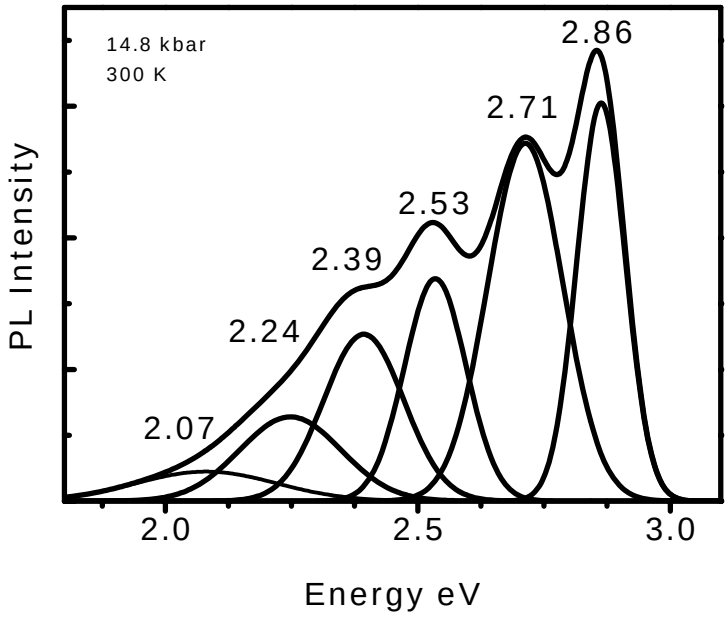

Figure 3.10 The PL spectrum at 14.8 kbar, where the vibronics, keto, and aggregate emissions are all clearly observed. The peaks associated with the lineshape fits for the spectrum are also displayed. The peak positions are in eV.

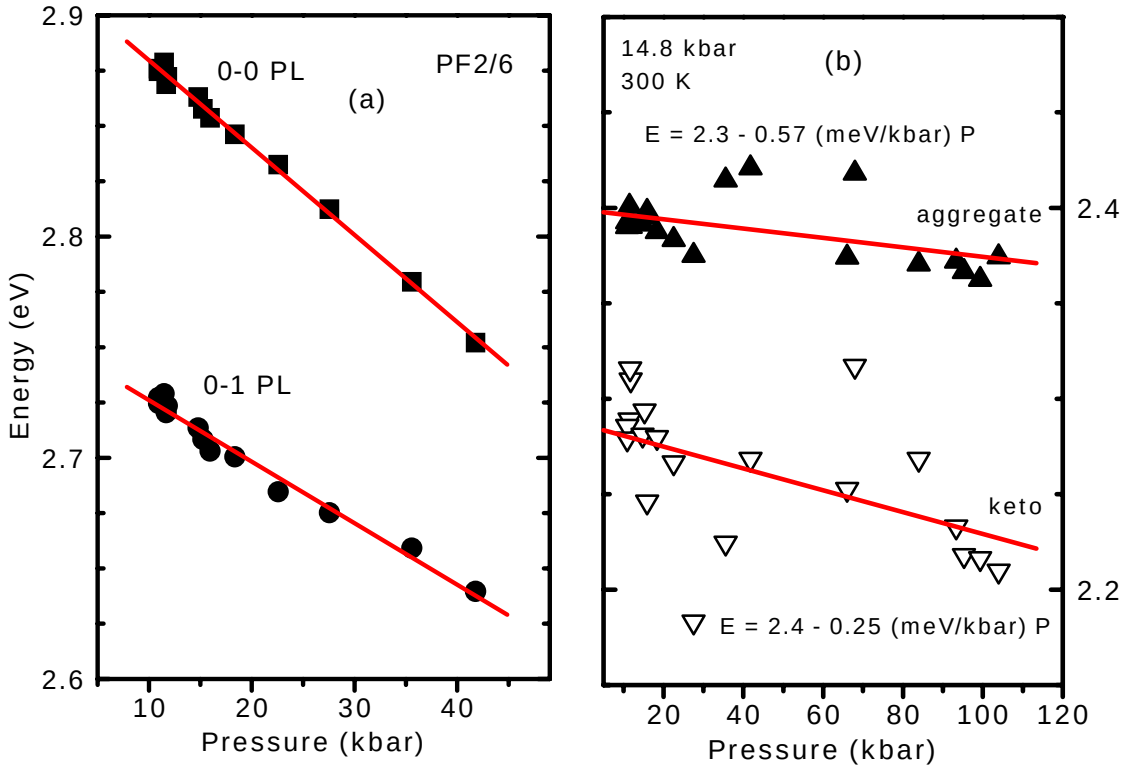

Figure 3.11 Peak positions of the various transitions in a film of PF2/6 as a function of increasing pressure at 300 K. The peak position of the 0-0 and the 0-1 backbone PL as a function of pressure are shown in (a) and the aggregate and the keto peak positions are shown in (b). The slopes of the various transitions are indicated in the figure.

The main impact of pressure on the PL spectrum is the enhanced emission in the 2.1-2.6 eV range which overwhelms the backbone emission of PF2/6 beyond a certain pressure value. Emission in this region has been observed in other works on PF at ambient pressure. Under photo-degradation in 9,9-di-n-hexyl-2,7-dibromofluorene (PDHF), three peaks at 2.2 eV, 2.4 eV and 2.6 eV are observed and have been identified as excimer peaks.[39] Using time-resolved PL spectroscopy, Herz and Phillips[40] find a longer decay time for the 2.15 eV peak, also attributed to an excimer type emission, as compared with other peaks in this region.

Work by List *et al.*[41] conclusively shows that the 2.2-2.3 eV emission is from keto defect sites in PFs. This assignment has been confirmed in a recent work by Lupton *et al.*[42] using time-resolved PL on a range of poly-and oligo-fluorene samples. They attribute the 2.3 eV emission to an on-chain emissive defect, in agreement with the keto-type defect. Further, they observe an enhancement of the 2.6 eV emission with increasing sample concentration concluding that the origin of this peak is due to the formation of interchain aggregates.

The enhancement of the 2.1-2.6 eV emission for the bulk sample occurs at ~ 20 kbar and for the film at a slightly higher pressure of ~35 kbar. The relative intensities of the various peaks in the 2.1-2.6 eV range under pressure are different in the film and in a powder sample. In bulk PF2/6 (Figure 3.7) both the keto and aggregate emission are equally enhanced at 20 kbar: the keto peak (~ 2.3 eV) gains intensity over the aggregate peak (~ 2.4 eV) beyond 42 kbar. Although the concentration of the keto defects is quite small in our PF2/6 sample (Figure 3.6), increasing the intermolecular interaction causes the emission from the defect sites to be considerably enhanced. This scenario is somewhat similar to the guest-host polyfluorene system where a small concentration of a chromophore with an absorption spectrum closely matching the emission of PFO drastically changes the PL emission.[43,44] In these systems there is an efficient Förster energy transfer to the host molecules that allows conversion of the blue emission from PFO into red emission of the guest chromophore. In our case the enhanced intermolecular interaction allows transfer from the backbone to the

keto defect making that emission more and more prominent as pressure increases.

The absorption spectrum as a function of pressure was measured from the same film (at the same pressures as the PL) and is shown in Figure 3.12. The spectra were taken at room temperature by dividing the sample transmission by the transmission of the empty diamond cell. Such a broad absorption spectrum is characteristic of the lower ordered alpha phase. With increasing pressure, the overall absorbance of the PF2/6 increases and the spectrum red shifts. Increased absorbance in the 2.7 eV region may be indicative of a more ordered phase. Although the alpha phase of PF does not show any absorption below 2.90 eV, one cannot rule out a red shift of the absorption edge from the alpha phase itself with increasing pressures. Such effects have been observed in m-LPPP under pressure.[45] A more likely explanation is the direct absorption by the keto defect at about 2.7 eV. This is a Förster energy transfer of the backbone emission to that of the guest defect chromophore. The sharp peak at 2.95 eV is from the type II diamond of the pressure cell used as a reference. Since the spectral emission from compact Ocean Optics lamp is not constant through the lifetime of the bulb a reference spectra was needed for each data point. Unfortunately the DAC chosen to be used as a reference cell had at least one type II diamond, impacting all of the absorption spectra.

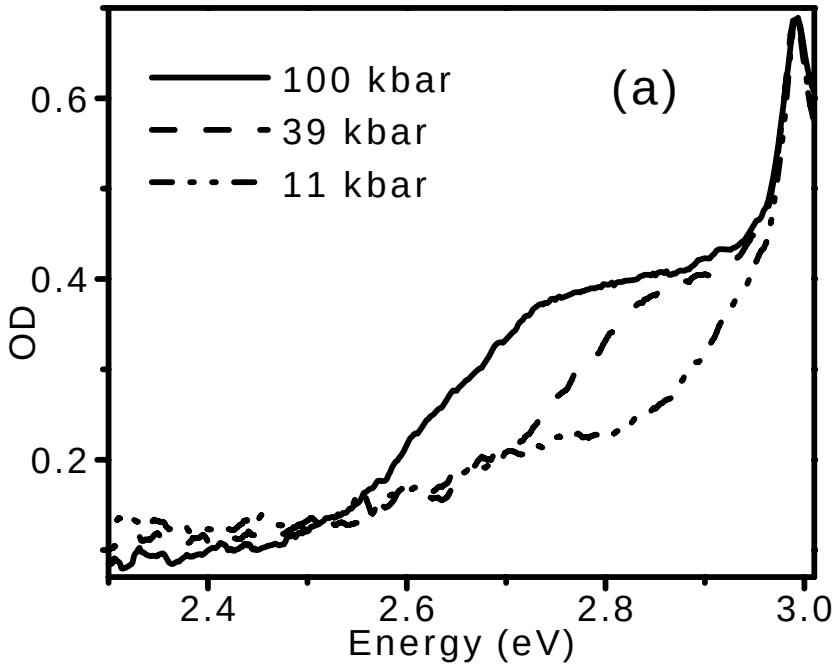

Figure 3.12 The absorption spectra at selected values of pressure

In the PF2/6 film, beyond 35 kbar the 2.1-2.6 eV emission dominates the backbone emission. The aggregate emission is stronger than the keto emission which appears as a weak shoulder at higher pressures. The higher aggregation in the film may result from a more compact and ordered nematic liquid crystal morphology in the film. This ordering may also explain the hysteresis of the PL spectra observed between increasing and decreasing pressures.

A weak shoulder at 1.9 eV is observed both in the film and powder samples of PF2/6 (Figures 3.7 and 3.9) at higher pressures. The exact origin of this peak is not understood but most probably it is due to aggregate emission. At higher pressures the 1.92 eV (647.1 nm) laser line used to excite the Raman directly

excites this emission as well. This emission then interacts with the discrete Raman phonons, which results in an antiresonance effect.

The overall PL intensity, due to aggregate and keto emission, increases noticeably at 42 kbar in the powder sample. A temperature scan was taken at this pressure since cooling the sample decreases the pressure by ~2 kbar, and thus allows us to cycle through any morphological or phase changes. The relative intensity of the backbone transitions was observed to decrease with increasing temperature. A significant change occurs between 150 K and 250 K; above 250 K the 0-0 transition is almost completely quenched and the broadband emission increases in intensity by more than a factor of three, figure 3.13. These changes in the PL are most likely due to morphological changes in PF2/6.[46] Transport measurements show that polymers in a liquid crystalline state exhibit greatly enhanced interchain charge carrier mobility.[32] Since PF2/6 does exhibit a crystalline to nematic liquid crystalline phase transition at about 40 kbar; it is possible that such a transition causes the sudden change in the relative intensities of the PL emission with increasing pressures.

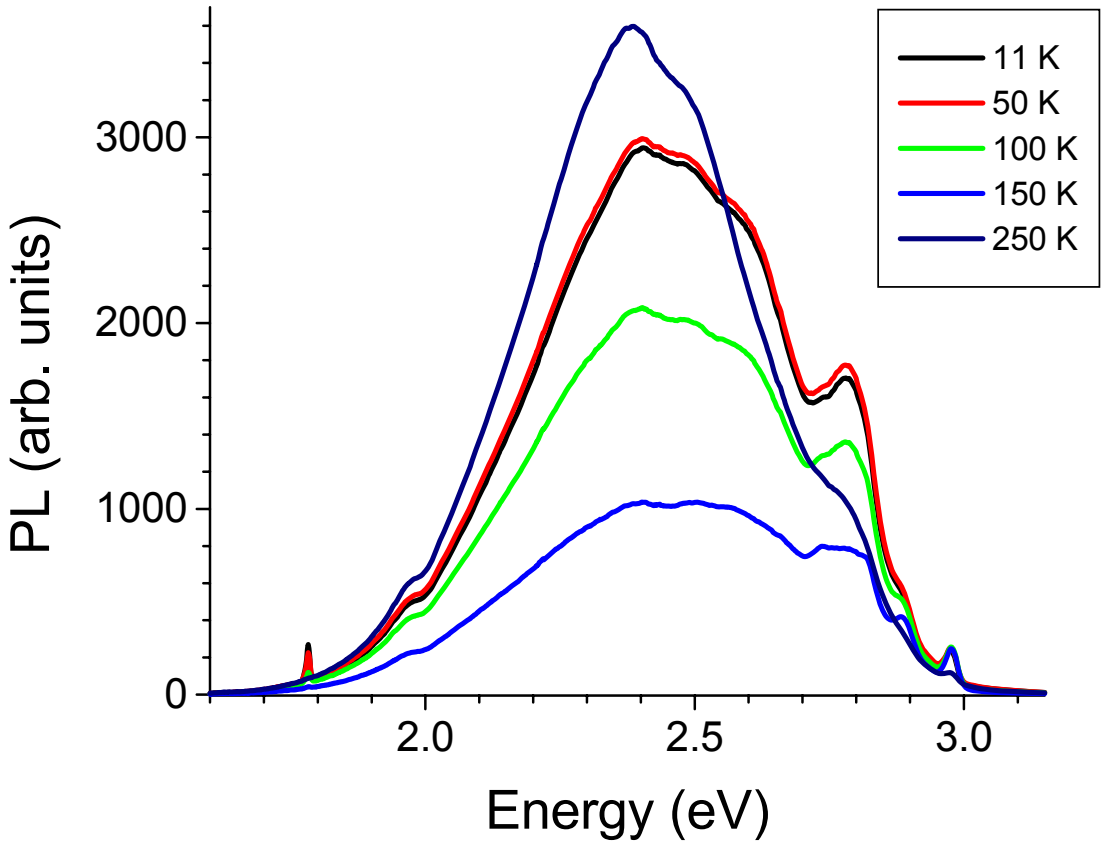

Figure 3.13 Photoluminescence from PF 2/6 at 42 kbar as a function of temperature.

The rate of red-shift of the 0-0 and 0-1 backbone emission peaks in the PF2/6 film under pressure is similar to shifts observed in m-LPPP film and PHP powder, as shown in Table 3.1. Future work on copolymers of PF2/6 and with other side-group substitutions are required to understand the dynamics of the backbone vibronics in the bulk PF2/6 sample, which barely appear to shift. This effect may well be an artifact due to the higher self-absorption in the powder or due to a different morphology of the powder as compared with the film under hydrostatic pressure. The shifts of the aggregate and keto emissions with pressure are similar in both the film and powder samples.

3.2.2 Raman Spectra of Polyfluorene

The Raman signal from the bulk PF 2/6 powder is quite strong yielding a very nice signal to noise ratio, shown in Figure 3.14 at 13 K and 300 K at ambient pressure. With increasing temperatures all the Raman peaks in the 1200-1600 cm^{-1} soften by ~2 cm^{-1} a value comparable to several known conjugated materials.[47]

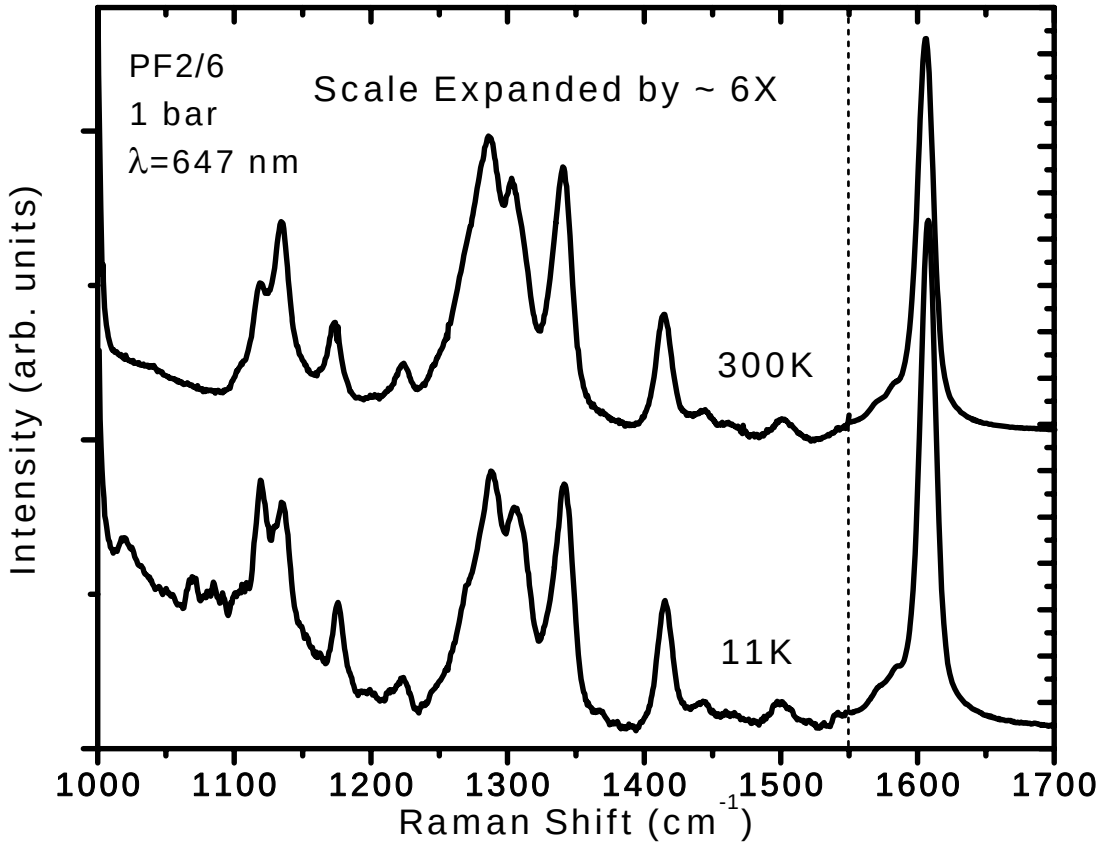

Figure 3.14 Raman spectra of PF2/6 at ambient pressure at 13 K and 300 K. The vertical scale has been expanded by about 6X below 1550 cm^{-1}.

The Raman frequencies in the 1050-1200 cm^{-1} region are sensitive to side group substitution; they arise from the C-H bending modes of the ethyl-hexyl side

group in PF2/6. The 1290 cm^{-1} 1342 cm^{-1} and the 1417 cm^{-1} are associated with the backbone C-C stretch modes. The Raman peaks in the 1600 cm^{-1} region arise from the intra-ring C-C stretch mode. These peak assignments are similar to those of Ariu *et al.*[48] in their work on PFO, there the Raman peaks in the 1200-1400 cm^{-1} region are attributed to the C-C stretch mode between adjacent phenyl rings. It has been assumed that the higher frequency modes in this region are due to the C-C stretch from within the more rigid monomer unit, while the C-C stretch modes between adjacent monomer units are expected to have a lower frequency due to the allowed torsional degree of freedom.[48] The 1600 cm^{-1} region of the spectrum is best fit with two peaks, a weak peak at 1582 cm^{-1} and a strong peak at 1605 cm^{-1}. The weak shoulder to the 1605 cm^{-1} has been observed in other PFs as well.[48,49]

As expected, some of the phonon modes are sensitive to the alkyl group substitution as can be seen in Figure 3.15. From this data it can be seen that the different side groups do not appreciably affect the phonon modes due to the PF backbone, but there are significant differences in the spectra around 1100 cm^{-1} and 1250 cm^{-1}. Also, several of the phonon frequencies have been shifted due to changes in the electronic/physical configuration of the molecule, but are visible in all of the spectra.

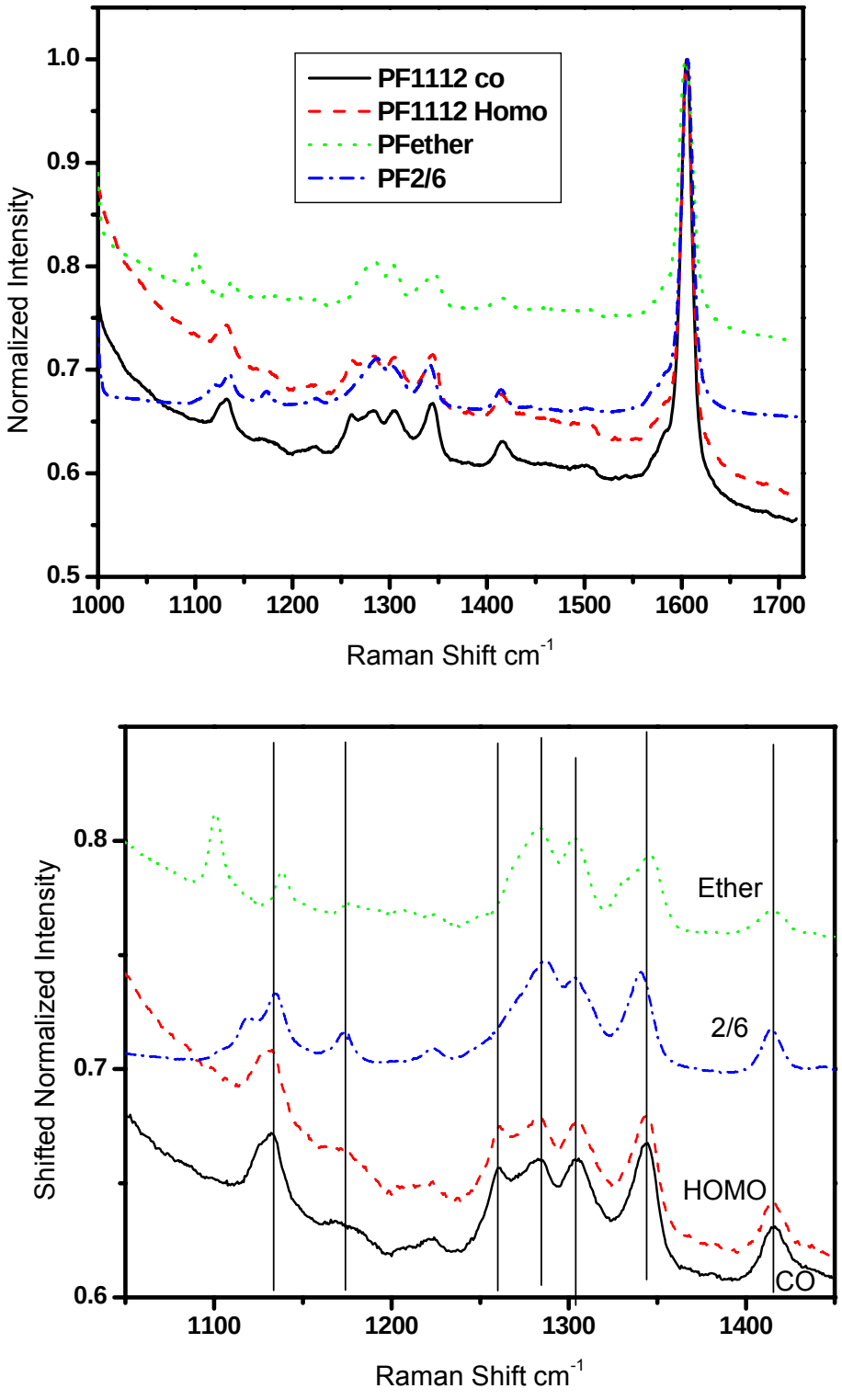

Figure 3.15 The Raman spectra from the PF samples at room temperature and ambient pressure are plotted here. All of the data has been normalized to the maximum of the 1600 cm^{-1} mode and shifted vertically for clarity.

The Raman spectra from PF2/6 at various pressures are plotted in figure 3.16. Each frequency region of the graph has been scaled individually so that key features in each spectrum are clearly observed. The break in the *x*-axis at 1300 cm^{-1} denotes the region where the Raman peak from the diamond has been removed for clarity. Most of the phonon frequencies corresponding to the backbone C-C stretch modes are not observable as a function of pressure due to the presence of the strong 1330 cm^{-1} Raman peak from diamonds in the DAC. As pressure is increased, all of the Raman frequencies analyzed tend to increase in frequency.

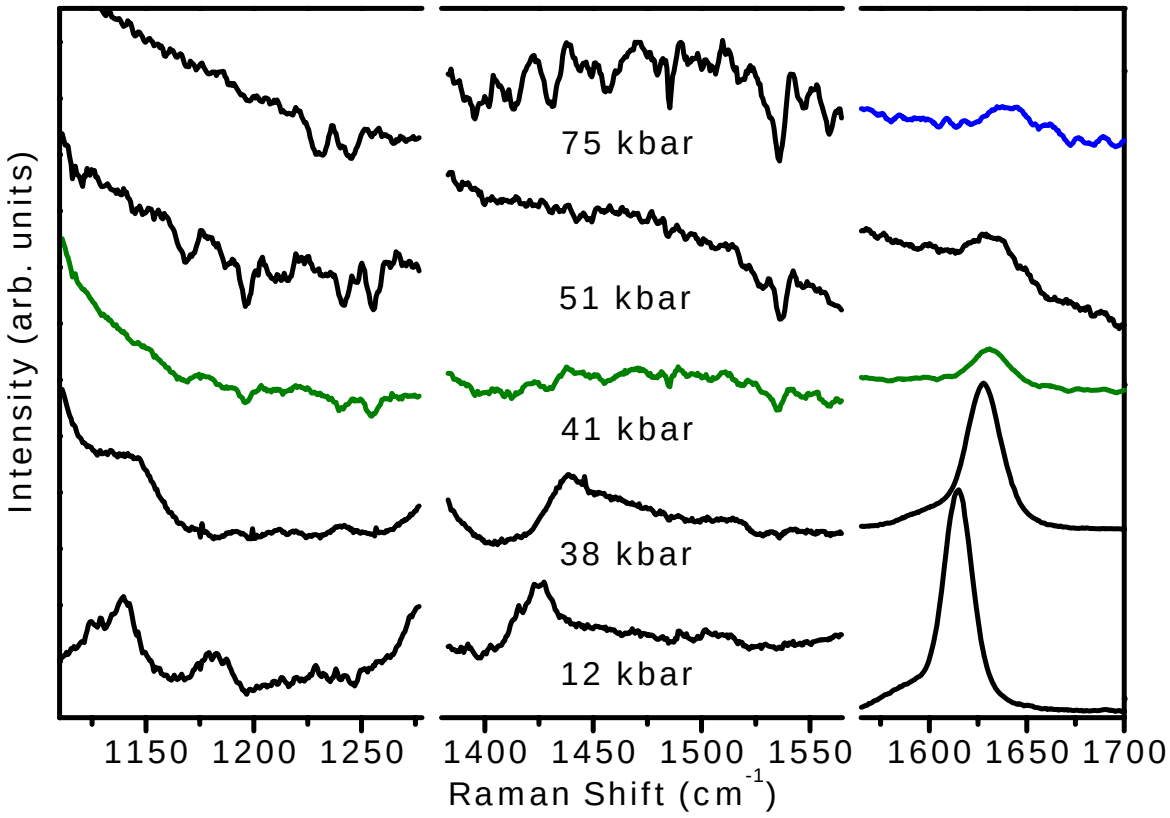

Figure 3.16 Raman spectra of PF2/6 at selected pressures. Each frequency region of the graph has been scaled individually to highlight the key features. Owing to the rising PL with increasing pressure, the background increases at higher pressures obscuring the low frequency Raman peaks.

At higher pressures the PL tail gains intensity, obscuring the Raman signal beginning with the lower frequency peaks. The region below ~1300 cm^{-1} is observable up to ~20 kbar and the 1417 cm^{-1} peak is observed up to about 40 kbar. Despite being well below the PL peaks of both the backbone and the keto emissions, the laser line still excites the low energy tail of the PL spectrum (see Figure 3.13). We believe that this tail most likely arises from aggregate emissions but possibly could also be due to the keto defects or residual impurities from processing.

The rising PL tail above 20 kbar causes several of the Raman peaks to exhibit asymmetric lineshapes and an antiresonance effect characteristic of a Breit-Wigner Fano (BWF) resonance. Such effects have been observed in inorganic semiconductors, for example in p and n-doped Si and Ge.[50,51] This effect is indicative of a strong electron-phonon interaction between the Raman phonons and the electronic continuum.[52] We find that the most consistent development of the BWF resonance is observed in the 1605 cm^{-1} peak with the development of asymmetry and increased broadening with increasing pressures is seen in Figure 3.16.

Along with the asymmetry of the 1605 cm^{-1} peak, new peaks exhibiting antiresonance effects appear near 1230 cm^{-1} and 1530 cm^{-1} (as seen in Figure 3.16). These peaks appear in the Raman spectra both with increasing and decreasing pressure. Although their signals are weak, their spectra are reproducible. Some of them may be infrared (IR) active modes that become Raman active at higher pressures in conjunction with phase/conformational

transitions of the material. E.J.W. List *et. al.*[53] report that there are a number of IR peaks in the 1000-1500 cm^{-1} range in PF with the strongest IR peak appearing at 1500 cm^{-1}. The 1530 cm^{-1} feature observed around 40 kbar is most likely the 1500 cm^{-1} IR active peak shifted to higher frequencies due to the applied pressure. This IR frequency shows a weak signature even in the 1 bar Raman spectrum (Figures 3.14 and 3.15), and the magnitude of the shift is consistent with the pressure shifts of the other Raman peaks.

Although the changes in the spectra have been shown to be reversible as the pressure is reduced, there is a hysterisis involved. As the pressure is lowered the PL shifts away from the excitation line used for the Raman measurements while dropping in intensity and the expected spectra are recovered. The pressure has to be reduced to below 15 kbar before the Raman and the PL signal fully recovers. G. Heimel also reports this hysterisis in work with fluorene monomers under high pressure (private communication).

The Raman peaks have been fit with Lorentzian lineshapes to determine their frequency positions and are plotted as a function of pressure in Figure 3.17. The 1417 cm^{-1} mode is seen clearly up to 40 kbar. The 1500 cm^{-1} peak is too weak in intensity to track below 40 kbar, but can be seen as antiresonance and can be tracked reliably for a few data points above 40 kbar. The 34 kbar data point for this peak was taken as the pressure was being decreased, and due to a hysteresis effect the peak was still visible. As the pressure was decreased further the PL background dropped in intensity and the low-pressure spectra

were fully recovered. All of the peaks shift with fairly similar pressure coefficients.

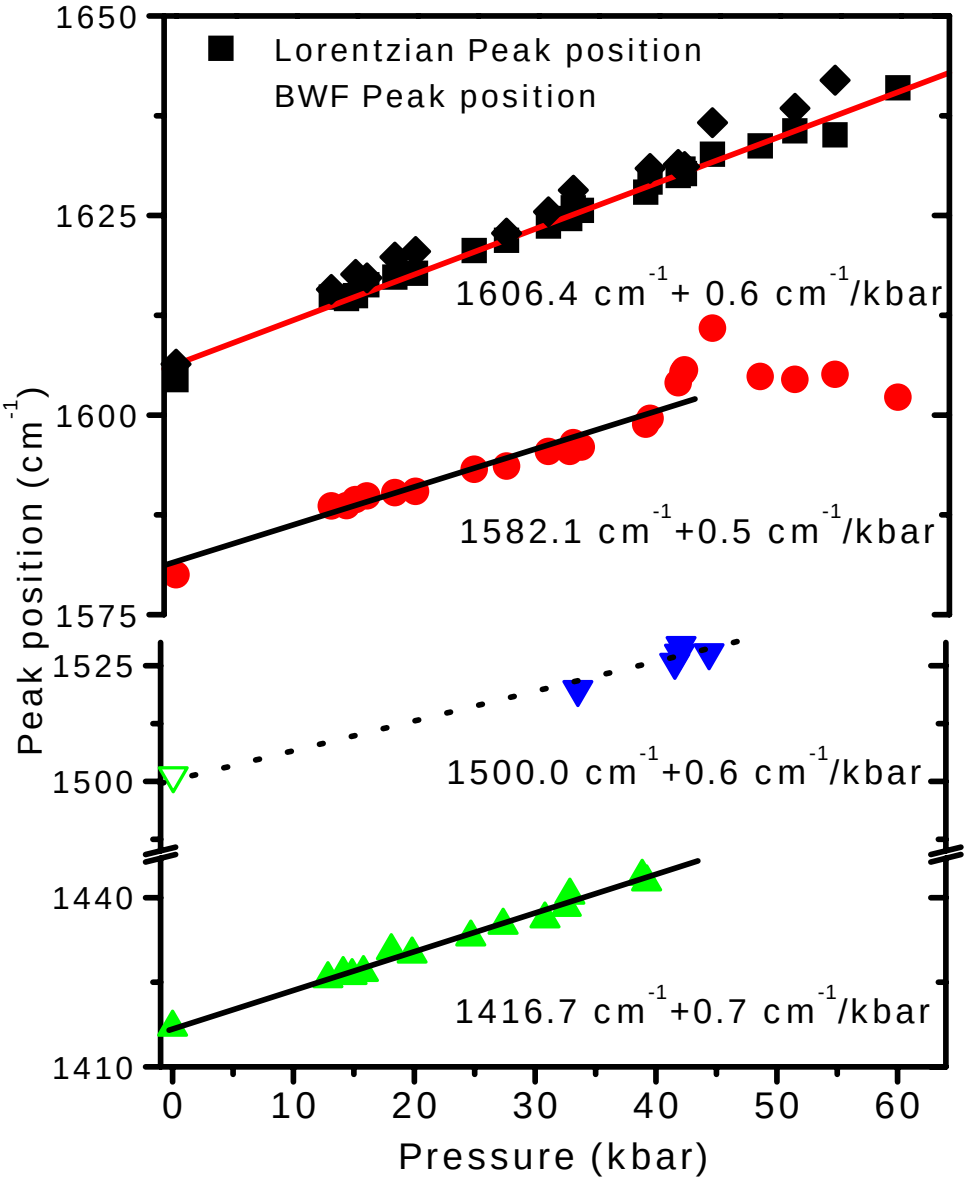

Figure 3.17 Peak positions of the 1417 cm^{-1}, 1500 cm^{-1} (IR-active), 1582 cm^{-1} (shoulder of 1605 cm^{-1}), and the 1605 cm^{-1} modes as a function of pressure. The open symbol (∇) denotes the position of the 1500 cm^{-1} peak at 1 bar. The slopes for the linear fits have an uncertainty of 0.05 cm^{-1} /kbar. The straight lines for the 1605 cm^{-1} and the 1582 cm^{-1} peaks are fits to the frequencies obtained from the Lorentzian fits up to 40 kbar.

The positions of the 1605 cm^{-1} and the shoulder peak at 1582 cm^{-1} are included up to 60 kbar in Figure 3.17. Above about 40 kbar the increase of the asymmetry of the 1605 cm^{-1} peak made fitting to the Lorentzian lineshape difficult. Since the interaction of the main 1605 cm^{-1} peak with the electronic continuum makes the lineshape broader and asymmetric it was more accurately determined by a BWF fit. It is possible only to resolve one peak using a BWF lineshape, Figure 3.18. The peak positions across the entire pressure range using both fit methods are plotted in Figure 3.19. At lower pressures there is good agreement between the peak frequencies determined by both the Lorentzian and the BWF fits, however the values deviate at higher pressures. The linear fits to the frequency vs. pressure data for the Lorentzian fits are shown in figure 3.17 up to 40 kbar.

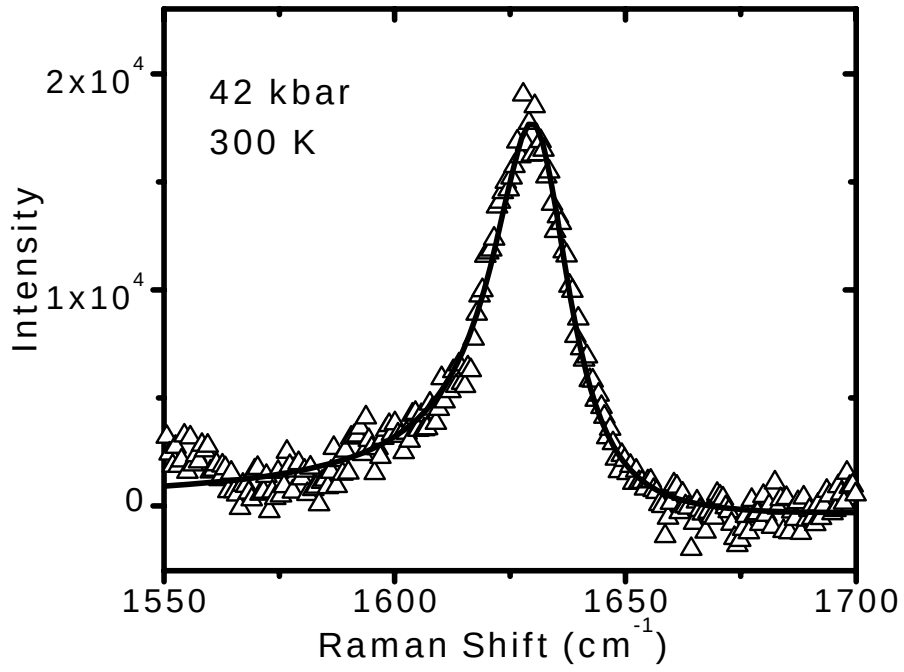

Figure 3.18 A sample BWF lineshape fit to the 1605 cm^{-1} peak at 42 kbar.

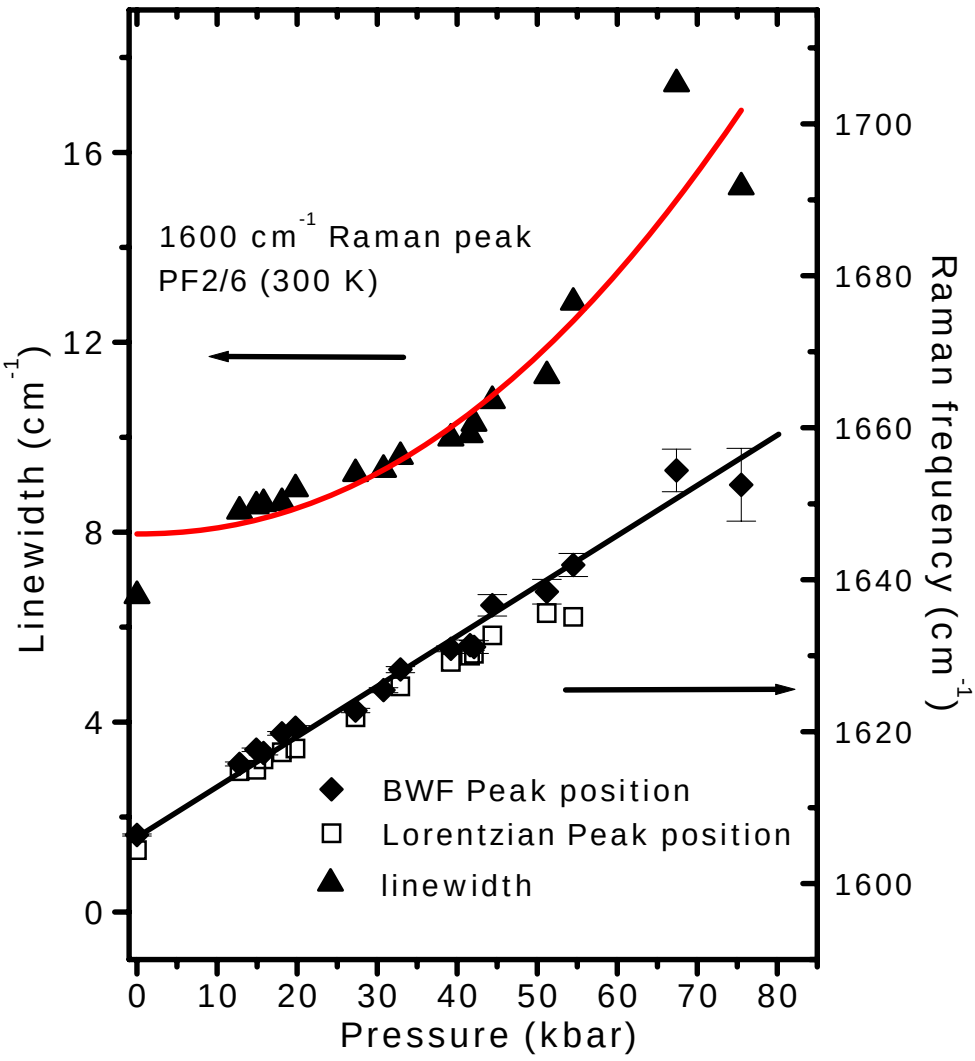

Figure 3.19 Linewidth and the peak position of the 1605 cm^{-1} Raman peak obtained by fits to Eq.1, as a function of pressure. A linear fit to the BWF peak position of the 1605 cm^{-1} Raman peak as a function of pressure yields a slope of 0.6 ± 0.02 cm^{-1}/kbar, as shown by the straight line.

Since the PL emission from the aggregates and the keto defects red shift, at higher pressures the 647.1 nm Raman excitation line (1.92 eV) excites the tail of the emission (Figure 3.7), which couples strongly to the phonons. We therefore directly excite the tail of the emission, which is most likely from defect and

aggregate emission, without exciting the backbone PL emission. This excludes the possibility of this low energy emission being from excimers.

To determine the peak position, asymmetry parameter and linewidth as a function of pressure, we fit the 1605 cm^{-1} peak with a BWF lineshape given by[54]

$$I(\omega) = I_0 \frac{\left[(\omega - \omega_0)/q + \Gamma \right]^2}{(\omega + \omega_0)^2 + \Gamma^2}, \quad (1)$$

where ω_0 is the discrete phonon frequency, and Γ is the width of the resonant interference between the continuum and discrete scattering channels. The asymmetry parameter (1/q) depends on the average electron-phonon matrix element *M* and the Raman matrix elements between the ground and excited states of the phonon and electron.[55] The broadening parameter is given by

$$\Gamma = \pi M^2 D(\omega) \quad (2)$$

where $D(\omega)$ is the combined density of states for the electronic transitions. For non-zero density of states it turns out that when

$$q = -(\omega - \omega_0)/\Gamma \quad (3)$$

the spectral function $I(\omega)$ will reveal an "antiresonance" close to the value of phonon frequency.[52] Figure 3.18 is a sample of a BWF fit to Eq. 1 (bold line) to the 1605 cm^{-1} Raman mode at 42 kbar.

Figure 3.20 shows the asymmetry parameter versus pressure for the 1605 cm^{-1} Raman mode. The asymmetry is relatively small up to about 35 kbar, with a 1/q value between -0.005 and -0.1. In this lower pressure region the Lorentzian and BWF fits give very similar results. Beyond 40 kbar however, the asymmetry

increases rapidly and 1/q varies from -0.3 to -0.6. The peak position and the linewidths from the BWF fits as a function of pressure are plotted in Figure 3.19. The linewidth shows a square law dependence with pressure ($\Gamma \alpha P^2$). The frequency positions vary almost linearly with pressure. Figure 3.21 shows 1/*q* to linearly vary with the linewidth Γ.

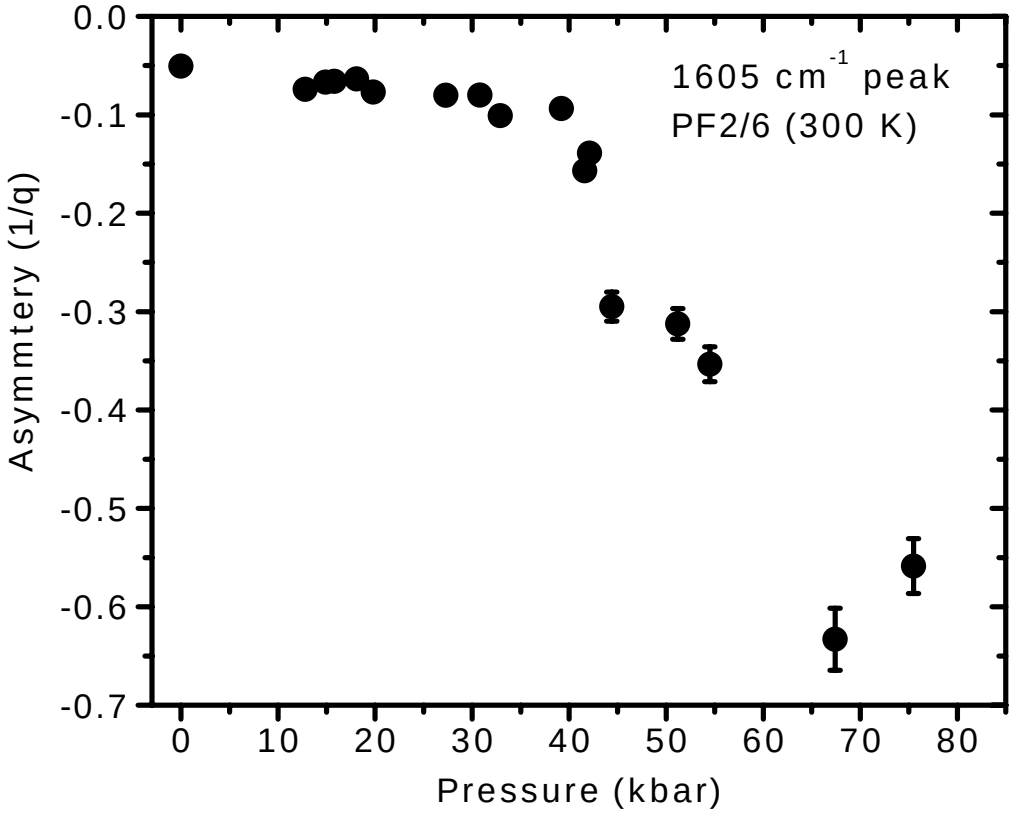

Figure 3.20 Asymmetry parameter(1/q) of the 1605 cm^{-1} Raman peak versus pressure obtained by fits with a BWF line shape (Equation 1).

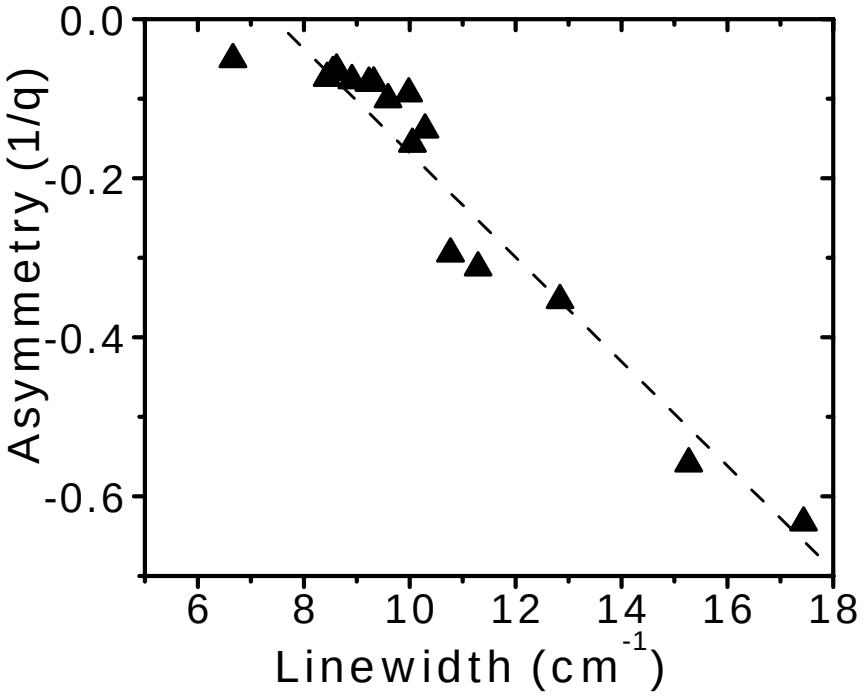

Figure 3.21 The asymmetry parameter (1/q) of the 1605 cm^{-1} Raman peak versus linewidth obtained by fits with a BWF line shape (Equation 1). The asymmetry parameter varies linearly with the linewidth.

Recently, optical techniques based on photoinduced infrared-active vibrational (IRAV) modes have been used to study the photogeneration and recombination dynamics of charged polarons in conjugated polymers.[56] Österbacka *et al*. have observed Fano-type antiresonances in the IRAV modes in a series of π-conjugated polymers that are explained well by extending the amplitude model beyond the adiabatic limit.[57] The observation here is somewhat different; the electronic continuum is from a combination of aggregate and/or defect emissions that shift to lower energies with increasing pressure. Figure 3.20 shows that the asymmetry parameter, q, is negative, indicating that the center frequency of the continuum lies below the discrete mode frequency of

1605 cm^{-1} (0.2 eV). The high background and the interference from the diamond Raman peak makes it difficult to analyze the asymmetry of the other Raman peaks as a function of pressure. The systematic appearance of the inverted 1530 cm^{-1} peak at higher pressures makes it a viable candidate for the IR-active frequency that gets activated in the Raman spectrum due to a lowering of the symmetry. Most probably the peak shows an s-like behavior due to the antiresonance effect and therefore appears as a negative peak. The pressure has been cycled several times to confirm the antiresonance effect on the 1530 cm^{-1} peak: the s-like behavior disappears at lower pressures but appears consistently at higher-pressure values.

Since the vibrational frequencies of a harmonic solid are independent of compression, pressure induced changes in the Raman spectrum provide insight into the anharmonicity of the solid state potential.[58] In this light the linear shift of the 1605 cm^{-1} peak as a function of pressure is not surprising. The rate of shift is similar to other Raman-active frequencies in PF2/6 which is an indication of the anharmonic potential. Although one expects an additional shift in phonon frequency due to the BWF interaction (the real part of the self energy) we cannot infer any information about this parameter from our data. In materials where the BWF interaction can be tuned, e.g. using uniaxial stress in both n-type[59] and p-type Si,[60] the real part of the self energy due to interaction between the phonon and the electronic continuum is determined by comparison with the pure material. In this work, such a comparison is not possible owing to a lack of a defect-free but identical material. Had this parameter been large one would expect a

significant deviation in the peak position vs. pressure behavior above 40 kbar where the BWF character of the mode is pronounced.

However, the imaginary part of the self-energy, Γ, does show a quadratic dependence with pressure. Furthermore, the asymmetry parameter should be directly proportional to Γ if the average electron-phonon matrix element and the Raman matrix elements between the ground and excited states are assumed to be roughly constant.[61] Indeed, this is what we find, as shown in Figure 3.21. The negative slope here is due to the negative q values that we obtain from the fit. At present we are unclear of the physical significance of the quadratic dependence of Γ on pressure, which reflects on the density of states of the continuum. A full-scale band-structure calculation incorporating aggregate and defect states should reveal the nature of the electronic density of states.

To further investigate the possible phase transition at 42 kbar, the temperature dependence of PL and Raman was measured. This was decided due to the overall PL intensity increasing noticeably at 42 kbar in the powder sample, due to aggregate and keto emission. A temperature scan decreases the pressure by ~2 kbar in the cell, and thus allows us to cycle through any morphological or phase changes. Figure 3.13 is a plot of the PL as a function of temperature at 42 kbar. It is interesting to note how the relative intensities of the transitions change with increasing temperature, the most significant of which occurs between 150K and 250K. The relative intensity of the backbone transitions was first observed to decrease with increasing temperature and then a significant change occurs between 150 K and 250 K. Above 250K the 0-0

transition is almost completely quenched and the broadband emission has increased in intensity by more than a factor of three. The temperature dependence of the PL from PF powder at 1 bar was published in MRS proceedings by S. Guha *et al.*[62] where they found a higher coupling of the C-C vibrations to the electronic states with increasing temperature. The relative strength of the 0-0 transition decreases with increasing temperatures relative to the 0-1 and 0-2, which is indicative of the Huang-Rhys factor increasing with increasing temperature. This is as a result of decreased conjugation and exciton localization.[63]

As the PL changes with temperature, the Raman is also impacted. An enhancement in the antiresonance effect can be seen between 150K and 250K in the Raman spectra plotted in Figure 3.22. This is due to the increase in intensity of the 1.9 eV emission that is directly excited by the 1.92 eV laser line used to excite the Raman. These changes in the PL and the impact on the Raman are most likely due to morphological changes in PF2/6.[64] Transport measurements show that polymers in a liquid crystalline state exhibit greatly enhanced interchain charge carrier mobility.[65] Since PF2/6 does exhibit a crystalline to nematic liquid crystalline phase transition, it is possible that such a transition causes the sudden change in the relative intensities of the PL emission along with directly impacting the Raman spectra with increasing pressures.[66,67,68]

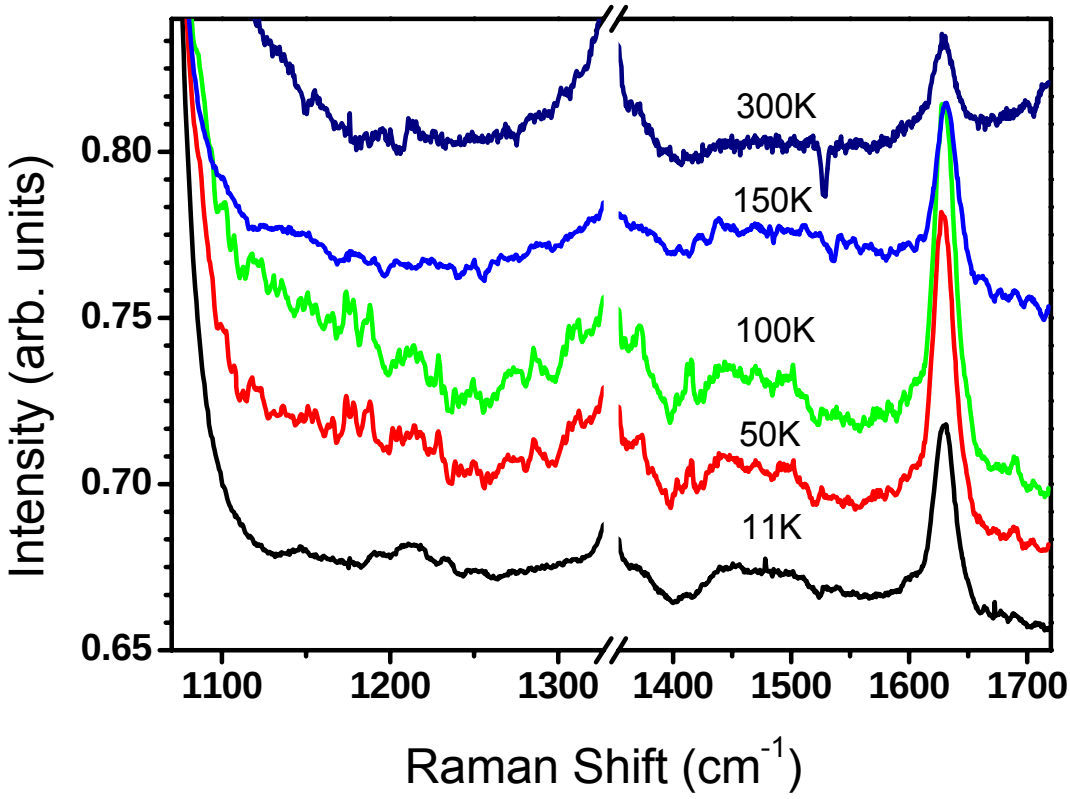

Figure 3.22 Raman from PF 2/6 at 42 kbar as a function of temperature

To investigate the impact of the temperature dependant phase transitions of PF2/6, a detailed series of Raman spectra were recorded as a function of temperature. These measurements were taken at specific temperatures and times to allow a direct correlation to x-ray data collected by M. Winokur.[69] From the x-ray data it can be seen that there is some initial order present in the meta-stable glassy sample. The sample was initially cooled slightly (to 245K) and then warmed towards the glass rubber transition, T_g, which is about 80 ºC for this material. The T_g was determined by DSC measurement and is result for bulk material. As the temperature approaches the T_g the material becomes softer allowing molecules freedom to align and increase extended ordering. This is

evident in the new peaks emerging in the x-ray spectra at these temperatures. Considerable time is needed to allow the sample to achieve energetic equilibrium as the molecules reorient themselves in the sample.

Almost all of the Raman modes increase in intensity as the temperature is increased past T_g, Figure 3.23. The intensity of the weaker modes at about 1417 cm^{-1} and 1500 cm^{-1} are not affected as strongly as the other modes. This trend in the Raman intensities continues to between 115 ºC and 130 ºC where the intensity of all of the modes except the 1500 cm^{-1} drops significantly then remains fairly constant up to 177 ºC, Figure 3.24. There is a corresponding change in the x-ray spectrum at these temperatures due to the changing amorphous vs. crystal ratio as the sample crystallizes. The sample was heated to about 145 ºC and after about six hours the intensity of the Raman modes stabilized, Figure 3.25. The x-ray data indicate that at this point the ordering is highest in the sample.

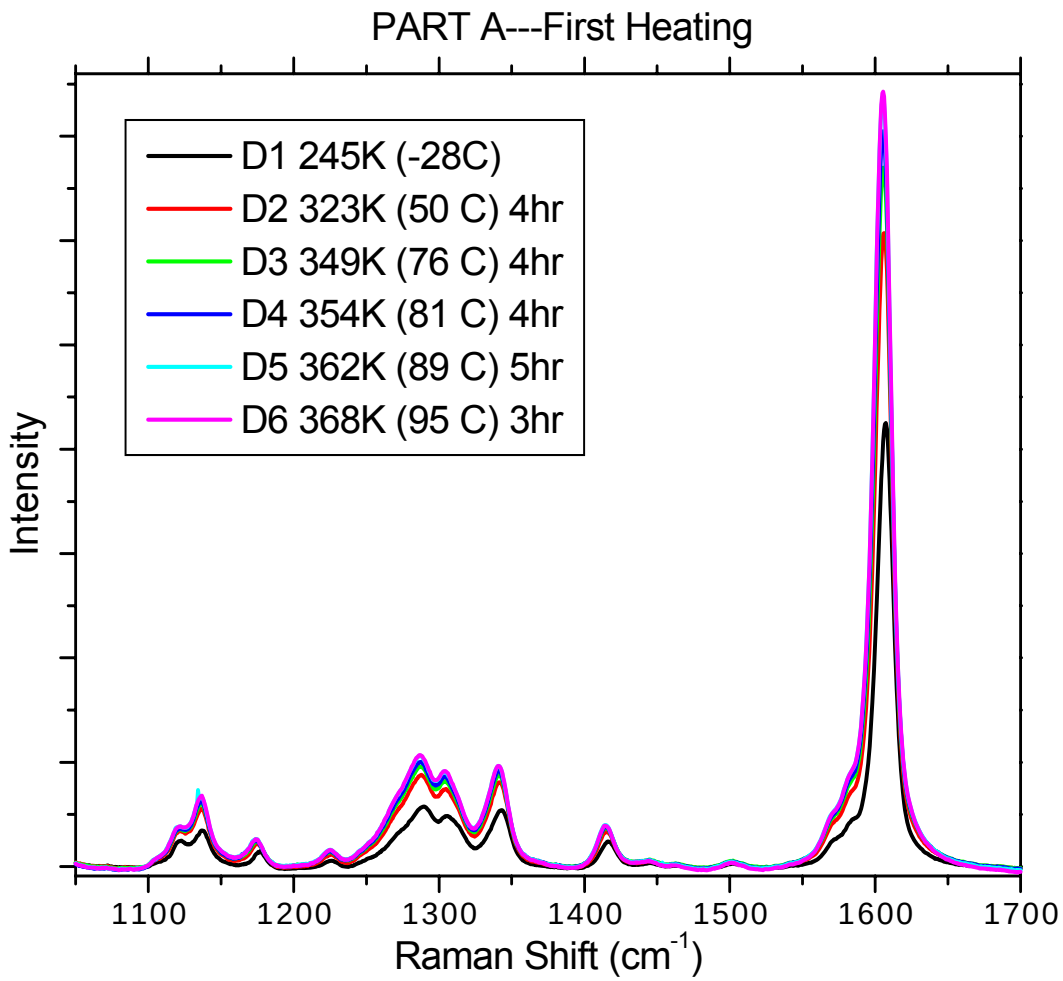

Figure 3.23 Raman from PF2/6 as a function of temperature and time. T_g for this material is about 80 ºC. The long dwell time at each temperature allows the sample to achieve structural equilibrium.

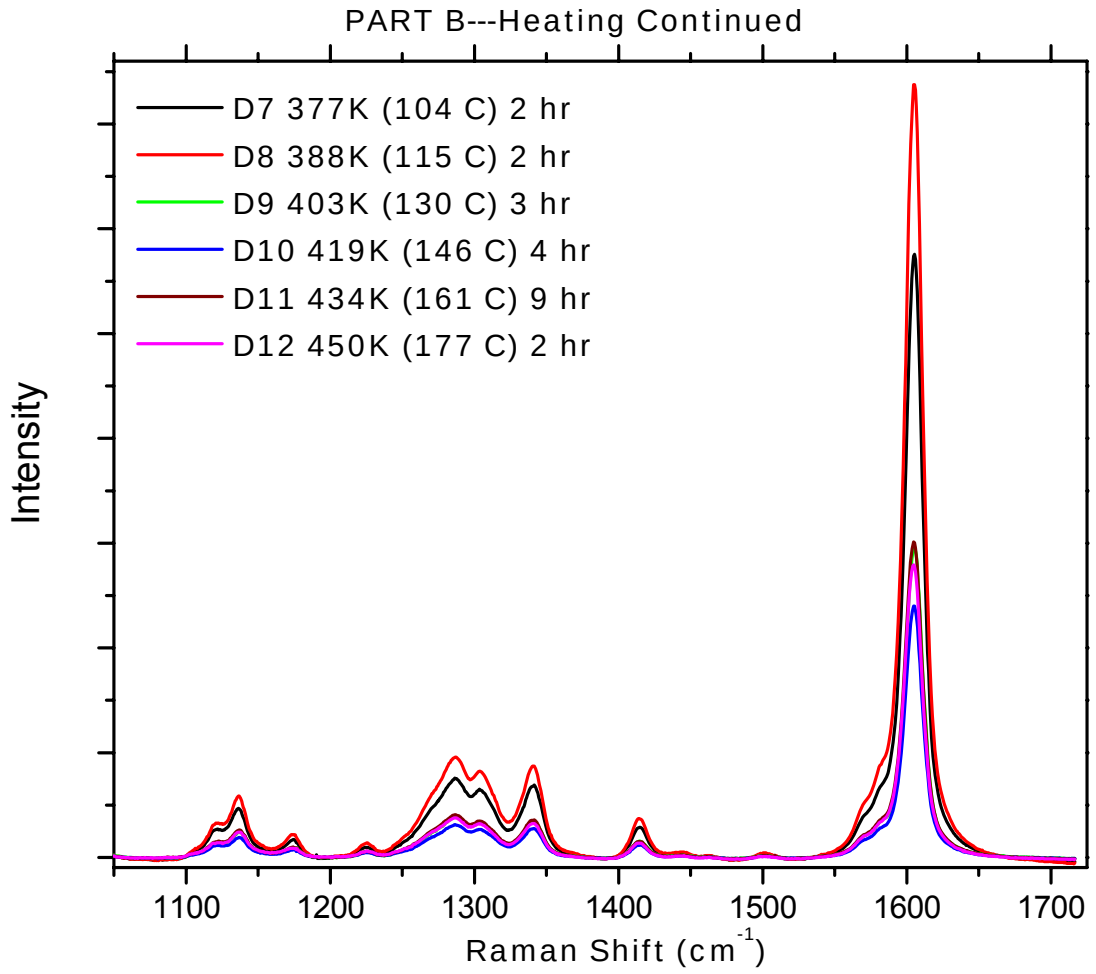

Figure 3.24 Raman from PF2/6 as temperature is increased from T_g to T_{lc}

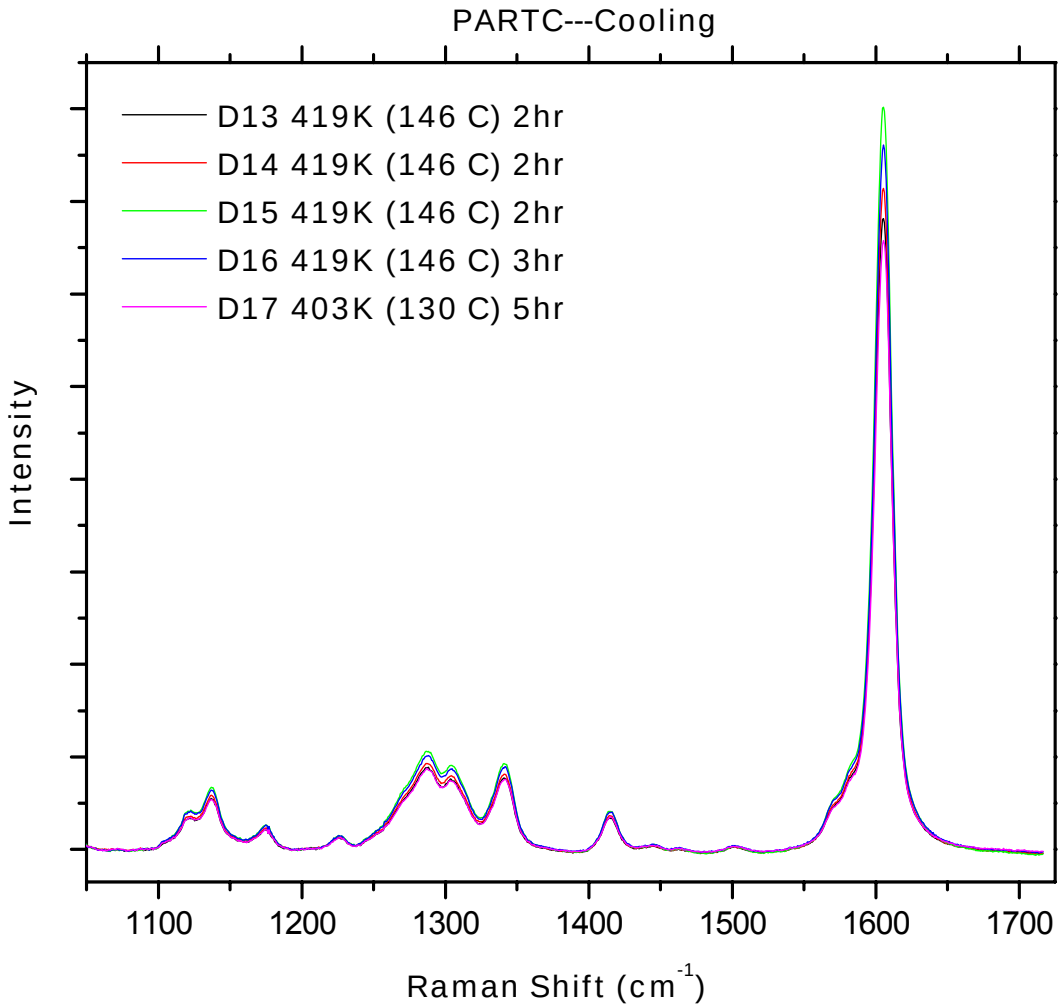

Figure 3.25 Raman from PF2/6 at about the liquid crystal transition 145 ^{0}C

As the sample is slowly cooled back below T_g the Raman signals loose some intensity, Figure 3.26, but is still enhanced from the initial intensities. The reduction in intensity is not the same for all of the modes. The intensity of the modes associated with the alkyl side groups does not change as significantly as the 1600 cm^{-1} mode or the monomer associated modes in the 1250 cm^{-1} to 1350 cm^{-1} range. The x-ray data indicate that after the sample is heated and then cooled the ordering that is achieved is frozen in place at T_g.

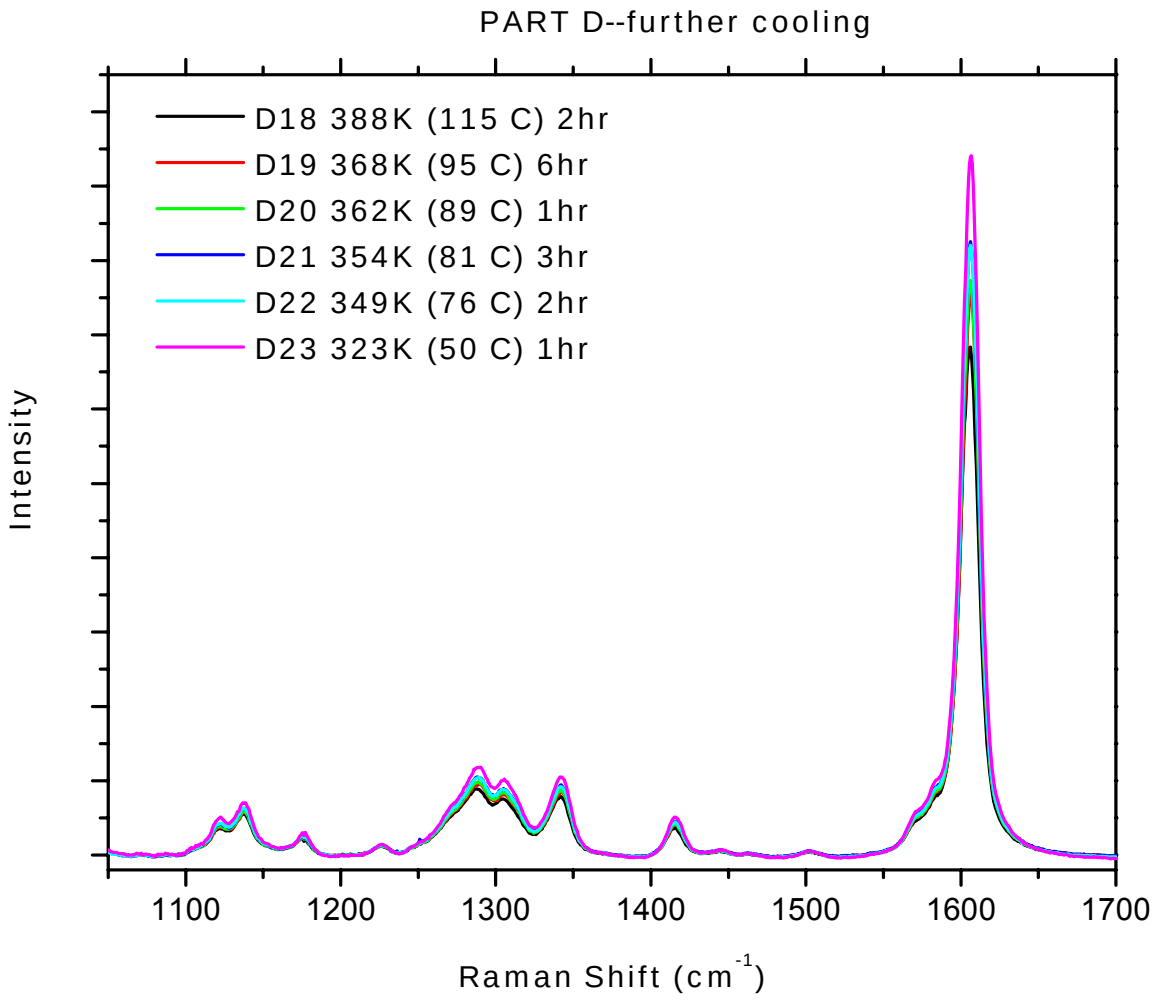

Figure 3.26 Raman from PF2/6 as the sample is slowly cooled to room temperature.

Upon heating PF2/6 undergoes some drastic irreversible morphology changes as can be seen in the SEM images in Figure 1.5. The thin fibrous structures initially present on the surface of the soft glassy sample have melted resulting in smooth hard surface. X-ray results confirm this irreversible

conformational change of the material as the temperature passes the glass rubber transition and the liquid crystal transitions.[69]

3.3 References

[1] Georg Heimel, “High Pressure Studies on Structural and Optical Properties of Poly(Para-Phenylene) based Systems”, Diploma Thesis, Institute of Solid State Physics, University of Technology Graz, (2000).

[2] S. Guha, W. Graupner, R. Resel, M. Chandrasekhar, H.R. Chandrasekhar, R. Glaser, and G. Leising, Phys. Rev. Lett. 82, 3625 (1999).

[3] L. A. Carreira, T. G. Towns, J. Mol. Struct. 1, 1 (1977).

[4] Mariacristina Rumi, Giuseppe Zerbi, Chem Phys, 242, 123-140, (1999)

[5] Giuseppe Zannoni and Giuseppe Zerbi, J. Chem. Phys. 82 (1), Jan (1985).

[6] G.Zannoni, G. Zerbi, J. Chem. Phys. Vol. **82**, 31 (1985).

[7] L.Cuff, M. Kertesz, Macromolecules **27**, 762 (1994).

[8] M. Rumi, G. Zerbi, K. Müllen, G. Müller, J. Chem. Phys. Vol. **106**, 1 (1997).

[9] G. Louarn, L. Athouël, G. Froyer, J.P. Buisson, S. Lefrant, Synthetic Metals **55**, 4762 (1993).

[10] H. Ohtsuka, Y. Furukawa, M. Tasumi, Spectrochemica Acta, Vol. 49A, No. 5/6, pp 731-737 (1993).

[11] G. Heimel, D. Somitsch, P. Knoll, and E. Zojer, J. Chem. Phys., **116**, 10921 (2002).

[12] A. Marucci, M.A. Pimenta, S.M.D. Brown, M.J. Matthews, M.S.Dresselhaus, M. Endo, J. Mater Res. Vol. **14**, No. 8 (1999).

[13] G. Heimel, D. Somitisch, P. Knoll, J. Brédas, E. Zojer, J. Chem. Phys. **122**, 114511, (2005).

[14] S. Guha, W. Graupner, R. Resel, M. Chandrasekhar, H.R. Chandrasekhar, R. Glaser, G. Leising, J. Phys. Chem. A 105, 6203-6211 (2001).

[15] C.M. Martin, Q. Cai, S. Guha, W. Graupner, M. Chandrasekhar, H.R. Chandrasekhar, Phys. Stat. Sol (b) 241, 3339 (2004).

[16] S. Krichene, S. Lefrant, G. Froyer, F. Maurice, Y.J. Pelous, J. De Physique 44, C3-733 (1983).

[17] Y. Furukawa, H. Ohtsuka, M. Tasumi, Synthetic Metals **55**, 516 (1993).

[18] G.Leising, T.Verdon, G.Louran, and S.Lefrant, Synthetic Metals **41**, 279 (1991).

[19] H. Ohtsuka, Y. Furukawa, and M. Tasumi, Spectrochim. Acta, Part A **49**, 731 (1993).

[20] K.K Zhuravlev, M. D. McCluskey, J. Chem. Phys. Vol. **120**, 4, (2004).

[21] K.K Zhuravlev, M. D. McCluskey, J. Chem. Phys. Vol. **114**, 13, (2001).

[22] C.M. Martin, S. Guha, M. Chandrasekhar, H.R. Chandrasekhar, R. Guentner, P. Scanduicci de Freitas, U. Scherf, Physical Review B 68, 115203 (2003)

[23] C.M. Martin, S.Guha, M. Chandrasekhar, H.R. Chandrasekhar, R. Guentner, U. Scherf, International Conference on Synthetic Metals, Synthetic Metals, 135-136, 273, (2003).

[24] U. Scherf and E.J.W. List, Adv. Mater. 14, 477 (2002).

[25] E.J.W. List, R. Guentner, P. S. de Freitas, and U. Scherf, Adv. Mater. 14, 374 (2002).

[26] D. Moses, A. Feldblum, E. Ehrenfreund, A.J. Heeger, T.-C. Chung, A.G. MacDiarmid, Phys. Rev. B 26, 3361 (1982).

[27] B.C. Hess, G.S. Kanner, and Z.V. Vardeny Phys. Rev. B 47, 1407 (1993).

[28] S. Yang, W. Graupner, S. Guha, P. Puschnig, C. Martin, H. R. Chandrasekhar, M. Chandrasekhar, G. Leising, C. Ambrosch-Draxl, U. Scherf, Phys. Rev. Lett. 85, 2388 (2000).

[29] S. Guha, S. Yang, W. Graupner, M. Chandrasekhar, H.R. Chandrasekhar, and G. Leising. Physica Status Solidi B 211, 177 (1999).

[30] S. Webster, and D.N. Batchelder, Polymer 37, 4961 (1996).

[31] G. Yang, Y. Li, J.O. White, and H.G. Drickamer, J. Phys. Chem. B 103, 7853 (1999).

[32] M. Redecker, D.D.C. Bradley, M. Inbasekaran, and E.P.Woo, Appl. Phys. Lett. 74, 1400 (1999).

[33] H. Sirringhaus, R.J. Wilson, R.H. Friend, M. Inbasekaran, W. Wu, E.P. Woo, M. Grell, and D.D.C. Bradley, Appl. Phys. Lett. Vol. 77, number 3, July (2000).

[34] J. Lanzo, F.P. Nicoletta, G. De Flipo, G. Chidichimo, Jap. Appl. Phys, Vol. 92, 8, October, (2002).

[35] Amena L. T. Khan, Paiboon Sreearunothai, Laura M. Herz, Michael J. Banach, and Anna Kohler, Phys. Rev. B, 69, 085201, (2004).

[36] J.L. Bredas, J.P. Calbert, D.A. da Silva Filho, and J. Cornil, PNAS, Vol. 99, 5804-5809, (2002).

[37] Alasdair J. Campbel, Donal D.C. Bradley, Homer Antoniadis, Appl. Phys Lett. Vol 79, 2133, (2001).

[38] S. Yang, W. Graupner, S. Guha, P. Puschnig, C. Martin, H. R. Chandrasekhar, M. Chandrasekhar, G. Leising, C. Ambrosch-Draxl, Phys. Rev. Lett. **85**, 2388, (2000).

[39] V.N. Bliznyuk, S. A. Carter, J.C. Scott, K. Klrner, R.D. Miller, and D.C. Miller Macromolecules 32, 361 (1999).

[40] L.M. Herz and R.T. Phillips, Phys. Rev. B 61, 13691 (2000).

[41] E.J.W. List, R. Guentner, P. S. de Freitas, and U. Scherf, Adv. Mater. 14, 374 (2002).

[42] J.M. Lupton, M.R. Craig, and E.W. Meijer, Appl. Phys. Lett. 80, 4489 (2002).

[43] T. Virgili, D.G. Lidzey, and D.D.C. Bradley, Adv. Mat. 12, 58 (2000).

[44] G. Cerullo, S. Stagira, M.Z-Rossi, S. DeSilverstri, T. Virgili, D.G. Lidzey, and D.D.C. Bradley, Chem. Phys. Lett. 335, 27 (2001).

[45] M. Chandrasekhar, S. Guha, and W. Graupner, Adv. Mater. 13, 613 (2001).

[46] X-ray studies of fluorene under high pressure show crystallographic phase changes starting at about 40 kbar (M. Winokur, Private Communication).

[47] S. Guha, W. Graupner, R. Resel, M. Chandrasekhar, H.R. Chandrasekhar, R. Glaser and G. Leising, Phy. Rev. Lett. 82, 3625 (1999); *ibid*, J. Phys. Chem. A 105, 6203 (2001).

[48] M. Ariu, D.G. Lidzey, and D.D.C. Bradley, Synth. Met. 111-112, 607 (2000).

[49] H. Leim P.Etchegoin, K.S.Whitehead, and D.D.C.Bradley, J. Appl. Phys 92, 1154 (2002).

[50] M. Chandrasekhar, J.B. Renucci, and M. Cardona, Phys. Rev. B 17, 1623 (1978).

[51] L. Pintschovius, J.A. Verges, and M. Cardona, Phys. Rev. B 26, 5658 (1982).

[52] M.V. Klein, *Light Scattering in Solids*, edited by M. Cardona, Springer-Verlag, New York, (1975).

[53] E.J.W. List, R. Guentner, P. S. de Freitas, and U. Scherf, Adv. Mater. 14, 374 (2002).

[54] P. Zhou, K-A. Wang, P.C. Eklund, G. Dresselhaus, and M.S. Dresselhaus, Phys. Rev. B 48,8412 (1993).

[55] M. Chandrasekhar, J.B. Renucci, and M. Cardona, Phys. Rev. B 17, 1623 (1978).

[56] P. B. Miranda, D. Moses, and A.J. Heeger, Phys. Rev. B 64, 081201 (2001).

[57] R. Österbacka, X.M. Jiang, C.P. An, B. Horovitz, and Z.V. Vardeny, Phys. Rev. Lett. 88,226401 (2002).

[58] J.R. Ferraro, *Vibrational spectroscopy at high external pressures*, Academic Press, New York (1984).

[59] M. Chandrasekhar, J.B. Renucci, and M. Cardona, Phys. Rev. B 17, 1623 (1978).

[60] L. Pintschovius, J.A. Verges, and M. Cardona, Phys. Rev. B 26, 5658 (1982).

[61] S. Satpathy, M. Chandrasekhar, H.R. Chandrasekhar, and U. Venkateswaran, Phys. Rev. B 44,11339 (1991).

[62] S. Guha, J.D. Rice, C.M. Martin, W. Graupner, M. Chandrasekhar, H.R. Chandrasekhar, U. Scherf, Mat. Res. Soc. Symp. Proc> Vol. 708 (2002).

[63] S-H Lim, T.G. Bjorklund, and C.J. Bardeen, Chem. Phys. Lett. **342**, 555 (2001).

[64] X-ray studies of fluorene under high pressure show crystallographic phase changes starting at about 40 kbar (M. Winokur, Private Communication).

[65] M. Redecker, D.D.C. Bradley, M. Inbasekaran, and E.P.Woo, Appl. Phys. Lett. 74, 1400 (1999).

[66] H. Liem, P. Etchegoin, K.S. Whitehead, D.D.C. Bradley, Jap. Appl. Phys. Vol 92, 1154, (2002).

[67] R. Stevenson, A.C. Arias, C. Ramsdale, J.D. MacKenzie, and D. Richards, Appl. Phys Lett., Vol 79, 2178, (2001).

[68] M. Ariu, D.G. Lidzey, D.D.C. Bradley, Synt. Met. 111-112, (2000).

[69] B. Tanto, S. Guha, C.M. Martin, U. Scherf, and M.J. Winokur, Macromolecules 37, 9438 (2004).

4. Conclusion

In previous 300K study of the Raman modes under pressure the focus was primarily on the 1220, 1280 and 1600 modes in 6P. We found that there was clear evidence for planarization of the molecule at ~ 15 kbar by using the intensity ratio I_{1280}/I_{1220} as an indicator. This ratio started out at 0.84 at 1 bar dropped rapidly to ~0.3 around 15 kbar and stayed close to that value thereafter. In this comparative study of 3P, 4P, and 6P, we show that both the frequencies and intensities of the two pairs of modes 1280-1220 and 1610-1600 are affected by planarization. The relative intensities of the 1280 cm^{-1} and 1220 cm^{-1} modes show a similar steep drop in intensity up to the planarization pressure and a gradual increase thereafter. The slow increase of the ratio of the intensities above the planarization pressure indicates that the molecules remain fairly planar. The relative intensities of the 1600 $cm^{-1}$and 1610 cm^{-1} modes also shows a decrease in the intensity of the 1610 cm^{-1} mode with pressure.

A remarkable feature is the rapid change in the frequency of the 1220 cm^{-1} in-plane bending mode during planarization. In contrast, the 1600 cm^{-1} region modes do not have as clear a two-slope behavior; however, a more sensitive measure of planarization is the frequency difference between the 1610 cm^{-1} and the 1600 cm^{-1} modes, which exhibits a distinct drop before planarization, and a gradual increase thereafter. Since the 1600 cm^{-1} mode is due to the aromatic C-C stretch within the ring, the torsional motion of the adjacent rings does not affect this mode. The resonance conditions that are responsible for the 1610 cm^{-1}

mode render the two-slope behavior less pronounced as compared to the 1280-1220 pair of modes and the changes in the C-H flex mode.

The intensity and frequency of the Raman modes from all three oligophenyls studied exhibit similar pressure dependencies. By fitting the 1220 cm^{-1} positions in two linear segments, the planarization pressure has been determined to be: 10±1.5 kbar, 9±2 kbar, and 13±1 kbar for 3P, 4P and 6P respectively.

I have presented an optical study on a variety of polyfluorene type polymers to investigate the changes in optical properties as a function of hydrostatic pressure, temperature, and side group substitution. The role of the keto defect in the PL emission and the effect of phase transitions on the charge carrier mobility were also explored. It has been shown that hydrostatic pressure induces very efficient energy transfer of the singlet excitons to the keto defect sites mainly in bulk PF2/6. Enhanced intermolecular interaction induces a strong aggregate-type emission in the film sample, in addition to a keto emission. This may result from a pinning of excitations in ordered regions in the film that prevents excitation diffusion to the defect states.

The Raman modes harden with increasing pressures. The 1605 cm^{-1} peak exhibits an asymmetric lineshape, characteristic of a Breit-Wigner Fano resonance, and some of the other peaks show an antiresonance effect. This is indicative of a strong electron-phonon interaction between the Raman phonons and the electronic continuum. The asymmetry observed in the Raman lines is fully consistent with the PL data, i.e., the BWF resonance is pronounced beyond 40 kbar where the PL emission drastically changes. The aggregate and defect

related emission increases significantly and the asymmetry of the 1605 cm^{-1} Raman peak becomes higher.

Upon heating PF2/6 undergoes some drastic irreversible morphology changes that leave the once soft fibrous glassy sample hard and smooth. These changes are accompanied by changes in the crystallinity of the sample as seen in the x-ray data.

Vita

Christopher Martin was born on September 13, 1973 in Emporia Kansas to Jerry and Cindy Martin. Christopher graduated from John Glenn High School in 1991. Throughout high school hobbies such as FM radio disk jockey, amateur radio, rappelling, hiking, and scuba diving occupied most of his time. Starting during his sophomore year of high school Chris was a research assistant to Dr. Hayes Cummings in the geology department at Muskingum College, helping to collect data to determine the extent of the damage due to acid mine drainage from the local strip mines. Chris later attended Muskingum College and majored in physics with minors in math and speech communications/broadcasting. After graduation in 1995, Chris moved onto Western Illinois University where he studied high temperature super conductivity under the advisement of Dr. Mark Boley until graduating in 1997. Dr. Boley is an alumnus of MU and was a student of Dr. Chandrasekhar which led Chris into the field of high pressure optical properties of materials. While attending MU Chris researched the impact of molecular configuration of basic photo-physical properties.